2018

Mixing and dispersion of a small estuarine plume

Sheridan, Megan

MIXING AND DISPERSION OF A SMALL ESTUARINE PLUME

by

Megan Marie Sheridan

A thesis submitted to the University of Plymouth

in partial fullfilment for the degree of

Master of Philosophy

School of Biological and Marine Sciences

September 2018

For Eric, who set me on this path, and who repeatedly encouraged me to do this; and for Ricardo, Javier and Samuel, for the support, encouragement and love that I absolutely needed to reach the end.

ACKNOWLEDGEMENTS

First, thank you to the School of Biological and Marine Sciences (formerly the School of Marine Sciences and Engineering), for providing the funding that made this happen.

My thanks also extend to my families at Plymouth University and the UC Davis Bodega Marine Laboratory, for all of you helped me to get to this point. To Dr. Phil Hosegood, whose patience, flexibility and support helped me get this done. To Dr. Paul Russell, for negotiating the terms of my employment so that I could do this in the first place. To Peter Ganderton, for everything: specifically help in the field and helpful chats. To Dr. Alex Nimmo Smith for field advice and support. To Rich Lilley, Jon Frary, Will Davies and Alastair McCallien for being excellent and accomodating skippers. To Sam Cox, Pedro Almeida, Guiomar Lopez, Claire Earlie, Rich Kenyon, Jonathan Coe, Marcus Zanacchi, and Tim Sykes (and Will, Seb and Adam- three undergraduates whose last names I don't remember!) for weathering wind and rain and near-constant CTD profiling (by hand) in the field. I know I made you work. To Tim Scott, Kit Stokes and Sam Prodger for help with the bathymetric survey. And to Helen Nance for helping to coordinate boat use, and Bob Bray for allowing it all. I wouldn't have done any of this without you all!

And to my BML family: thank you to Dr. John Largier, for providing guidance from 6000 miles away, and for being one of the best bosses one could have, and to Skyli McAfee, for being the other. To Jennifer Fisher, for telling me on more than one occasion to get my act together and do this, and to Dr. Seth Miller for being one of the funniest, supportive and inspirational friends and co-workers that a girl could have.

And finally, to my mom and dad, and my whole family for giving me the foundation that helped me to get to this point, and for your love and support these past few years.

You have all helped me do this. Thank you.

Thank you to Kayla Friedman and Malcolm Morgan of the Centre for Sustainable Development, University of Cambridge, UK for producing the Microsoft Word thesis template used to produce this document.

AUTHOR'S DECLARATION

At no time during the registration for the degree of Master of Philosophy has the author been registered for any other University award without prior agreement of the Doctoral College Quality Sub-Committee.

Work submitted for this research degree at the University of Plymouh has not formed part of any other degree either at the University of Plymouth or at another establishment.

This study was financed by the School of Biological and Marine Sciences (formerly the School of Marine Sciences and Engineering).

A program of advanced study was undertaken, which included independent research and analysis.

Word count of main body of thesis: 26,789

Signed_____

Date _____26/09/2018_____

ABSTRACT

Mixing and Dispersion of A Small Estuarine Plume

Megan Marie Sheridan

Entrainment velocity, salt flux and the turbulent diffusivity of salt are estimated in the outflow of a small, radially spreading buoyant outflow, just outside of the Teign Estuary mouth, as a means to compare mixing dynamics between very small and larger–scale estuarine and river plumes, and build on a scant knowledge base regarding the former. The analysis was made using a control volume approach, based on the conservation of momentum, volume and salt, from a Lagrangian perspective. Drifting buoys were used to accomplish this. The analysis was based on that employed by McCabe et al. (2008), with some modifications to fit a small-scale outflow, namely: repeat deployments, shorter drifter tracks, and deployment-specific criteria used for choosing the plume base, a step in the analysis used to calculate vertical entrainment, flux and diffusivity. In addition, temperature was used as a proxy for salinity, and this is evaluated in the results. Overall results were compared to a similar study, which was conducted in the Columbia River plume, a system much larger in scale to the Teign. Drifter experiments were conducted on multiple days, under different conditions (i.e. wind, tides, river flow), and those results are discussed briefly, but the focus is on one specific day, April 3, 2014, where conditions most closely matched those of the comparison study, and those results are compared between the two systems. Entrainment velocity was measured along the drifter tracks, in the near-field plume, where shear-induced mixing dominates. Drifter track subsections were chosen so as to avoid source or frontal dynamics, the plume base was chosen for individual deployments as the plume dynamics could change relatively quickly, and repeat deployments were conducted as a way to look at near-field plume evolution over the course of the ebb (and with a smaller plume, time allowed for this) . On April 3, the mean value for entrainment velocity for the four deployments chosen in the Teign outflow was 4.3×10^{-4} ms^{-1}. The mean cast value was slightly higher at 7.6×10^{-4} ms^{-1}, as casts values were typically measured at the beginning of the drifter tracks. Entrainment values at the cast sites were calculated in the same way as the track values, taking plume thickness from hydrographic casts, as a means to evaluate accuracy of track values, which are based on a modelled plume

thickness. A rough estimate for the mean entrainment velocity for one pair of drifters used in the Columbia River was 9 x 10^{-4} ms^{-1}, approximately double that of the Teign, but within the same order of magnitude. Salt flux values ranged from 0-5 x 10^{-2} psu ms^{-1} and from 0-3 x 10^{-2} psu ms^{-1} for the Teign and the Columbia, respectively, and diffusivities ranged from 0.5-5.8 x 10^{-2} m^2s^{-1} and from 0.2-9.6 x 10^{-3} m^2s^{-1}. With a similar range of entrainment and salt flux values, and almost an order of magnitude difference between diffusivity values, it was determined that weaker density gradients in the Teign are responsible for the latter, and that this increased level of mixing results in a larger horizontal horizontal salinity gradient, which balances out the terms in the entrainment equation that are related solely to the physical size of the system (i.e. plume thickness, velocity and the vertical salinity gradient). This higher level of mixing of a smaller physical entity, supports the view that smaller plumes mix more thoroughly over a shorter timescale, resulting in a larger impact to the local environment into which they flow.

CONTENTS

List of Tables

LIST OF FIGURES

LIST OF ABBREVIATIONS AND ACRONYMS

°C – Degrees celsius

B – Buoyancy Flux

B – Distance between drifters (in meters)

c – Interfacial wave phase speed

c – Internal (gravity) wave phase speed

f- Coriolis parameter

Fr_d – Densimetric Froude number

Fr_f – Frontal Froude number

Fr_i – Dimensionless internal Froude number

g – gravitational acceleration (9.81 ms^{-2})

g'- reduced gravity

h – partial depth, or plume thickness in meters

H – Total water depth

hshw – Hours since high water

K – Kelvin number

kgm^{-3} – Kilograms per meter cubed

km – Kilometer

K_q – Vertical eddy coefficient

K_s – Diffusivity of salt (in meters squared per second)

K_ρ – Diffusivity of density (in meters squared per second)

L – Characteristic length scale (Kelvin number)

LAT – Lowest astronomical tide

m – Meter

ms^{-1} – Meters per second

ms^{-2} – Meters per second squared

N – Brünt Vaisala Frequency

N_{int} – intrinsic frequency (Rottman and Simpson, 1983)

P – Shear production

psu – Practical salinity unit

q – Dimensionless volume flux

Q – Volume flux

q_e – Entrainment velocity (Pritchard, 2000)

r – Constant friction coefficient (bottom or internal, Garvine, 1995)

R' – Internal Rossby radius of deformation

Re – Reynolds number

Re_b – Buoyancy Reynolds number

Re_Z – Reynolds number for boundary effects

Ri_B – Bulk Richardson number

Ri_E – Estuarine Richardson number

Ri_f – Flux Richardson number

Ri_g – Gradient Richardson number

S – Shear

S_e – Entrainment salinity

S_eW_e – Salt flux (in psu meters per second)

T_e – Entrainment temperature (in degrees Celsius)

U – Current velocity (in meters/second)

u – East-west flow component

v – North-south flow component

V_E – scaled Ekman volume transport (Garvine, 1995)

W_e – Entrainment velocity (in meters per second)

W_s – Wind strength index (Garvine, 1995)

W_p – Theoretical width of plume

t_{tilt} – Wind strain timescale

x – streamwise direction (current study)

y – stream-normal direction (current study)

z – vertical direction

ΔS – Salinity anomaly (between plume and ambient)

ΔT – Temperature anomaly (between plume and ambient)

ε – Turbulent dissipation rate

η – Kolmogorov scales

λ – Plume slenderness

ρ - density

LIST OF APPENDICES

1 INTRODUCTION

Estuaries exist as a transition between inland watersheds and the coastal ocean. Estuarine plumes form as brackish water flows from an estuary, through a narrow opening, and into the more saline, dense coastal waters. The dynamics involved in plume formation, development, and ultimate dispersal are fundamentally important in the contribution they make to the local environment.

The contribution of freshwater to the margins of the ocean basins is important at both local and global scales. Anthropogenic effects, including nonpoint pollution and nutrient input, are predicted to have the most impact to marine environments within hard and soft continental shelves and rocky reefs, with the English Channel and North Sea existing amongst the highest risk areas on the planet (Figure 1.1, Halpern, 2008). In addition, process studies looking at small local freshwater discharges help to inform researchers about small and large scale buoyant coastal flows (Garvine 1991, 1995), and this coastal freshwater input is influential in circulation at the coastal margin (Yankovsky and Chapman, 1997). This influence will continue to increase as climate changes and freshwater input increases, which is why this contribution has begun to be incorporated into various Global Circulation Models (Garvine and Whitney, 2006).

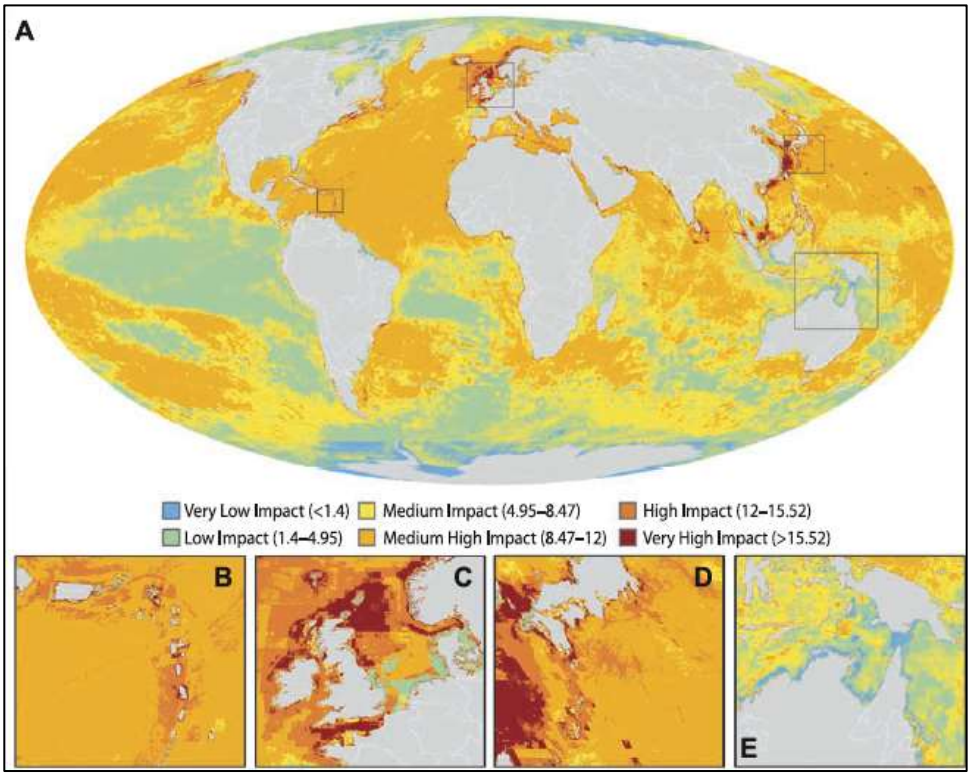

Figure 1.1: Global map showing predicted anthropogenic impact, including nonpoint pollution and nutrient input, from Halpern 2008.

Plumes occur on multiple scales. All plumes are different in the way they form and develop, and dynamics are governed by their scale and the unique environments in which they exist. How they behave and the way in which they mix with ambient seawater are largely determined by factors that include: volume of freshwater input, bathymetric features, estuarine variability, mouth characteristics, shelf dynamics, and external forcings such as wind, tides and waves. Plumes have been classified by Garvine (1995) as being large or small, based on five independent variables, the primary of which is the Kelvin number, $K \equiv \frac{\gamma L}{c/f}$, or, the ratio of the primary physical length scale to the baroclinic Rossby radius. Plumes that are 'K small' are considered small scale plumes, with strong advection terms and Froude numbers (ratio of buoyant water velocity to the internal wave phase speed) of order unity, but little influence from the Coriolis effect. Small scale plumes tend to spread radially, while large scale plumes form a coastally trapped current that flows in the direction dictated by Coriolis and other effects (i.e. wind) (Garvine,1982; Chant, 2012).

Much of the literature focuses on large scale plumes ("K large"), and the argument here is that small scale plumes are just as important, if not individually, then collectively, as they are likely to far outnumber large scale plumes, especially along the UK coastline. But collective global impact aside, they are important on the local scale, as they are instrumental in governing the transport of anthropogenic and other materials (i.e. sediment, nutrients, contaminants, larvae) into the local marine environment (Aguilar-Islas and Bruland, 2006; Hill and Wheeler, 2002; Lohan and Bruland, 2006; Bruland et al., 2008, Buck et al., 2007). Small scale geophysical plumes are thought to mix more quickly and presumably disperse locally (Horner-Devine et al., 2014), moreso than their larger scale counterparts, whose buoyant effluent may move offshore or impact coastline further away from the plume's source. That said, actual evidence in the literature of the former is scant (Luketina and Imberger, 1987/1989; Pritchard and Huntley, 2002/2006), which will be addressed in the current study. This directly affects both local sediment dynamics and water quality, which may impact public health, local marine populations, as well as beach morphology and dynamics. Even further, there is literature that describes what are considered to be "K small" plumes (i.e. Connecticut River), but these are still considerably larger than the plume investigated in the current study, and it is as yet unknown to what extent these even smaller geophysical, or "micro", plumes exhibit behaviour that is different from the classical small and large scale geophysical plumes.

To gain a better understanding of how plumes contribute to the flux of materials, one must first focus on two basic features: how individual plumes behave under different conditions and how they mix with the ambient coastal ocean. In Chapter 2, the following topics are reviewed: general plume characteristics (i.e. shape, scale), properties of buoyancy driven or gravity currents and shear-induced mixing in plumes, as well as the effects of external forces such as wind and tides.

In the chapters that follow, first, the current study is introduced in Chapter 3, along with a description of the study that inspired it; as well as the methods, instrumentation and data analysis. Results are presented in Chapter 4, and then discussed in Chapter 5.

2 LITERATURE REVIEW

2.1 Plume structure

River plumes and estuarine plumes differ in that river plumes occur when rivers flow directly into the coastal ocean, forming a thin lense of mostly freshwater on top of the ambient seawater. In contrast, estuarine plumes form when an influx of saltwater into a river valley creates an estuary, and the water that returns to the coastal ocean is brackish (Mann and Lazier, 1991). In either case, a plume may be defined as a buoyant body formed when fluid (or gas) of one density flows into fluid or gas of a different density, and a geophysical plume exists as a naturally ocurring system, as opposed to outflows that result from man-made structures like thermal power plants. Plumes are surrounded by fronts, where there exist sharp density gradients delineating the transition from plume fluid to that of the ambient fluid that surrounds it (Garvine, 1974; Simpson, 1995). In the case of estuarine plumes, the stability of the frontal feature is determined mostly by salinity, rather than temperature (Garvine,1974; Mann and Lazier,1991).

Oceanic fronts have long been associated with increased concentration of particulates and often increased biological activity (Zaneveld et al., 1969; Le Fèvre, 1987), and plumes are no exception, as many have been characterised in this way (Kingsford and Suthers, 1994; Largier, 1993; Mann and Lazier, 1991; Morgan, 2005).

Plumes behave as gravity currents in a two-layer density, or buoyancy, driven flow, with a "head", or leading edge, behind which intense mixing occurs (Figure 2.1). Due to the buoyancy differences between the two fluids, as the head advances, water flows toward the front from both sides and then plunges underneath the advancing plume, creating a layer of mixing on the underside of the plume where ambient water is entrained (Garvine, 1974; Simpson and Britter, 1979; Luketina and Imberger, 1989).

Large plumes (e.g. the Columbia River) may be separated into four distinct (spatial and temporal) zones: the source, tidal plume, recirculating plume (Yankovsky and Chapman, 1997; Horner-Devine et al., 2009), and far-field plume, and there exist similarities between the behaviour in the tidal region of large-scale plumes and the behaviour of smaller scale plumes (Horner-Devine, et al., 2009; Kilcher and Nash, 2010) and it is these similarities which receive most attention in this review. The similarities are that non-linear terms, like the inertial force of the outflow, dominate, at least initially, while Coriolis and wind have less of an impact, if any.

The source region exists in the vicinity of the estuary mouth. It is where the plume 'lifts off' from the seafloor, due to density differences between the effluent and receiving waters. Most mixing (about one third) is thought to occur in this zone (Horner-Devine et al., 2009; MacDonald and Geyer, 2004), and turbulent dissipation and shear exist in abundance, often extending to the seafloor and causing sediment resuspension (Spahn, et al., 2009). The tidal plume contains the water that is leaving the estuary on the ebb tide. It can exist as a jet and then as a buoyant structure that radially spreads, and is at least initially independent of the earth's rotation.

The recirculating plume is the bulge region, where water is affected by both the earth's rotation and outflow momentum. Water in this region accumulates from previous ebb tides, and may have a shelf residence time of 0.5 to 4 days, depending on the wind conditions.

Finally, the far-field plume is a mesoscale feature that is governed by buoyancy, the earth's rotation, and wind-forcing, and it is in this region where the final mixing of freshwater and seawater takes place and estuarine water is delivered to the coastal zone (Kilcher and Nash, 2010).

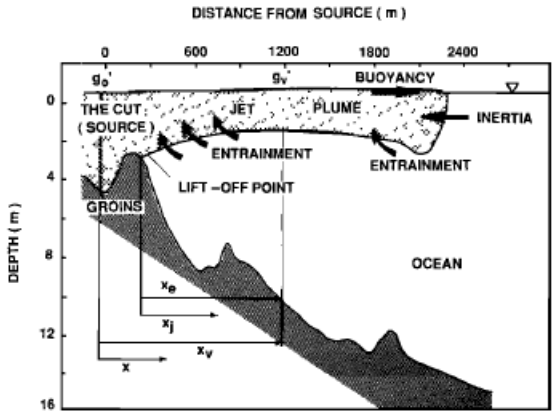

Figure 2.1: An example outflow schematic from Luketina and Imberger, 1987

2.2 Gravity currents

Estuarine plumes in their totality are in essence gravity, or buoyancy, currents. Simpson (1999) described the movement of a gravity current as similar to a dam breaking. The movement of the current is governed principally by gravity, and as the force of gravity acts downward on a parcel of water, potential energy is converted to kinetic energy as it spreads. Gravity currents occur when a volume of air or liquid of one density flows into that of a different density, and in this case, it is when lighter, fresher water flows from an estuary into the denser, saltier waters of the coastal ocean. If viscous forces are small, then they are driven primarily by gravity, as well as inertia.

According to Simpson (1982), there are two distinct regions in a gravity current: the head, or leading-edge, and the tail. The head region is preceded by a front, where there generally exists sharp horizontal density gradients and strong downwelling. It is deeper than the flow behind and moves at a velocity U that is dependent upon various factors, including the depth of the current h relative to the overall water depth H. In addition to these factors, the head structure may also be influenced by the dynamics of the surrounding flow environment, including the velocity and direction of ambient coastal currents, or whether it flows over a sloping bottom (Whitehead and Chapman, 1986; Garvine, 1999; Avicola & Huq, 2002).

Mixing occurs when density differences lead to high Reynolds numbers, or $Re = Uh/v$, where U_1 is the frontal velocity, h is the depth of the current, and v is the kinematic

viscosity. As the Reynolds number increases, until it reaches 1000, over which all gravity currents exhibit the same behavior, shear overcomes viscosity and billows due to Kelvin-Helmholtz instabilities may be formed on the underside of the gravity current. The billows may break down in complex flows, but mixing will still occur. Entrainment out of the front, which quantifies the degree of mixing, in this case characterized by the volume flux Q, or the ratio of the mean overtaking speed of the tail, U_4, to the front speed, U_1, was found to be close to 0.15 in all cases by Simpson and Britter (1979a) and experimentally in the field by Luketina and Imberger (1987). This term was later non-dimensionalised with g' and U_1 to form $q=Qg'/U_1^3$. Applying Britter & Simpson's (1978) theories to plume structure, they outlined something similar to the figure below (Figure 2.2), which was modified by Marmorino & Trump (2000) and Luketina & Imberger (1997) and validated in the Columbia River plume by Orton and Jay (2005).

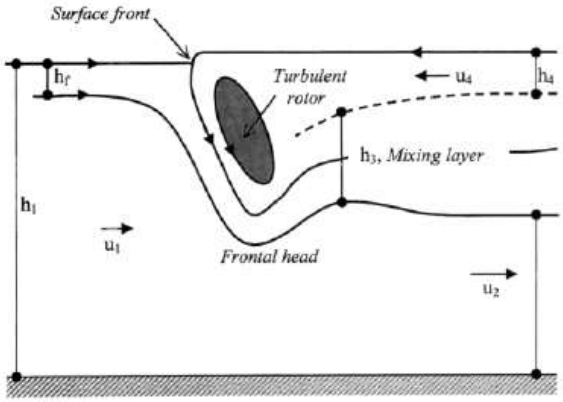

Figure 2.2: Schematic of plume structure in accordance with gravity current theory, velocity variable *u* is represented by *U* and h_1 by *H* in the text for consistency, from Marmorino and Trump, 2000.

The independent variables that represent gravity current structure (Figure 2.2) are as follows: the total depth of the fluid H; the reduced gravity, $g' = g(\rho_1-\rho_2)/\rho_1$, where ρ_1 is the uniform density of the ambient water, ρ_2 is the uniform density of the gravity current fluid, and g is the gravitational acceleration; and Q, or the volume flow per unit width into the gravity current head from the direction of the source. The dependent variables are h_4, the depth of the buoyant fluid measured well behind the head in the tail region of the gravity current, and U_1, the velocity of the oncoming flow required to hold the head

of the gravity current steady in a fixed frame of reference, or the frontal velocity in a stationary ambient fluid. The last of the values are h_2, the depth of the ambient fluid underneath the gravity current; U_2, the velocity of the same fluid; h_3, the thickness of the mixing layer; U_3, the velocity of the mixing layer, and $U_4(Q/h_4)$ is the flow into the tail of the gravity current.

The frontal Froude number, defined as $Fr_f = U_1/c$, *where* $c = (g'h_4)^{1/2}$, is the ratio of the frontal velocity to the interfacial wave phase speed within the gravity current. It depends on the relative thickness of the plume to the ambient water depth (h_4/H) and the dimensionless volume flux parameter, q (as described above). The frontal Froude number varied between 1-2.3 in Britter and Simpson's (1978) experiments, with it being 1 for a fractional depth of 1/5 and up to 2.5 as the fractional depth approached 0.

Froude numbers are significant in that they provide insight into the stability of two–layer flows. For $Fr_f < 1$, flow is subcritical, and for $Fr_f > 1$, flow is supercritical (Garvine, 1984). Others have defined this supercritical flow limit as existing within the range $1 < Fr_f < 2^{-1/2}$ (Benjamin, 1968; Shin et al., 2004; Didden and Maxworthy, 1982; Marmorino et al., 2004). Britter and Simpson's experiments above produced Froude numbers significantly higher than this upper limit, and determined this outcome to be the result of adding mixing to the dynamics. These Froude numbers were validated in the field (Luketina and Imberger, 1987- Figure 2.3). Frontal Froude numbers in excess of 2 cause shear instabilities, which leads to breaking waves, and therefore mixing, just behind the head region, or turbulent roller (Garvine, 1984). For supercritical flows in geophysical contexts, Chao (1988a) and Kourafalou (1996) have slightly different approaches with regard to this classification, as will be described in a subsequent section.

Mixing behind the roller leads to entrainment, mostly in the region underneath the plume (Figure 2.2), from the leading edge to as far as 200 m behind (Luketina and Imberger, 1987). Pritchard and Huntley (2002) found evidence of multiple hydraulic jumps in the region 30-50 m behind the roller, something that they think could be similar to wave-like undulations as described in Massey (1989).

According to the 3D model of Garvine (1984), assuming a radial surface plume with constant source flux, and neglecting wind stress, mixing and Coriolis acceleration, when the frontal Froude number increases beyond a critical value (greater than 2, but dependent on vertical profiles of ρ and U_4) , mixing then causes the layer just behind

the roller, or leading edge, to become thinner until nonexistent, and a new front may then form just behind. This process then leads to the additional formation of multiple fronts. Chen (1980) produced similar 3D model results, neglecting entrainment and varying flow behind the head, and confirmed these results experimentally. Luketina and Imberger (1987) also found evidence of multiple fronts, only these were moving at a speed close to the overtaking speed, rather than remaining stationary relative to the front.

Lastly, with regards to the velocity of the leading edge, a dimensionless internal Froude number, or $Fr_i = k(g'h)^{1/2}/N_{int}H$, where k is a quantity, given in Rottman and Simpson (1983), that depends on h/H, N_{int} is the intrinsic frequency and H is tank height, equivalent to $1/\pi$ defines a critical limit between two types of flow with regard to internal wave generation. For $Fr_i \leq 1/\pi$, multiple waves are generated, and each wave interacts (is released from the head, moves upcurrent, reflects off of an object (e.g. channel wall) and propagates back toward head) effectively slowing down the gravity current head, or creating oscillations in the velocity. For $Fr_i > 1/\pi$, one or more waves may be generated, but only the first appears to affect the propagation of the gravity current head, and this may be due to the decrease in energy caused by the generation of the wave (Maxworthy et al., 2002).

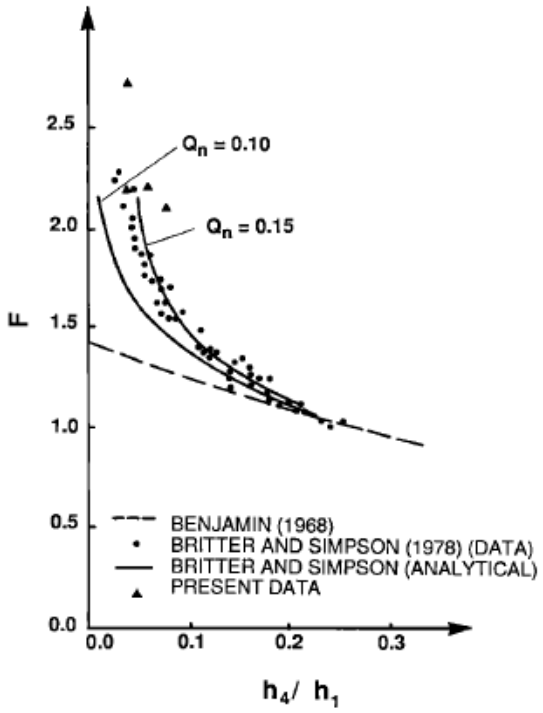

Figure 2.3: Frontal Froude number versus fractional depth for the Leschenchault plume during September 1984, as compared to previous theoretical data from Benjamin (1968), and analytical (and experimental) data from Britter and Simpson using different values of Q_n (1978), from Luketina and Imberger, 1987.

2.3 Fronts

Plumes are separated from the ambient sea by sharp gradients known as fronts. Oceanic fronts are typically characterized by vertical or horizontal shifts in water properties such as density, or in the case of density-compensated fronts, salinity and temperature, and develop as a sloping interface between two distinct water masses. In an estuarine context, they may appear as channel or supercritical plume borders, as well as tidal intrusion fronts, or those fronts that appear as dense seawater enters an estuary on an incoming tide and subducts beneath estuarine brackish water (Largier, 1992). They appear as convergence zones with potential increases in shear-induced mixing, which may encourage the transport of organic and inorganic materials between the seafloor and water column, or the ambient shelf water and plume, and yet they are persistent in time (Garvine and Monk, 1974; Orton and Jay, 2005). To the eye, fronts may be

represented by strong colour differences, foam lines, or the accumulation of detritus and other biological materials (Knauss, 1957; Cromwell and Reid, 1956; Zaneveld, et al., 1969; Pingree, et al., 1975).

Figure 2.4: Image of front from the Teign plume, April 1, 2014.

Density differences across plume fronts may be at least an order of magnitude larger than other observed oceanic fronts (Figure 2.5, Garvine and Monk, 1974). For larger outflows such as the Columbia River, density and velocity changes have been measured in the range of >9 kgm^{-3} for the former and >1 ms^{-1} in <100 m for the latter, with vertical velocities of >0.5 ms^{-1} (Kilcher and Nash, 2010). For the Connecticut River, the frontal velocity shift was >0.8 ms^{-1} and the density change was 9 sigma-t units (Figure 6, Garvine and Monk, 1974). For smaller outflows, such as Koombana Bay, the density difference is closer to 1 kgm^{-3} and the velocity difference 0.3 ms^{-1} with vertical velocities of 0.10 ms^{-1} (Luketina and Imberger, 1987). For a discharge like the Teignmouth plume, vertical velocities were calculated as being up to 0.08 ms^{-1}, and horizontal velocities changed by 0.15 ms^{-1} (Pritchard and Huntley, 2002).

Mass and momentum balance is responsible for all movement (i.e. surface convergence) in the frontal region and the entrainment caused by the resulting shear instabilities affects the plume's shape and size in many ways, to be explored in detail later. In addition, frontal dynamics allow changes in direction to match ambient currents, and

dictate that outlet channels with more than an approximate 66° turn may result in plume detachment from the coast (Garvine, 1982; O'Donnell, 2008).

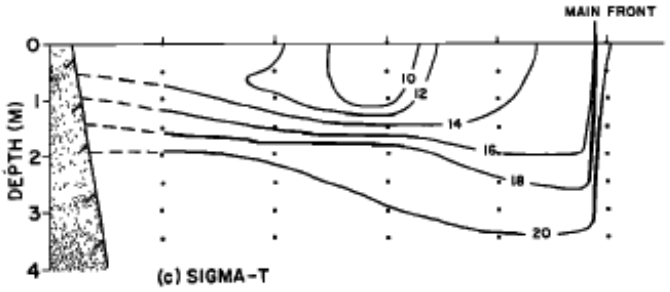

Figure 2.5: Density contours from a section of the Connecticut River plume, from Garvine, 1974.

Front propagation speed may be calculated as the sum of the jet extent translation speed and the radial plume spreading rate, and constant frontal motion is strongly influenced by a linearly increasing estuary discharge rate, more so than internal plume or frontal dynamics (Garvine, 1984; Jay, 2010; Kilcher and Nash, 2010). In the Columbia River studies, simple frontal structure has been measured, as described in classical gravity current literature, as well as complex frontal structure, which occurs as a result of frontal interaction with plume water from previous ebb tides. This may produce multiple fronts, 'reverse fronts', or non-linear internal waves (NLIW's) that emanate from the frontal region. (Luketina and Imberger, 1987; Garvine, 1984; Kilcher and Nash, 2010; Nash and Moum, 2005).

2.4 Scales and classification schemes

Generally speaking, plumes are a product of the environment in which they develop, and the shape and behaviour of the gravity current develops accordingly. Large outflows will propagate differently than smaller outflows; and topography, bathymetry, external forces and ambient cross-flows all have an effect.

As a result, plumes form at different scales and may be classified accordingly. Kourafalou (1996), Yankovsky and Chapman (1997), Garvine (1987,1995) and others all presented different classification schemes aimed at describing plumes in various

Vertically integrated continuity eqn:

$$\frac{\partial}{\partial x}(hu) + \frac{\partial}{\partial y}(hv) = 0 \qquad (1)$$

Vertically averaged x and y momentum eqns:

$$\frac{\partial}{\partial x}(u^2) + \frac{\partial}{\partial y}(uv) - fv = -\frac{1}{\rho_0}\frac{\partial p}{\partial x} + \frac{\tau_w^{(x)}}{\rho_0 h} - \frac{\tau_b^{(x)}}{\rho_0 h} \qquad (2)$$

$$\frac{\partial}{\partial x}(uv) + \frac{\partial}{\partial y}(v^2) + fu = -\frac{1}{\rho_0}\frac{\partial p}{\partial y} + \frac{\tau_w^{(y)}}{\rho_0 h} - \frac{\tau_b^{(y)}}{\rho_0 h} \qquad (3)$$

Where x is the along-shelf direction, y is the cross-shelf direction, h is the buoyant layer depth, u is the along-shelf velocity, v is the cross-shelf velocity, p is the pressure, τ_w is the wind stress, f is the Coriolis parameter, and τ_b is the stress at the base of the upper layer, from Garvine (1995)

contexts. Of almost primary importance, Garvine (1987) distinguished between non-rotating and rotating plumes, or plumes that are effected by Coriolis forces, according to the Kelvin number, an indicator of the physical size of the plume. Garvine (1995) then enhanced this classification scheme using a specific set of properties, combinations of which determine the overall classification. The continuity and momentum equations were vertically averaged over the buoyancy current, ignoring variables based on time and disregarding entrainment on the underside of the plume (Equation 1). After scaling analysis, five parameters remain that are used to differentiate between small and large plumes (see Table 1). They include: plume slenderness (the ratio of the plume's width to its length), γ; the Kelvin number, $K \equiv \frac{\gamma L}{c/f}$, or, the ratio of the primary physical length scale to the baroclinic Rossby radius; the Froude number, $Fr_d \equiv U/c$, the ratio of plume velocity to the interfacial wave phase speed; wind stress, represented by the scaled Ekman volume transport $V_E = (HU)$; and the basal friction coefficient, $r/(fH)$, where r represents a constant friction coefficient, corresponding to either bottom or internal friction as appropriate, and f is the Coriolis parameter. The Kelvin number is of primary

importance, and Garvine (1995) differentiates between plumes that are K-large ($K>>1$) and K-small ($K<<1$). 'K small' plumes (e.g. Connecticut, Koombana Bay) tend to be fast-flowing (at least initially) and radially spreading, with large frontal discontinuities and potential for internal hydraulic jumps. Coriolis does not have an appreciable effect, so the momentum balance exists between advection and buoyancy (and perhaps wind and basal friction in some cases). 'K large' plumes (e.g. Delaware, Chesapeake, Columbia), on the other hand, are large enough to be influenced by the Coriolis effect, advection becomes less relevant, and the flow is considered semi-geostrophic. These plumes are rotating, and will turn and flow in the direction of Kelvin wave propagation, potentially forming coastally trapped currents or, depending on the level of mixing or the presence of upwelling winds, may break away from the coast and move further offshore (Kourafalou, 1996; Hickey and Hamilton, 1980).

Table 1: Parameter estimates from Garvine's (1995) classification scheme

Name	K	F	KF	$1/\gamma$	V_E/HU	r/fH
Point Beach	0.1	2.0	0.2	1	0.1	0.3
Mississippi	0.2	1.0	0.2	1	0.2	0.7
Amazon	0.6	0.6	0.4	2	0.01	5.0
Niagara	1.0	1.0	1.0	1	0.08	0.1
Alaska	1.0	0.3	0.3	6	0.02	0.08
Gaspé	2.0	0.4	0.8	10	0.01	0.1
Algerian	3.0	0.3	0.9	8	0.005	0.06
Rhine	3.0	0.1	0.3	5	0.2	0.7
Delaware	4.0	0.1	0.4	5	0.3	0.4
SAB	4.0	0.3	1.0	5	0.2	0.4
Norwegian	4.0	0.1	0.4	10	0.01	0.02
Scottish	10.0	0.1	1.0	5	0.05	0.1

Later, Kourafalou (1996) used 3-dimensional numerical models to delineate between supercritical and subcritical plumes based on a bulk Richardson number, or the ratio of buoyancy induced stratification to mixing. When $Ri_b > 1$, the plume is considered to be supercritical, when $Ri_b < 1$, the plume is subcritical. This means that large, buoyant plumes may result in meandering coastal currents via baroclinic instability while smaller, less buoyant discharges are more susceptible to increased mixing, a reiteration of the point that smaller outflows may have more impact closer to home.

Another important aspect of plume development is whether a plume may be considered bottom-advected, surface-advected, or a combination of the two (Yankovsky and Chapman, 1997). This is based on two length scales, the equilibrium depth, h_b, and the offshore distance, y_s. If the distance to the h_b isobaths is greater than y_s, a bottom-advected plume will form. If the h_b isobath is shallower than the inflow depth, a surface-advected plume will form as far offshore as y_s. If the h_b isobath is deeper than the inflow depth, but closer to the coast than y_s, a plume will form with both characteristics. Chapman and Lentz (1994) acknowledged earlier that plumes that reached to the bottom would behave differently than surface-advected plumes due to the friction encountered at the bottom.

In 2002, Lentz and Helfrich developed a scaling argument to predict surface or bottom-controlled plume behaviour in coastal gravity currents that exist away from the source in contrast to the Yankovsky and Chapman classification that applies to plumes closer to the source. The basic nature of the argument lays in the non-dimensional parameter c_w/c_α, or the speed limit of the nose over a steep slope/the speed limit of the nose over a shallow slope. If $c_w/c_\alpha << 1$, the gravity current is surface advected, and if $c_w/c_\alpha >> 1$, the gravity current is slope-controlled, and slope-controlled gravity currents are wider than their surface-advected counterparts (Lentz and Helfrich, 2002; Whitehead and Chapman, 1986).

In the case of the Merrimack plume, a sandbar exists at the mouth, with water depths of 3m occurring at low tide. This causes that plume to be bottom attached until just after the sandbar, unless the river flow is sufficient that the water is fresh enough to lift off. This is also likely with the Teign outflow, as similar structures exist near the estuary mouth.

When a plume transitions between bottom-attached and surface-advected, sediment resuspension becomes unsustainable, and any sediment that the plume is carrying begins to settle out of the water column. This settling rate, in addition to plume trajectory and velocity, collectively determine the fate of sediment in river plumes (Geyer et al., 2004).

2.5 Mixing

Mixing processes, governed by turbulence, affect multiple aspects of plume development. In a sense, plumes begin in the source estuary, where tidal currents, shear-induced mixing and freshwater outflow influence, and may even dictate, plume development and evolution (Nash et al., 2009). For surface-advected plumes, as water exits the estuary, constriction at the mouth and plume lift-off causes flow to accelerate (Armi, 1975). Prior to lift-off, the plume mixes through boundary layer mixing (i.e. bottom mixing), and shear-induced mixing at the edges. After lift-off, shear-induced instability created by momentum and stratification results in increased mixing at the edges of large plumes, and may to a greater extent mix smaller plumes (Chen and MacDonald, 2006). As ambient water is entrained, the density changes and the plume eventually begins to decelerate. Once this happens and the plume transitions from the near field to the far field, wind then becomes most important in the mixing and transport of plume waters in the coastal region and offshore.

2.5.1 Turbulence in plumes: a primer

As MacDonald et al. (2007) states, "it could be argued that turbulence is truly a phenomenon which is important across all scales of relevance to a particular flow field" implying its significance to the multiple scales important to plume development and evolution. Mixing is the result of the blending of water masses by turbulence which, in essence, is the result of an influx of energy that generates eddies. These eddies may exist at a variety of scales, the largest of which are denoted by L (the integral length scale; Taylor, 1935; Smyth, 2001) and the smallest by η (the Kolmogorov scales; Kolmogorov, 1941) in a turbulent flow, and these limits are determined by the physical boundaries of the flow. Energy is transferred between scales, from large (e.g. Kelvin-Helmholtz billows) to small (e.g. the Kolmogorov scales), and then is released as heat due to viscous forces.

Turbulence in estuaries and other shallow coastal flows is generated principally by shear, which is denoted by the shear production, P. Shear occurs as the currents interact

with solid boundaries, between layers of different densities, and the air-sea interface. This energy transfer must be balanced by the eventual loss due to heat. The rate at which this happens is denoted by the turbulent dissipation rate, or ε, and these two quantities must be in balance in steady, homogenous and unstratified turbulent flows (Monin and Yaglom, 1975; Osborn, 1974). In flows with stratification, unsteady turbulent kinetic energy or the advection/diffusion of energy, the balance can be described by the steady state turbulent kinetic energy budget equation (Gregg, 1987):

Defining turbulent kinetic energy as,

$$q^2 = \overline{u'^2} + \overline{v'^2} + \overline{w'^2} \tag{4}$$

The balance is :

$$\frac{\partial q^2}{\partial t} + u\frac{\partial q^2}{\partial x} + v\frac{\partial q^2}{\partial y} + w\frac{\partial q^2}{\partial z} = \frac{\partial}{\partial x}\left(K_q\frac{\partial q^2}{\partial x}\right) + \frac{\partial}{\partial y}\left(K_q\frac{\partial q^2}{\partial y}\right) + \frac{\partial}{\partial z}\left(K_q\frac{\partial q^2}{\partial z}\right) + 2P + 2B - 2\varepsilon \tag{5}$$

Variables with overbars represent the mean, and K_q denotes a vertical eddy coefficient. This, in cases of steady and homogenous turbulent flow, reduces to:

$$P + B - \varepsilon = 0 \tag{6}$$

Where P is shear production, ε is the turbulent dissipation rate, and B represents the buoyancy flux, and characterises the amount of kinetic energy/potential energy that is converted to potential energy/kinetic energy.. The left hand side of equation (5) is reserved for the changes and advection of the turbulent kinetic energy by the mean velocities and the right is for the diffusion of kinetic energy, in addition to sources and sinks of energy (Stacey et al., 2011).

The flux Richardson Number, Ri_f, which can be defined as:

$$Ri_f = -\frac{B}{P} \quad (7)$$

assuming a homogenous and isotropic turbulent field, is the ratio of the buoyancy term of the turbulence kinetic energy budget equation and the negative of the shear term of the same equation, and is a parameter that represents mixing mixing efficiency, or the amount of turbulent kinetic energy that is converted into potential energy through mixing against a density gradient, or positive buoyancy flux. It is also key in estimating eddy diffusivity from measurements of turbulent dissipation, and was found to be equal to between 0.15 and 0.2 in instances of turbulent mixing in the laboratory (Ivey and Imberger, 1991). In later studies, values for Ri_f have been found outside of this range (Gargett and Moum, 1995; Barry et al., 2001; Etemad-Shahidi and Imberger, 2001; Moum, 1996) and some think it has to do with the source of the turbulence, as grid-generated turbulence in the lab does not always produce the same results as shear-generated turbulence in the field or lab, which is an important distinction when evaluating how lab-based turbulence studies apply to the 'real-world'.

As mentioned briefly above, in shallow coastal flows, the following limitations, or length scales, are important when characterizing turbulent processes: the Kolmogorov scales, or the smallest turbulent scales where energy is dissipated as heat, based on the assumption that only the dissipation rate and viscosity are important; the length limitation due to Prandtl, which describes the distance from a solid boundary; and the Ozmidov scales, which describe the limitation imposed by competition between stratification and mixing, which is based on the buoyancy frequency. There must be enough space left by these three limitations for turbulence to fully develop. Using these length scales as guidelines, one may calculate dimensionless numbers that represent the ratios of inertial to viscous forces that indicate whether turbulence can exist, as in the Reynolds number for boundary effects, Re_z, or the buoyancy Reynolds number, Re_b, which describes the effects of the limits imposed by stratification. Even further, these length scales can be used to determine the overturn Froude and Reynolds numbers, which describe the energy-bearing eddies that make up turbulence, and it is the relationship between these parameters that may determine the magnitude of Ri_f (this is still under debate) and that describes the state of the turbulent energy field. The nature of the turbulence is thought to be affected by the mechanism that generates it, and in

laboratory situations the length scales imposed by the tank or numerical simulations may bias the resulting overturn Froude number and Ri_f, reinforcing the need for field measurements (MacDonald and Geyer, 2004). Overturn Froude numbers equal to one are generally expected in cases where Kelvin-Helmholtz billows are thought to be primarily responsible for turbulence production, as in the case of plume evolution (Ferron, et al., 1998; MacDonald and Geyer, 2004).

In estuarine and coastal environments (e.g. plumes), stratification often exists due to the combination of freshwater (or brackish) flow into (or out of) an estuary from rivers and seawater intrusion from the coastal sea. The stability of this stratification is also a key indicator as to whether the flow will become turbulent. The Brünt-Vaisala (buoyancy) frequency, N^2, is a measurement of the frequency at which a water parcel will oscillate around its position of neutral density when displaced in a region of linear density variation and is an indicator of the amount of stratification that exists:

$$N^2 = -\frac{g}{\rho_0}\frac{\partial \bar{\rho}}{\partial z} \tag{8}$$

Shear, on the other hand, exists when adjacent particles move at different velocities, as when near a boundary of some kind, and is defined as:

$$S^2 = \left(\frac{\partial U}{\partial z}\right)^2 + \left(\frac{\partial V}{\partial z}\right)^2 \tag{9}$$

Shear promotes turbulence, while stratification suppresses it. Taking the two relative to each other, one may calculate the gradient Richardson number, Ri_g:

$$Ri_g = \frac{N^2}{S^2} \tag{10}$$

As Ri_g increases, stratification dominates, as it decreases, turbulence and mixing increases. Conversely, turbulence reduces both shear and stratification.

Entrainment occurs as the result of turbulence generated by shear between two stratified layers. As in the case of a buoyant layer on top of an underlying dense layer of water, when enough energy is provided to increase shear to the point where it overcomes the buoyancy-induced stratification between the two layers, as in when $Ri_g < 1$, vortices, also known as billows or rotors as mentioned above, are formed. These billows engulf water from the less turbulent lower layer, entraining it into the more turbulent upper layer.

A few studies have looked at microstructure in river plumes, but most have focused on large and medium plumes, such as the Columbia and Fraser Rivers, respectively. As an example, Orton and Jay (2005) reported mixing rates estimated from a Thorpe overturn length-scale analysis of undulating CTD data captured in the Columbia River plume. They reported maximum values of dissipation ε and eddy diffusivity K_ρ as 10^{-3} Wkg^{-1} and 0.2 m^2s^{-1}, respectively, 50 m behind the plume front. Only a few have focused on smaller, or 'micro', geophysical plumes, and this includes the Leschenchault Estuary (Luketina and Imberger, 1987; 1989), which is similar in scale to the Teign plume. The results of the Leschenchault studies were amongst the first direct microstructure measurements in a river plume. They found that the entrainment velocity, dissipation, and turbulent displacement scale were all highest near the plume front, and decreased in magnitude with distance behind the front. The maximum entrainment velocity found was ~1.7 x 10^{-3} ms^{-1}, and this decayed exponentially to one-tenth this value 300 m behind the leading edge.

2.6 Regions of importance

Below is a description of the primary regions of influence used to discuss different stages of plume development and evolution: in the most general description there is the estuary, near-field plume, and far-field plume, and within these regions there are smaller divisions (i.e. source, lift-off, tidal plume). We will exclude the estuary here, as the current study does not focus on the estuarine environment.

2.6.1 Near-field plume

In the near-field momentum forces dominate, and the amount of mixing that occurs in this part of the plume may be equivalent to the far-field plume, which has a much bigger geographical footprint. There exists complex flow dynamics, and the flow rapidly responds to changes in the flow field in both the vertical and horizontal directions (Hetland, 2005). There is competition between dynamics: the flow accelerates as it lifts off and shoals due to density differences between plume and ambient water. Simultaneously, horizontal streamlines diverge due to the density anomaly, creating a lateral pressure gradient that may slow the plume down. Active mixing due to turbulence may then alter this lateral pressure gradient, thus limiting the divergence in streamlines (MacDonald et al., 2007). Understanding this complexity, and this dynamical balance, is important in understanding the dynamics of the near-field of any given plume (McCabe et al., 2009).

The near-field plume may be broken up and categorised in different ways, but what we are talking about here is the Luketina and Imberger "jet regime" or the near-field region described by Horner-Devine (2009) and Kilcher and Nash (2010): and in this region there exist different zones, each dynamically different and all regions of active mixing. The two regions that will be the focus here, in terms of mixing, are the lift-off zone (or source) and the tidal plume (or surface jet), having discussed the plume head or front (with leading edge and rotor) in previous sections.

Beyond this, the near-field plume may be further broken up into regions of mixing in the vertical direction, including a wind-stirred surface layer, stable layer, mixing layer, and quiescent layer (Luketina and Imberger, 1987 and 1989).

2.6.1.1 Source/lift-off

For surface-advected plumes, the source region of the outflowing plume is where the plume initially lifts off from the bottom due to density differences between incoming seawater and outgoing fresh or brackish water. The location of the lift-off itself may change, and is influenced by river outflow, tidal range (Horner-Devine et al., 2009) and

the amount of interaction with the bottom at the lift-off point (Chen and MacDonald, 2006). It is characterised by intense shear and turbulent dissipation throughout the water column, resulting in high bottom stress and sediment resuspension. Flow is supercritical, due to the narrowing of the channel at the mouth which forces the transition from subcritical flow, and salinity changes rapidly as seawater is entrained into the outgoing fresh or brackish water through turbulent mixing.

Bottom friction is 1-2 orders of magnitude more efficient at creating turbulence than shear-induced mixing, which is why the area just inside of the lift-off region is such a hotspot for mixing (MacDonald and Geyer, 2004; Chen and MacDonald, 2006). Chen and MacDonald found that in a thermal discharge from a power plant, mixing in the region from 1-200 m along the plume centreline was an order of magnitude larger than in the region from 200-800 m, and attributed that to the effects of bottom-friction.

This bottom friction activates mixing, which prevents ambient water from getting underneath the plume and depending on the amount of mixing, may push lift-off further offshore. Bottom friction is a direct result of the outflow dynamics (i.e. velocity shear), as well as bottom type. The lift-off point has been observed to be mobile in small and large plumes alike (e.g. Columbia River and thermal discharge) (Chen and MacDonald, 2004; Kilcher and Nash, 2010). The bottom stress may result in sediment resuspension, the level of which depends on the availability of fine sediments in that region, along with the Estuarine Richardson number Ri_E. This resuspension may have biological implications; acting as a mechanism for the transport of nutrients, which are associated with those sediments, up through the water column (Spahn et al., 2009).

Mixing continues to be intense at lift-off, with lower Ri_b values. Once the plume lifts off, shear-induced mixing at the base then creates a mixed layer at the base of the plume (Chen and MacDonald, 2006).

Plume processes may be similar at a wide variety of scales, although certain ones may have more influence at different scales (Chen and MacDonald, 2006). For instance, the size of the plume, or aspect ratio as Chen describes it, may be a factor in determining how important the different types of mixing are. After lift-off, shear stratified processes are the primary driver of turbulent kinetic energy production (Macdonald and Geyer, 2004), with larger plumes experiencing shear-induced mixing over a much larger area than smaller plumes (i.e. thermal plumes, or other very small geophysical plumes), making this process more efficient at mixing plume water with ambient water than the

bottom interactions described above, despite the latter being more intense. This makes shear-induced mixing overall more important, especially in larger scale plumes (Chen and MacDonald, 2006).

In terms of mixing in the source region, documented diffusivities near the mouth of the Fraser, Merrimack and Columbia Rivers have been in close agreement, and largely fall in the range of 10^{-2} m^2s^{-1} – 10^{-3} m^2s^{-1} (McCabe et al., 2008; MacDonald and Geyer, 2004; MacDonald et al., 2007). For studies in Koombana Bay, results were two orders of magnitude smaller, potentially closer to what would be expected to see in Teignmouth.

Mixing results in entrainment of seawater into the outgoing plume. Entrainment may be described as the rate of increase of streamwise volume flux within a turbulent region (Ellison and Turner, 1959; Morton et al., 1956; Nash et al., 2009), and the amount of entrainment that occurs wthin an estuary has implications on the resultant plume. This entrainment may be represented by the terms for the horizontal advection of freshwater ($\mathcal{F}_{adv}$) and the vertical turbulent flux of freshwater ($\mathcal{F}_{turb}$), based on the fraction of freshwater within a water parcel (Figure 7). The freshwater fraction is defined as

$$F = (s_0 - s)/s_0 \tag{11}$$

with s_0 as the salinity of pure seawater and s a representative plume salinity, and the advective and flux terms become

$$\mathcal{F}_{adv} = u\mathrm{F} \tag{12}$$

$$\mathcal{F}_{turb} = K_\rho dF/dz \tag{13}$$

with u as the velocity of the water parcel of interest. The ratio of $\mathcal{F}_{adv}$ to $\mathcal{F}_{turb}$ represents Ri_E, or the estuary Richardson number, which Nash et al. (2009) posit is a useful parameter in predicting plume properties including: median salinity, thickness, and turbulent mixing at the plume base, and that this may be applied to all river plumes, with some customisation.

2.6.1.2 Surface jet, or tidal plume, or transition and 2-layer regions

Continuing to use the terms developed for the Columbia River (during the RISE project), the tidal plume describes the region of the plume that includes the surface jet, or strongly stratified, energetic outflow from the estuary that has just lifted off from the source region. It accelerates as it shoals, due to the Bernoulli principle, which induces further mixing. Flow here is generally supercritical and is still moving in response to the inertial forces of the estuarine outflow. It is bounded by sharp fronts, and the Coriolis effect and wind are assumed to have less important roles. In the case of the Columbia River plume, this region can extend as far as 35 km from the source, and it is this region that is the focus of comparison with the Teign plume in the current study.

This region may be further broken up into the transitional and 2-layer regions, as described by Kilcher and Nash (2010). The transitional region being that which has just undergone lift off, and still shares certain characteristics with the source region, such as being strongly sheared, with TKE levels that are 1000 times background levels ($\varepsilon = O(10^{-4})$ WKg^{-1}). Surface velocities are double that of the front, and while shear-induced mixing is active, it is limited by the stratification between the plume and ambient water. Gravitational forces on the plume result in lateral spreading, causing the plume to thin, almost by half in the Columbia River plume (from 20 m to 10 m). At the centre of this region, diffusivities in this plume are $O(10^{-4})$ m^2s^{-1}).

The transitional region then gives way to the 2-layer zone, where the plume appears to be more well-mixed, with dissipation at the plume base ($\varepsilon = O(10^{-5})WKg^{-1}$).

As a result of mixing in both regions, additional seawater is entrained into the plume. In the horizontal direction, $\mathcal{F}_{adv}$ shifts from higher to lower salinity waters, with the freshest waters occurring just before low tide, although these values change with different tidal stages and river flows (Q_f). Similarly, in the case of vertical flux $\mathcal{F}_{turb}$, the plume is thicker and saltier during spring tides and low Q_f, and thinner and fresher during neap tides or high Q_f. See Figure 2.6 for a look at $\mathcal{F}_{turb}$, and how those values correspond with other mixing parameters, including shear, dissipation and diffusivity in this region (Nash et al., 2009).

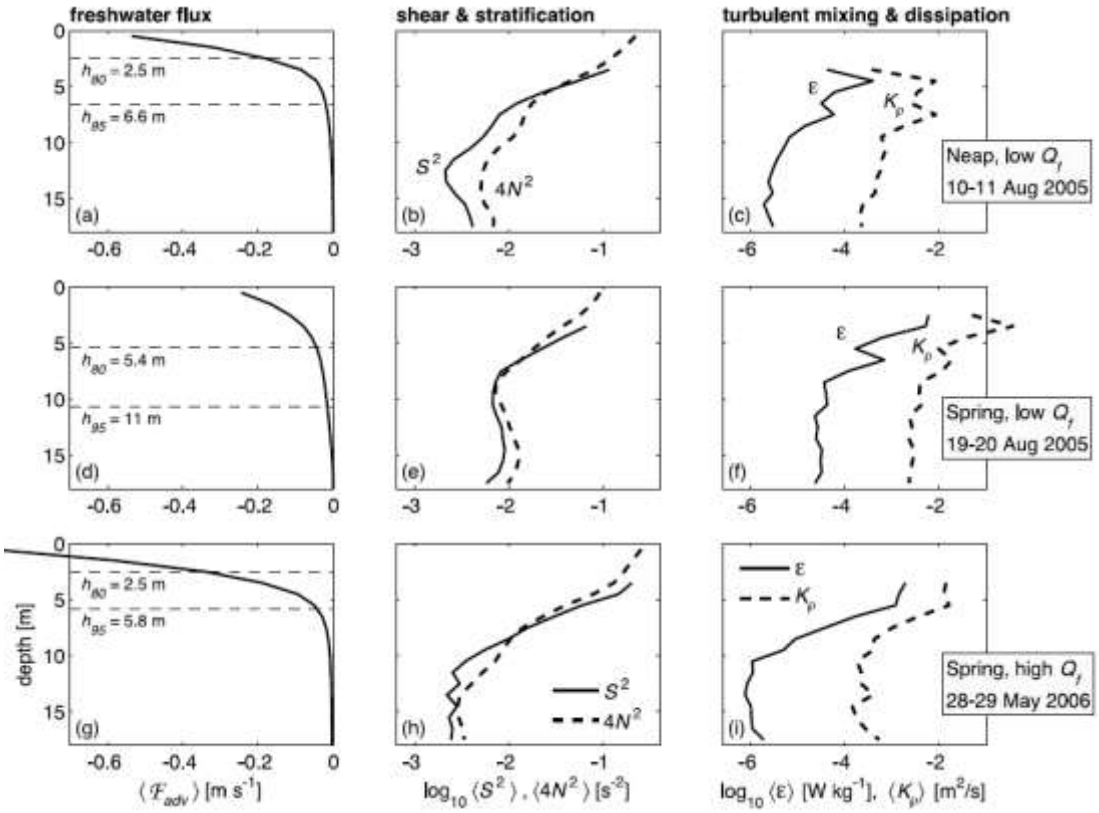

Figure 2.6: Time-averaged vertical structure in the near-field plume under 3 different flow conditions, where $\mathcal{F}_{adv} = uF$, u is velocity of the water parcel, F is the freshwater fraction $(s_0-s)/s_0$, s_0 is the salinity of pure seawater and s a representative plume salinity, S^2 is shear in this case, N^2 represents stratification, ε is dissipation, and K_ρ is diffusivity, from Nash et al., 2009.

2.6.1.2.1 Plume spreading

In the current study, the focus is on spreading in the near-field. Chen and MacDonald (2006) describe the relationship between mixing and spreading in near-field plumes as a "perplexing problem", and stresses that it is important to understand the mechanisms behind how a plume spreads and the effects of mixing on this process. In a two-layer flow, with a buoyant upper layer and a denser lower layer, the upper layer expands as it flows onto the lower layer and shoals as it does so. This causes the upper layer to accelerate according to the Bernoulli principle (drop in sea surface height = drop in surface pressure), leading to an increase in shear between the two layers. Due to the evolution of Kelvin-Helmholtz vortices, the flow becomes turbulent. This leads to

entrainment, as liquid from the less-turbulent layer is entrained into the more turbulent layer, and thus leads to the mixing of the two layers. For geophysical plumes, lateral mixing is assumed to be negligible due to the small aspect ratio as compared to engineering-scale plumes. Entrainment is thought to happen vertically. The entrainment velocity, w_e, is a quantity that represents the mixing of water properties (e.g. salt, heat, density, momentum) from the lower layer into the upper layer, and it tends to be greatest where the plume is thinnest (Chen et al., 2009). In addition, Hetland (2010) posits that Q_f, or the freshwater flux into the plume, rather than Q, or the overall discharge at the mouth, is the primary driver for mean entrainment rates of water into the plume. Local entrainment appears to be driven by the density anomaly, both reinforcing the importance of the influence of buoyancy on entrainment.

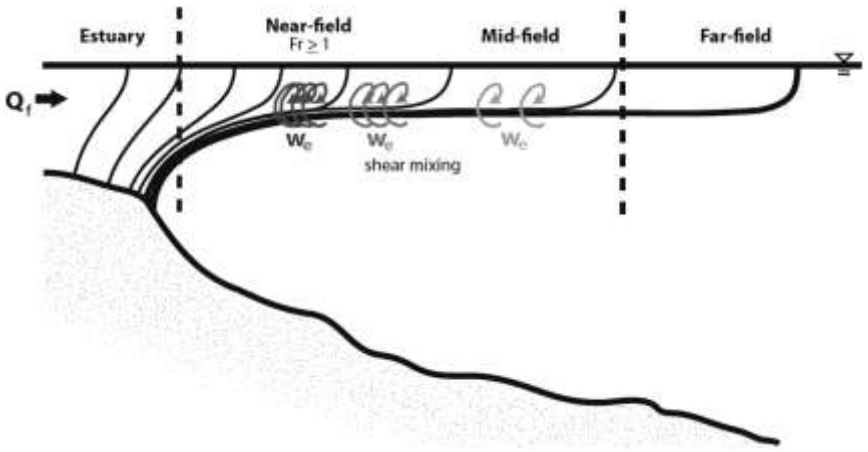

Figure 2.7: A schematic showing the variability in intensity of entrainment according to plume region, with Q_f indicating freshwater flow; and dark grey, medium gray, and light gray representing strong, medium, and weak entrainment, from Cole and Hetland, 2015.

Plume spreading is directly related to the local internal gravity wave speed. The percent change in plume width is proportional to the radial distance from the mouth, as are other plume properties such as surface salinity, mixing, spreading rates, etc. Mixing reduces the density anomaly between the plume and ambient water, which then alters the plume thickness and thus the local internal gravity wave speed, causing the plume to slow down. At the same time, spreading results in a thinning of the plume, which may cause surface velocities to increase. Interestingly, both mixing and momentum can alter the

Froude number, as it is related linearly to the velocity and to the square root of the density anomaly, and both may alter it by as much as an order of magnitude. However, the Froude number in the near-field is typically always at or very close to 1, meaning that mixing and spreading may overall be in balance, with both exerting competing influences on the overall plume structure. Mixing also affects the spreading rate in that the local interfacial stress term, which is determined by mixing in the stratified shear layer, directly influences the radius of curvature, and thus the spreading rate (Hetland and MacDonald, 2008; MacDonald, 2009).

The balance of dynamics at play during the evolution of a radially spreading plume may be described in terms of the momentum balance in the streamline-normal direction. The terms include: acceleration, advection, streamline curvature, Coriolis forcing, barotropic forcing, and stress. In the Merrimack River plume, the near-field (1 km) lateral momentum balance was dominated by the streamline curvature, or the centrifugal force term created by the creation of centripetal force due to a pressure gradient across a streamline, which was balanced by buoyancy, interfacial stress and Coriolis forces. In the far field, Coriolis dominated (Chen et al., 2009). In the Columbia River, momentum balance analysis using Lagrangian surface drifters and a ROMS model also describes the forces primarily responsible for plume spreading in different regions of that plume. Those results elucidated the importance of both streamwise and stream-normal contributions to spreading, some more than others with greater distance from the source. They used a streamwise-normal coordinate system (Hence and Luettich, 2003). Spreading appears largest where cross-stream processes are involved. Closer to the mouth, they found that the streamwise momentum balance exists primarily between a pressure gradient caused by elevated sea surface heights associated with the buoyant freshwater, and the advection of the flow and friction, the latter especially at the mouth. The stream-normal balance changes slightly through the ebb and into slack, but the key players are streamline curvature (or centrifugal forces), advective acceleration, the cross-stream pressure gradient and Coriolis force. As the plume moves further from the mouth, the stream-normal balance becomes more dominated by centrifugal and Coriolis forces, with some contribution from the pressure gradient, the combination of which defines 'gradient wind' or the cyclostrophic currents mentioned in bulge literature, which will be discussed briefly in a subsequent section (McCabe et al., 2009).

Finally, after momentum decreases and gives way to buoyancy, the plume decelerates due to an adverse streamwise pressure gradient, friction, and mixing, the latter of which,

if not done consistently, may affect how Coriolis forces act on the plume, further enhancing deceleration or aiding in plume breakdown. Deceleration may happen quickly at first and then slowly, based on the degree of mixing, or will be more dependent on timing and volume of the source outflow, depending on the school of thought (Garvine, 1984 vs. Kilcher and Nash, 2010).

Under circumstances where plume expansion is limited by local bathymetry or ambient seawater conditions, reduced streamwise gradients of velocity may affect the turbulent buoyancy flux. In plumes with limited ability to expand, acceleration will be reduced, resulting in less intense mixing at the plume base (MacDonald, 2004).

2.6.2 Far-field plume

The transition between the near and far fields has been characterised in various ways. One accepted idea is that it is the region where the plume moves from its supercritical to its subcritical phase. Some assert that this happens in the form of a hydraulic jump (Armi and Farmer, 1986), while others assert that it happens as momentum forces give way to buoyancy, and that the transition happens when mixing is no longer driven by the shear instabilities created by the inertial motion of the jet (Hetland, 2005). It could be that scale is important here, as hydraulic jumps have been observed in field experiments in smaller scale plumes, or some think that modelling studies done without mixing as a parameter will more likely result in a scenario where a hydraulic jump occurs, which could be mirrored in field situations with little to no wind. In any case, in the far-field, surface wind stress becomes the primary driver of mixing (Fong and Geyer, 2001). The far-field plume may be broken up into two distinct regions, the re-circulating plume and the coastal buoyancy current (Horner-Devine, 2009), both of which are mentioned below, but neither are highlighted as this region is of less interest in this study of a small scale plume.

In the absence of wind, large outflows typically form an anticyclonic eddy, or 'bulge', in the far-field, which exists at the transition between the estuarine outflow and the coastal current that forms in the direction of kelvin wave propagation (due to the Coriolis effect). It is a recirculating gyre that expands according to the ratio of the gravity current propagation speed within the estuary to the one along the coast (Chao and Boicourt,

1986) as well as ambient current conditions. Approximately 25-70% of the freshwater within is released into the coastal current via interactions with the coastal boundary (Fong and Geyer, 2002; Nof, 1988), meaning that residence time in this feature could be as long as a few days. The bulge, to the extent that one exists, is unlikely to be as persistent in smaller scale outflows, which is why in this study the focus will be on the near-field plume.

Further downstream from the bulge region is the buoyancy-driven coastal current. As water is released from the bulge, a current forms close to the coast, with propagation speeds close to the linear internal wave phase speed, and behaviour is still in line with gravity current dynamics. These alongshore currents influence coastal shelf flows and dynamics, which impacts the transport and delivery of anthropogenic materials far away from the source (Hickey and Hamilton, 1980; Blanton, 1981; Simpson and Hill, 1986; Garvine, 1991; Munchow and Garvine, 1993; Lentz and Largier, 2006), in direct contrast with the fate of smaller scale outflows.

2.6.2.1 Wind: impact on plume advection and mixing

Wind affects mixing in both near-field and far-field plumes, but is the primary driver of mixing in the far-field. Wind initiates Ekman transport which then intensifies the shear-driven instabilities between the upper layers of the water column, until the Richardson number reaches a point where mixing stops (Fong and Geyer, 2001). In the near-field, where density differences are more pronounced, the effects of wind may be more pronounced, but compete with shear driven mixing caused by momentum. In a ROMS modelling scenario with 2 turbulence closure schemes and with and without wind, overall work done by mixing is roughly equivalent between the estuary/near-field and the far-field, although in the far-field it is done over a much larger area, resulting in less work per unit area. According to the model, wind mixing had the largest effect on mixing at the transition between the near and far fields. Further ability to mix is then determined by wind stress, a critical Richardson number (Ri_C) and initial conditions. The resulting thickness of the upper mixed layer will then in turn affect the speed of Ekman transport, and therefore the propagation speed of the resulting coastal jet. In regions where the mixed layer has mixed as much as it can, there may exist areas where

mixing has "maxed out" and areas where mixing still occurs (Figure 2.8, Hetland, 2005).

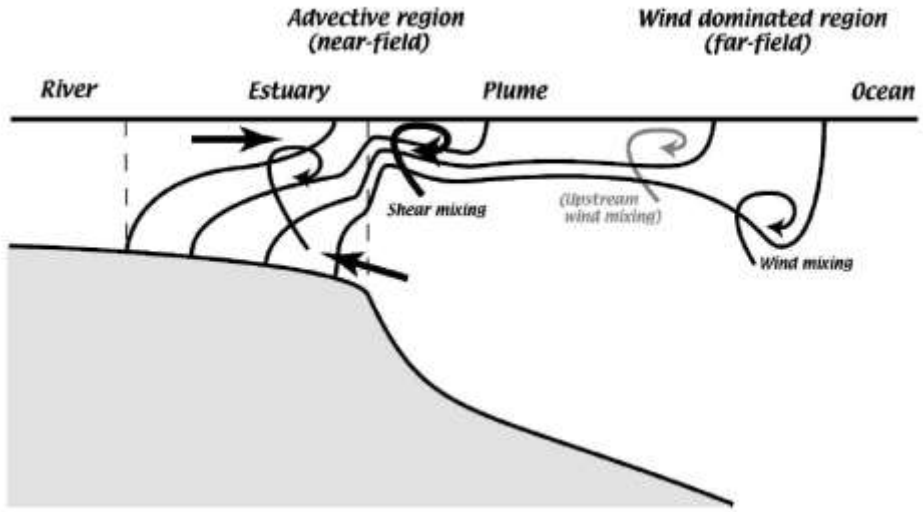

Figure 2.8: Schematic of a river plume with regions and dominant mechanisms of mixing, from Hetland, 2005.

Persistent upwelling favourable winds cause plumes to change direction, detach and move away from the coast; at first tilting isopycnals, and then eventually distorting them, causing rapid mixing, as Ekman transport drives the plume offshore in a thin layer. This mixing will eventually result in total dispersal of the plume, and dissipation of the buoyancy signature. Lighter downwelling winds will steepen the front and isopycnals and result in plume widths that are either the same as the theoretical width, W_p, or slightly smaller in the case of moderate downwelling winds. Heavier downwelling winds will encourage vertical mixing, with bulk Richardson numbers on the order of 0.25; the plume front will widen, and width will remain the same. Downwelling winds will push the coastal current up against the coast, possibly creating a strong coastal current, or jet (Chao,1988b; Fong and Geyer, 2001; Sanders and Garvine, 2001; Whitney and Garvine, 2005, Lentz and Largier 2006).

Whitney and Garvine (2005) developed two scales meant to determine wind effects on across-shelf plume structure (wind strain timescale, t_{tilt}) and along-shelf plume velocities (wind strength index, W_s). W_s is the ratio of the wind-driven velocity scale (u_{wind}) to the buoyancy-driven along-shelf current velocity scale (u_{dis}). The wind strain

timescale, t_{tilt}, is the amount of time it takes the wind stress to increase or decrease the plume width by 50%, in the case of upwelling or downwelling respectively. Using these scales in the Delaware River plume, winds greater than 10 ms^{-1} shifted the plume from a buoyancy-driven to wind-driven state, as $W_s > 1$. If these winds were upwelling favourable, the current would change direction and move offshore. For t_{tilt}, In the case of the Delaware plume, 4 ms^{-1} winds for 15 hours and 10 ms^{-1} winds for 3 hours will cause changes in the across-shelf structure (Whitney and Garvine, 2005).

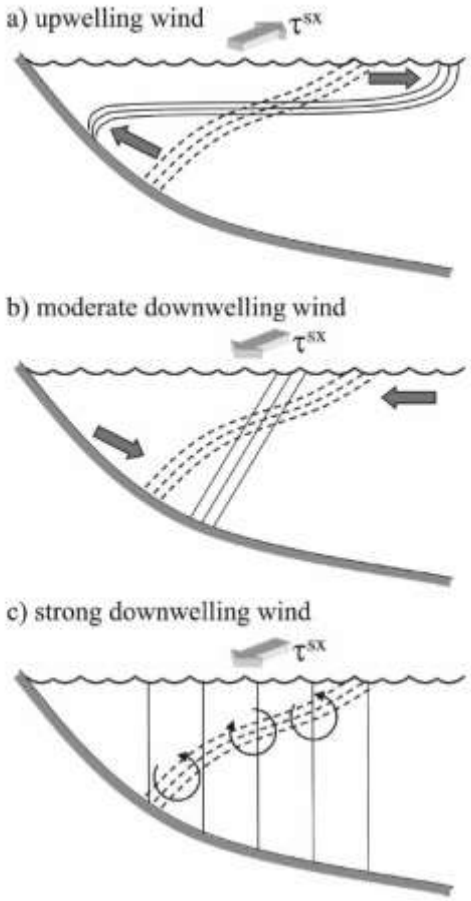

Figure 2.9: Plume diagram showing effects of alongshelf wind forcing, from Lentz and Largier, 2006.

In downwelling winds, plumes may carry fine particles as far as 60 km from the plume source, and aggregated or heavier sediments to within 1-10 km of the source. In upwelling winds, all sediment seems to settle close to the mouth (Geyer et al., 2004).

The degree to which wind contributes to overall mixing within the plume depends on the amount of wind stress produced, and could depend on the size of the plume, as smaller plumes may be more easily influenced by wind forcing, as in the case of the Chesapeake bay plume (Lentz, 2004), or even the Teign plume. In the case of a Teign plume model, winds of 20 ms^{-1} or more are predicted to rival mixing caused by buoyancy and frontal effects (Pritchard and Huntley, 2006).

Tidal energy may also contribute considerably to mixing in both the near and far fields, especially in regions of the world with larger tidal ranges (Table 2; Pritchard and Huntley, 2006).

Table 2: Values of total mixing energy integrated over the measurement period, Teignmouth, from Pritchard and Huntley, 2006

Mixing Process	Energy	Percent of Total Buoyancy Input
Buoyancy input	3.8×10^8	
Plume front	5.7×10^8	110
Tide: spring	2.6×10^7	5
Tide: neap	1.2×10^6	0.2
Wind: 1 m s^{-1}	1.0×10^5	0.02
Wind: 2.7 m s^{-1}	1.9×10^6	0.4
Wind: 5 m s^{-1}	1.2×10^7	2
Wind: 10 m s^{-1}	9.5×10^7	18
Wind: 15 m s^{-1}	3.2×10^8	62
Wind: 20 m s^{-1}	7.6×10^8	146

[a]Measurement period is HW + 2:36 hours to HW + 5:54 hours. Values are given in Joules. The total buoyancy input, over the complete ebb cycle, is estimated to be 5.2×10^8 Joules.

3 CURRENT STUDY: AIMS AND EXPERIMENTAL PROTOCOL

3.1 Introduction

Entrainment velocity, in addition to rates of turbulent kinetic energy production and salt flux, in the region just outside of the Teign Estuary are evaluated using a control volume approach from a Lagrangian perspective. The results will be compared to a similar study of the Columbia River, a large-scale river plume.

Previous studies (Luketina and Imberger, 1989 and MacDonald and Geyer, 2004) have calculated entrainment based on analysis of a control volume, using the principles of conservation of momentum, volume and/or salt. Moving with the developing plume, and integrating the changes with respect to each over the control volume surfaces that bound the plume section of interest, vertical entrainment velocity through the base of the plume is estimated.

These estimates, and others, were made at the source and leading edges, where mixing is largest. And while the former study was conducted in the small-scale outflow of the Leschenchault Estuary, most others have been performed primarily in what are

considered to be medium or large scale outflows (e.g. the Merrimack or Columbia Rivers). McCabe, et al. (2008), working in the Columbia River outflow during the RISE study (https://www.ocean.washington.edu/rise/), developed a novel technique using adjacent drifting buoys to create a control volume using conservation of volume, momentum and salt to calculate the entrainment velocity along a line midway between drifter paths. In this way, entrainment velocities, salt flux and diffusivity were estimated in the area between the source and front (or leading edge of the plume) in order to investigate the level of mixing between the two regions. In the current study, the McCabe technique was evaluated and slightly altered for use in the small-scale Teign plume, and results compared between the two plumes. Entrainment velocities found in other plumes will also be discussed briefly to add context.

Working with a smaller plume, multiple drifter deployments were possible, and provided insight into how dynamics change throughout the course of the ebb. The drifters are used in a similar way to the McCabe study to calculate entrainment (w_e), and salt flux ($S_e w_e$), all along the drifter tracks, and eddy diffusivity (K_s), at discrete points on these tracks, on multiple days and in variable conditions, but this thesis will focus on a specific day where conditions most closely match those under which the McCabe study took place. Due to the uncertainty associated with the dynamic nature of a small plume (more on this later), w_e and $S_e w_e$ are also calculated at the site of hydrographic (CTD) profiles, as a means to assess accuracy of track values for entrainment velocity. Diffusivity estimates are then compared to those calculated from microstructure data. Lastly, results from the remaining deployments (tides, wind, freshwater outflow, ambient currents) will be briefly covered in order to demonstrate the variability of mixing dynamics within this small plume. Results are intended to support the theory that small plumes disperse more quickly than large plumes, and that changes in conditions may affect that dispersal.

3.2 Site description

The Teign outflow, or plume, debouches from the Teign Estuary at Teignmouth, Devon, in the southwestern corner of England (Figure 3.1). The plume originates at the narrow

mouth of the Teign Estuary, and flows into Lyme Bay, which exists as part of the Southern English Channel.

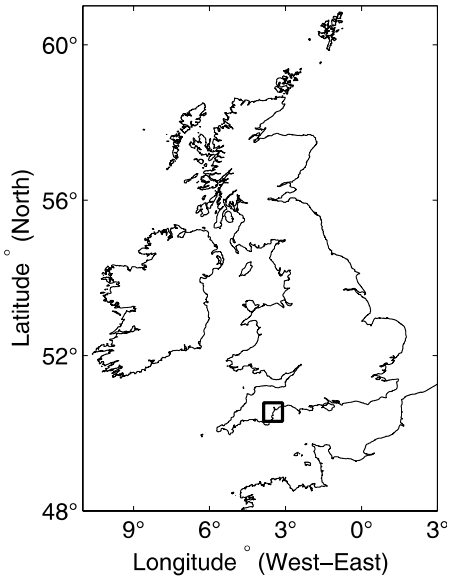

Figure 3.1: Map of the United Kingdom with the study region bounded by the black square, from Pritchard, 2000.

The River Teign is 42 km long, and originates in central Dartmoor granite moorland, at a height of 599.1 m, and flows through a catchment area of 381-526 km^2, depending on the source of the information (former from NERC Centre for Ecology and Hydrology, the latter is from Southwest Water), where it is joined by the River Bovey (the second largest tributary), the River Lemon, and the Aller Brook (Figure 3.2). It has the second largest catchment on Dartmoor. The South Teign is dammed in order to feed the Fernworthy Reservoir. About 60% of the catchment is used for agriculture, specifically the rearing of beef cattle and lamb, and other major industries including tourism, shellfish mariculture and ball clay extraction, with a Sibelco large ball clay quarry existing just upriver from Teignmouth in Kingsteignton. The Aller Brook subcatchment is the most populated. At Newton Abbot, the Teign enters a long narrow estuary, which in geological terms, is actually a submerged river valley, or ria. The estuary is approximately 6 km long and 3.7 km^2 and includes large intertidal areas. The estuary itself sustains a shipping port, shellfish farms, recreational activity and other fishing practices.

Figure 3.2: Map of the Teign catchment area (above, left), aerial view of Teign Estuary (above, right), Teign Estuary at high tide (below, left) and Teign Estuary at low tide (below, right), images courtesy of CoastView project (http://141.163.79.209/web/Teignmouth.html).

The mean river flow in the Teign between 2004 and 2013 was 5.616 m^3s^{-1}, with annual maximums of 44 m^3s^{-1} and 140 m^3s^{-1} occurring in 2011 and 2012 respectively. Average annual rainfall between 1961 and 1990 was 1230 mm per annum, with an average of 2200 mm at the highest point and 800 mm close to the estuary (Cengtre for Ecology & Hydrology, National Environmental Research Council).

The estuary is macrotidal with a semi-diurnal tidal regime. Mean tidal ranges at the estuary mouth occur between 1.7 m and 4.2 m for neap and spring tides, respectively, but can reach 6 m during some springs (Miles et al., 1997). Spring tidal current maximum velocity magnitudes are 20% larger than their neap tidal counterparts (Whitehouse et al., 2000), and flood tide is evident as far as 6.8 km upstream (Wimpol, 1989).

In Lyme Bay, tidal hydrodynamics are characterised by large tidal amplitudes and weak tidal currents. Tidal ellipses, based on data collected by Wimpol (now Fugro Geos, Ltd.) for Southwest Water in 1988 (Figure 3.3), for four sites within 4 km of Teignmouth, indicate the existence of a rectilinear tidal stream that flows towards the NE at the beginning of the ebb tide, then moves to the east, and then to the south during the latter part of the ebb (Figure 3.4). At the site closest to the estuary (RCM1) the ellipse shows greater variability about the semi-minor and semi-major axes due to the effect of the estuarine outflow on the tidal dynamics (Pritchard, 2000). Data collected from a moored RDI ADCP (inshore) and a Nortek Acoustic Wave and Current Profiler (offshore) during the current study support this trend, and a tidal ellipse constructed from the moored ADCP for the period from March 25 - April 9, 2014 is included (Figure 3.5) and shows a very similar trend to RCM1.

For a more detailed description of the estuarine tidal dynamics, see Pritchard (2000), but in brief, the estuarine outflow is governed primarily by barotropic gravity forcing, and decelerates quickly once through the mouth, at least partly due to interaction with the bar topography. It joins the ambient flow to the NE, and is increasingly pushed offshore (E) as the tidal currents change over the course of the ebb. The topography in the vicinity of the mouth becomes increasingly important as the water level decreases. Residual currents are small, though as wind increases, may become more influential. Ebb flow through the mouth does not start until 1 hour after high water, due to a phase lag caused by a tidal assymetry of 0.36 ms^{-1} in the peak flood and ebb currents, in addition to funneling and friction in the channel. This funneling also causes a sudden change from ebb to flood tide, which is clearly evident in the current tidal ellipse in Figure 3.5, and was observed in the field.

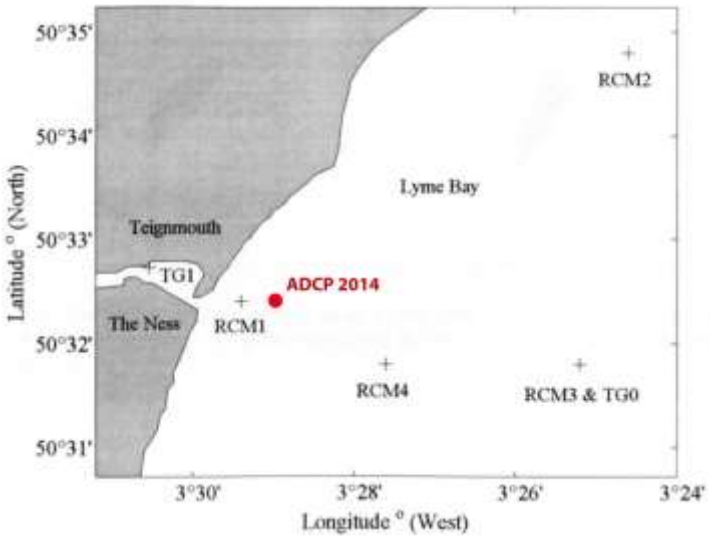

Figure 3.3: Location of moorings used to determine tidal ellipses in Lyme Bay, including the approximate location of the moored ADCP used in the current study, from Pritchard, 2000.

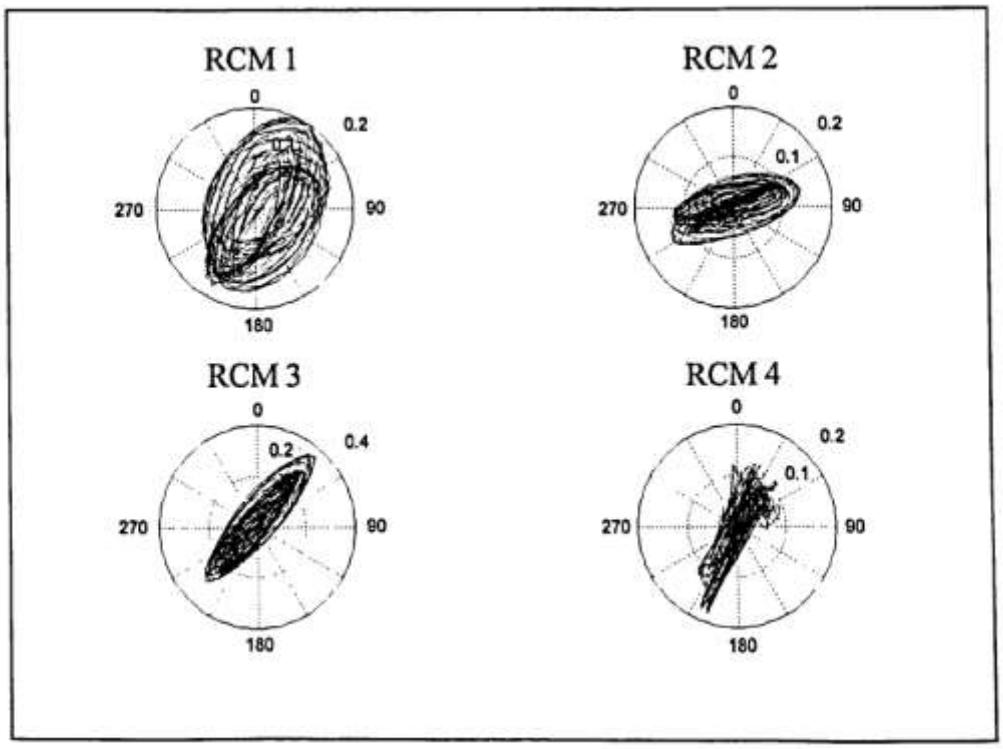

Figure 3.4: The predicted tidal current elipses, *u* (ms^{-1}) vs. *v* (ms^{-1}) from November 1 - November 30, 1998 at the sites of four RCM tidal current meters moored in Lyme Bay, from Pritchard, 2000.

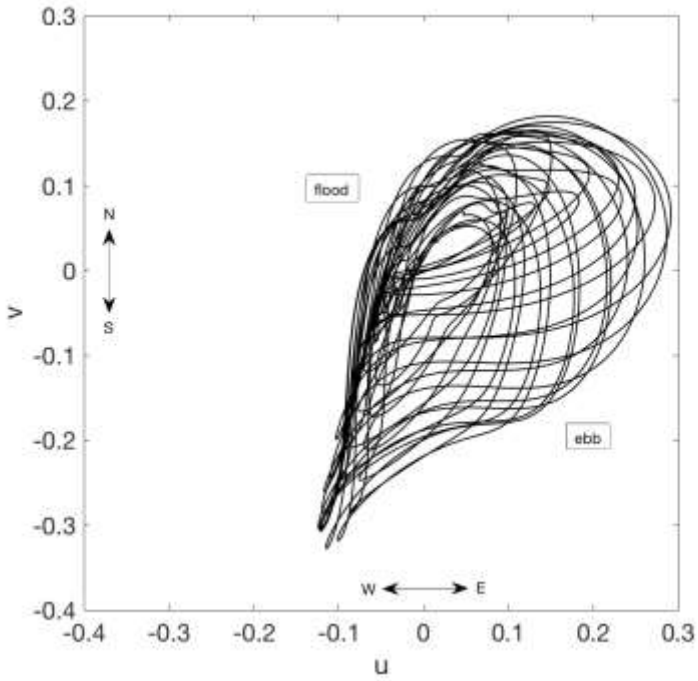

Figure 3.5: Tidal ellipse generated from moored ADCP data, March 25-April 9, 2014 (current study).

Waves are generally short period and wind-driven (including at the time of this study), and significant wave heights close to the beach occur above 0.5 m for less than 10% of the year. Winds fell within one of three principal directions in the period between 1980 and 1984: west-southwest (20.6%), northwest (22.6%), and east-northeast (20%) (VanLancker et al., 2004).

Water leaves the estuary and flows along the northern coastline of a rocky headland called the Ness and flows into Lyme Bay. At the mouth, flow is partially obstructed by a sand bar known as East Pole Sand, which is part of a system of nearshore sand bars that change in height and location over time, following a cyclical pattern (Figure 3.6). Sedimentation is thought to be induced by a combination of fair-weather and storm-dominated processes, including easterly gales (Rennie, 1838) or a combination of tides and waves (Robinson, 1975). Early documented hydrographic observations of the sand bar system were made by Spratt (1856) and then later by Craig-Smith (1970) and Robinson (1975) who monitored the patterns for 10 years (VanLancker, 2004). Frequent dredging is necessary to keep the channel open to shipping.

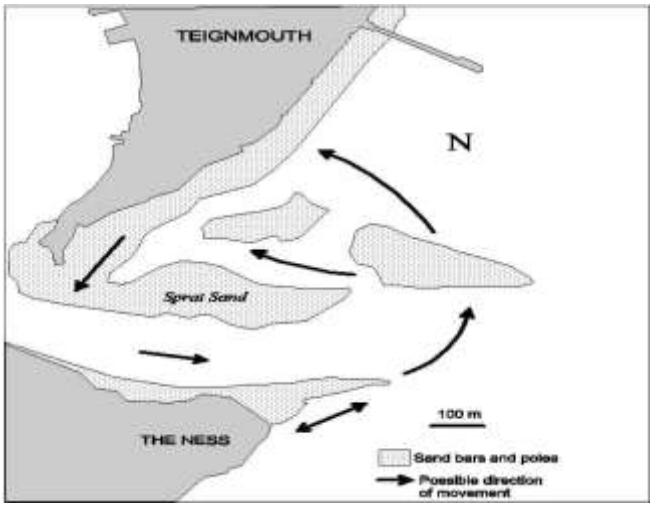

Figure 3.6: Diagram of the sediment cycle at Teignmouth, from Robinson, 1975.

3.2.1 The plume

According to previous studies (Matthews, 1997; Institute of Marine Studies/Southampton Oceanography Centre multidisciplinary study, 1995; Pritchard, 2000), the Teign plume is a small-scale, symmetrical radially-spreading outflow that is tidally modulated. The mouth of the estuary is a narrow, constricted opening, approximately 125 m wide. As mentioned, there is a large amount of sediment movement around the mouth, leading to complex bathymetry. A bar, in addition to other features, was evident (2-3 m at low tide), during the time of this study, approximately 750 m from the mouth, along the channel (Figure 3.7). It is possible that this is the location of plume lift-off, but this depends on river flow and tidal range (Horner-Devine, 2009). The plume forms on the ebb tide, and while there is some evidence of plume formation on the flood tide, it is likely remnants from the previous ebb tide (Matthews, 1997; Pritchard, 2000).

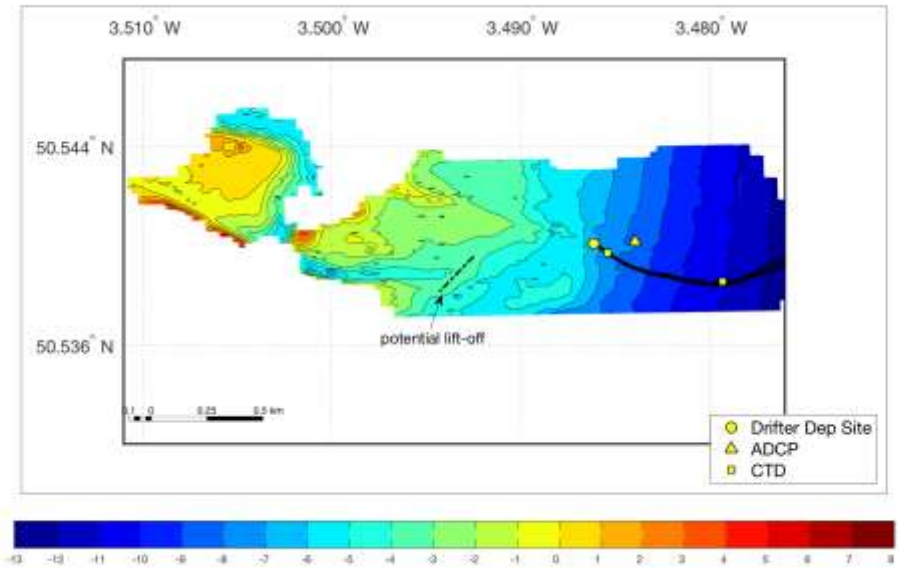

Figure 3.7: Teignmouth bathymetry, April 11, 2014, with representative instrument locations added, and potential lift-off point or location of sill adjacent to estuary mouth.

The tidal jet can reach speeds of 3 ms^{-1} at the mouth, but depth-averaged currents 1 km from there did not generally exceed 0.3 ms^{-1} in October/November 1999 (Wimpol, 1989; Walstra et al., 2000; Whitehouse, et al. 2000). During the period of our experiment, velocities at the moored ADCP did not exceed 0.32 ms^{-1}, 95% of the time, but velocities of up to 1 ms^{-1} were seen in the ADCP data and surface velocities as high as 1.4 ms^{-1} were seen in the drifter data (at peak springs). The ADCP was moored about 1.3 km from the mouth, roughly ENE, along the channel (Figure 3.7). At times of high river discharge, ebb currents can increase as much as 0.1 ms^{-1} at the surface (Wimpol, 1989). Initial plume front formation and frontal velocity is variable and dependent on tides and freshwater outflow. A front develops as densimetric Froude numbers exceed unity, a result of the higher flow velocities and narrowing of the channel at the mouth. Plume spreading is typically arrested to the south, due to the alignment of the tidal outflow with the coastal tidal stream. Wind waves and swell can constrain plume spreading as well, when moving in an opposing direction to the plume (Pritchard, 2000). Through analysis of X-band radar images collected by Southampton Oceanography Centre during an Institute of Marine Studies (Plymouth University) study in March 1995, the strongly defined front formed during the 2nd quarter of the ebb

tide, and a radial shaped plume during the 3rd and 4th quarters, which is consistent with this study's observations of a more clearly defined buoyant plume in the latter half of the ebb tide. A linear spreading rate of 0.17 ± 0.006 ms^{-1} was determined through analysis of the X-band radar images (Pritchard and Huntley, 2006)

Pritchard (2000) found that Garvine's classification based on the Kelvin number ($K \equiv \frac{\gamma L}{\frac{c}{f}}$) does not apply to the Teign plume. Based on his calculations, this plume has a Kelvin number of 2.5, which suggests an appreciable influence from Coriolis forces. This does depend, however, on what is used as the characteristic length scale, *L*. (See Section 5.2.1). It is evident from his examination of the momentum balance that the barotropic pressure gradient, due to large tidal ranges and the slope driven pressure gradient between the estuary interior/exterior, clearly dominates the balance of forces that drive the plume. The radial spreading described above, as seen in the X-band radar images, is a feature of K-small (K<<1) plumes, as there is no deformation caused by the Coriolis affect beyond the Rossby radius of deformation, which is 2 km, as determined by Pritchard 2000 and the current study. In the current study, the Kelvin number differed, but was also calculated differently. This will be explained in Section (5.2.1).

Pritchard and Huntley (2006) developed a model for predicting the formation of the Teign plume, demonstrating that, depending on the ratio of buoyancy input to mixing, a plume may not form under certain conditions, namely, during spring tides with freshwater flow rates of less than 7.5 m^3s^{-1}. Those results show that the plume may only form during 1 out of every 3 spring tides, but should always form during neaps. In the case of the current study, two-layer flow may be referred to as a plume, but in some instances, may identify more closely with a buoyant jet, or even a jet, where momentum may exceed buoyancy, but the critical factor here is that two-layer density-driven flow is still evident. In addition, freshwater flows in the current study are taken as a combination of the flows from the two biggest tributaries, the Rivers Teign and Bovey, that feed into the Teign Estuary. There are additional freshwater inputs, and mixing within the estuary is not taken into account, so these numbers are rudimentary (and conservative) in terms of actual buoyancy flux into the plume. In the case of our experiment on April 3, which is the focus of this study, the tide is 3 days past peak springs, freshwater flow rates total 7.2 m^3s^{-1}, and two-layer density-driven flow is evident.

3.3 Methods

In an effort to expand on the current body of knowledge regarding the Teign plume and other small, or 'micro', plumes like it, this study will compare the level of mixing that occurs in this small plume with other plumes, small, medium and large. Specifically, the Teign plume will be compared to the Columbia River plume using a control volume approach developed by McCabe et al. (2008) to estimate variables that represent mixing. Pairs of drifting buoys (drifters) are used to define the boundaries of the control volume, so that the continuity equations for volume, salt, and momentum may be used to estimate entrainment, salt flux, and diffusivity, using temperature as a proxy for salinity in the case of the Teign. First, a brief description of the study site from that experiment, followed by a brief description of the deployment and the theory behind the control volume analysis. After, the current study will be introduced. First there will be a description of the deployment, then the application of the control volume to the Teign plume, including some experimental differences, and finally, a description of the instrumentation used and the steps taken to process the data..

3.3.1 The Columbia River study

3.3.1.1 Deployment

The entrainment calculations were based on a drifter experiment conducted during the RISE study (https://www.ocean.washington.edu/rise/) on 9 June 2005, and this study was inspired by the control volume technique developed by MacDonald and Geyer [2004] and Chen and MacDonald [2006] in the Merrimack River plume, near the Massachusetts/New Hamphire border in the United States. A single group of satellite-tracked drifting buoys were deployed in a straight line across the river mouth at maximum ebb, on the greater ebb of the day, and were left to run their course through the remainder of the ebb tide (Figure 3.8). CTD casts were taken at the centremost drifters, 5 times throughout the deployment, to allow for estimates of entrainment terms, salt flux and diffusivity. There existed a 30 minute lag between ship arrival time at the

pack of drifters and the CTD casts. Drifters were of the "Davis" configuration (Davis, 1985), with sails 1m deep by 0.5 m wide. Moored and vessel-mounted ADCP data were available for use in the evaluation of the steady-state assumption, and a comparison to diffusivity measurements calculated from microstructure measurements collected during another cruise.

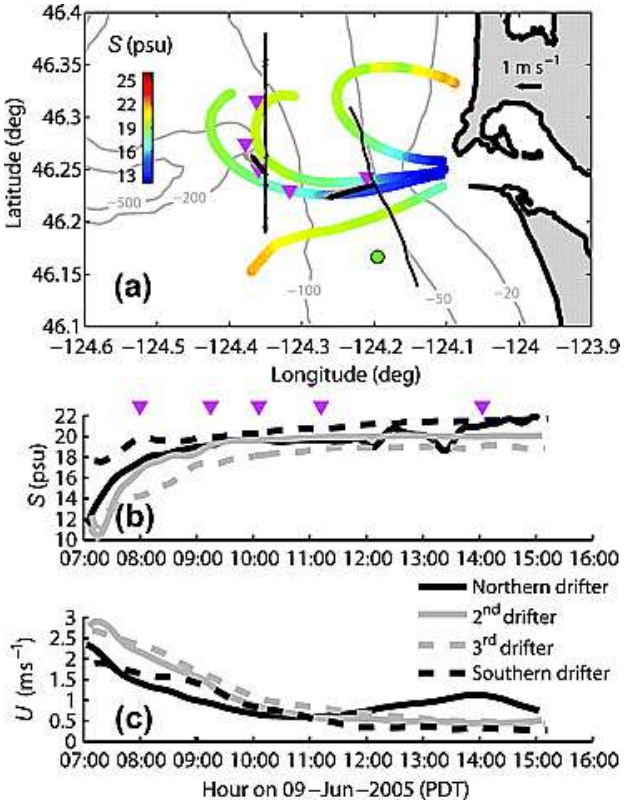

Figure 3.8: Drifter tracks overlaid with salinity deployed at the mouth of the Columbia River on June 9, 2005, from McCabe et al., 2008. Ship tracks are denoted as black lines in the top panel, and the magenta triangles represent sites of hydrographic profiles. Profiles are plotted at the time the ship arrived on station, cast times were <30 minutes later. The green dot is the location of the ADCP used in the steady state analysis. The small vectors plotted midway along the drifter tracks represent mean velocities calculated from the (gray) drifters and (black) shallowest shipboard ADCP bin.

3.3.1.2 Drifter control volume analysis

Following is a description of the theory behind the control volume analysis. For a more detailed description of the methodology that is used here, please refer to McCabe, et al. (2008 and 2009).

Assuming a steady, incompressible flow, the control volume is defined by pairs of adjacent and diverging drifters, and is analysed using the continuity equation for volume in a streamwise coordinate system (Figure 3.9):

$$\nabla \cdot \mathbf{u} = 0 \qquad (14)$$

Where, $\mathbf{u}$ = *(u,v,w)* is the three-dimensional velocity vector with components in the streamwise, cross-stream and vertical (*x,y,z*) directions, respectively, and $\nabla = (\frac{\partial}{\partial x}, \frac{\partial}{\partial y}, \frac{\partial}{\partial z})$ is the three-dimensional gradient operator. The typical *x, y* coordinate system is rotated so that the principal flow direction is aligned with the instantaneous velocity vector, though *x*, *y* and *z* are used here to avoid confusion with variables for salinity, etc. A streamwise coordinate system is used to better visualise and more easily interpret the plume dynamics (Hence and Leuttich, 2003).

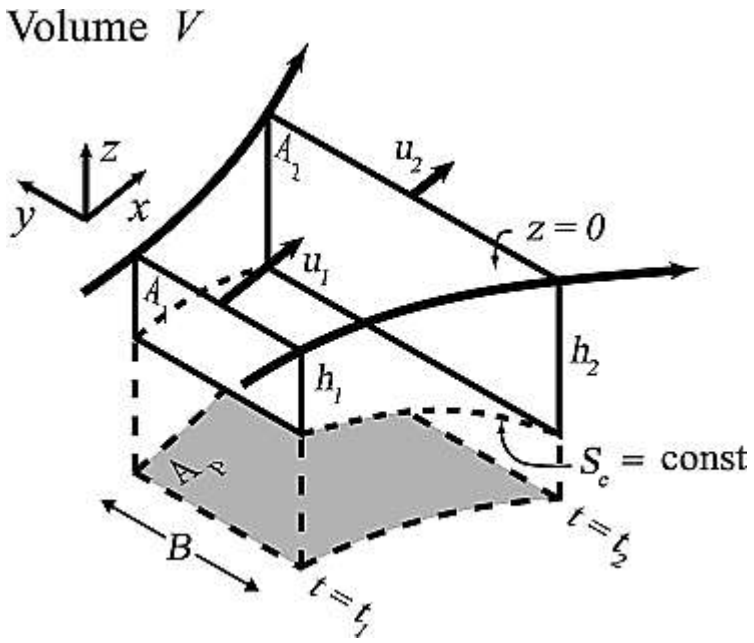

Figure 3.9: Schematic of the control volume used for entrainment calculations, based on drifter movement and divergence, from McCabe et al., 2008.

Integrating over the volume in Figure 3.9, and using the Gauss divergence theorem to break up the equation into surface integrals over an areas A, A_1, A_2, and A_{bot} gives:

$$\int_{A_1} \mathbf{u} \cdot \hat{\mathbf{n}} dA + \int_{A_2} \mathbf{u} \cdot \hat{\mathbf{n}} dA + \int_{A_{bot}} \mathbf{u} \cdot \hat{\mathbf{n}} dA = 0 \qquad (15)$$

There is no integral over the top surface, as $\mathbf{u} \cdot \hat{\mathbf{n}} = 0$ there, similar to the side terms, as the drifters are horizontally Lagrangian and the assumption is made that spreading is uniform with depth, which will most likely result in an overestimate of plume spreading, as plumes are typically sheared with depth. This analysis assumes lateral entrainment is zero, as Macdonald and Geyer (2004) found them to be negligible in the upper layers (< 5-6 m) due to the alignment of the streamwise direction with the mean upper layer flow direction. After integrating over the surfaces of the control volume, then redefining each of the terms based on the velocities at each surface (A_1, A_2, and A_{bot}, which becomes A_p), with the velocity through A_p defined as $\mathbf{u} \cdot \hat{\mathbf{n}} = -w_e\left(\zeta_x^2 + \zeta_y^2 + 1\right)^{-1/2}$, and $dA = dxdy\left(\zeta_x^2 + \zeta_y^2 + 1\right)^{1/2}$ at the bottom boundary, and ζ_x and ζ_y are the x and y slopes of the plume base, respectively, then allowing dx —> 0 as it is 0 by assumption, gives:

$$\frac{\partial}{\partial x}\int_{A_{sect}} u \; dzdy - \int_{y1}^{y2} w_e dy = 0 \tag{16}$$

A_{sect} represents a cross-sectional area of the rectangle between adjacent drifters that is normal to the local streamwise direction (e.g. A_1 or A_2). Finally, performing the integrals and solving for the vertical entrainment velocity, produces:

$$w_e = \frac{1}{B}\frac{\partial}{\partial x}(uhB) \tag{17}$$

Where the width of the section (distance between drifters) is B and the mean plume depth across the section is h; u and w_e are the streamwise flow velocity and entrainment velocity, respectively. They are sectional averages, and presented along 'midpoint' tracks. Similarly, an equation for the salt flux is produced (using conservation of salt):

$$S_e w_e = \frac{1}{B}\frac{\partial}{\partial x}(uhBS) \tag{18}$$

Where S_e is the entrained salinity and S represents plume salinity. In McCabe's case, the plume depth was defined as 'just beneath the overlying turbulent plume so that any vertical flux through the plume base could be described entirely by vertical advection'. They chose a particular isohaline, or 26 psu. Full-depth plume salinity and velocity were taken as the drifter-measured salinity and velocity. This could result in an overestimate of entrainment and vertical salt flux, with plume velocity and salinity anomalies potentially off by a factor of 2, as typically a plume is sheared and stratified, and bulk properties are approximately half that at the surface. It is assumed that actual salt flux estimates (Equation 21) will be more accurate as velocity decreases and salinity increases with depth.

The previous two equations may be combined by solving for and then eliminating w_e, and once h is determined at the sites of the hydrographic profiles, the following equation may be used to find the unknown constant of integration, at that site:

$$uhB\Delta S = const \tag{19}$$

where $\Delta S = S_e - S$, and is the local salinity anomaly. Once the constant is known, the same equation may be used to calculate h along the entire drifter path. All data are mean values at midpoints between drifter tracks. With h, w_e may then be calculated as follows:

$$w_e = \frac{hu}{\Delta S}\frac{\partial S}{\partial x} \tag{20}$$

Either equation (17) or equation (20) may be used to calculate entrainment. In both studies, the latter was used. Equation (20) may then be expanded into its component terms to be used as a diagnostic tool, or to provide further information about the flow (see Section 4.3.4.2).

Due to the base of the plume being defined as the layer just underlying the turbulent plume, so that all vertical flux may be explained by vertical advection, it holds that vertical salt flux may be expressed as a product of the turbulent diffusivity of salt and local stratification:

$$S_e w_e = -K_s \frac{\partial S}{\partial z} \tag{21}$$

CTD profiles allow for the determination of $\partial S/\partial z$, and therefore estimates of K_s. McCabe at al. (2008) meant these to be rough estimates. In that study, the values compared well (same order of magnitude) to microstructure data collected 10 km west of the Columbia River mouth, but shoreward of the front. In the case of the current study, similar estimates of diffusivity data were also compared to microstructure data.

3.3.1.3 The steady-state assumption

To evaluate the steady state assumption, McCabe et al. calculated the total Lagrangian acceleration (DU/Dt) from the drifter data, and then endeavoured to differentiate the Eulerian, or the local acceleration, ($\partial U/\partial t$), from the Langrangian component, the advective acceleration ($U\,\partial U/\partial x$), based on the relationship:

$$\frac{DU}{Dt} = \frac{\partial u}{\partial t} + \left(U\frac{\partial U}{\partial x}\right) \tag{22}$$

Then, a theoretical $U\,\partial U/\partial x$ was determined by plotting drifter velocity against along-track distance, taking the slope of that line, and multiplying it by the drifter velocity. In order to validate this and compare it to $\partial U/\partial t$, single point estimates were made for both. First, $U\,\partial U/\partial x$ was calculated by differencing simultaneously measured velocity data from the drifters and the vessel-mounted ADCP at various points along the drifter tracks (Figure 3.8). Then, $\partial U/\partial t$, or the change in velocity at a single point with respect to time only, was calculated by differencing velocities from the drifters and the vessel-mounted ADCP at locations where the ship crossed the drifter tracks. Estimates were also made using the moored ADCP data. Ideally, $\partial U/\partial t$ is zero in a steady flow, but in their case less than 25% as compared to $U\,\partial U/\partial x$ was considered 'relatively small' and more than half, relative to $U\,\partial U/\partial x$, invalidated the steady state assumption.

3.3.2 The Teign study

In the case of the Teign plume, four drifters, equipped with high-resolution thermistors, rather than conductivity sensors, were deployed approximately 1.5 hours after high water, before maximum ebb, just outside of the Teign Estuary. The deployment site was located approximately 200 m west of the moored ADCP. Drifters were released in a single cluster, just beyond the last channel marker (Figure 3.7), so as to keep out of the way of the dredger that works every day in the vicinity of East Pole Sand. Releasing them in a cluster was intended to provide insight into the spreading of the plume, and was practical as they were not released in the estuary mouth, and it was difficult to know where the jet boundaries were located. The drifters were released and allowed to go as far as ~1.8-2 km from the mouth, as the plume has been described as having a

typical diameter of about 2 km (Pritchard and Huntley, 2006). This allowed for approximately 11-13 deployments, starting at 1-2 hours after high water, and continuing for the entire ebb tide. Drifters were deployed in staggered groups, so, about 30 minutes after one group was deployed, a second group was deployed, so that two groups would be in the water simultaneously until the first group was pulled about 45 minutes after initial deployment. This approach differed from the McCabe et al. study as they only worked with one drifter deployment in a single day. Our drifters were then recovered and redeployed in the original position, the goal being that simultaneously deployed groups could be used to calculate the total Lagrangian acceleration and the relative contribution from local and advective acceleration, in order to address the steady state assumption. Due to the staggered way in which the drifters were deployed, the deployments follow a naming convention that reflects this: D1(1), D1(2), D2(1), D2(2) and so forth.

In our case, there was no lag between arrival on station and the CTD casts. This was particularly important for us, considering the difference in scale and the speed at which conditions could change, as well as how quickly the drifters could reach the front.

Drifters could not be deployed in the mouth itself, as the dredger operated most days during the experiment, in the mouth of the estuary. This did not adversely affect the experiment, as the lift-off point was likely not too far from the actual deployment site (Figure 3.7), meaning that only source conditions were missed, which was an advantage in this case.

Drifters were deployed on multiple days, but this thesis will focus on one day in particular, April 3, with a brief description of the range of values found overall.

3.3.2.1 Application of drifter control volume analysis to the Teign plume

Due to the smaller size of the Teign plume, and the degree to which it responds to external forces, modifications were made to the McCabe procedure for the current study. Its small physical size, imposed by geological limitations and decreased buoyancy input, results in weaker density gradients, and an increased rate of mixing with ambient seawater, especially at times of reduced buoyancy input (Pritchard and Huntley, 2006). The Pritchard-Huntley model does not take wind into account, and it

was evident during this experiment that wind only increases this instability. Freshwater flow only exceeded 7.5 m^3s^{-1} twice during this experiment, and wind, from various directions, was a factor for most deployments. Wind and buoyancy input both presented challenges in the current study, as both rendered the plume less predictable. Though, despite the threat of instability, two-layer supercritical flow and a frontal feature were evident throughout the experiment.

In the sections that follow is a description of how the analysis was customised to the Teign plume; first, a description of the instrumentation used in this study, followed by a look at how to determine which data may be used for this type of analysis for a more ephemeral plume of this size, and finally the steps that correspond to the steps taken by McCabe et al. (2008) (see Section 3.3.1), and how those may have been altered slightly for this study. All in all, one major diagnostic when working through the analysis was the effect that any changes would have on the modelled plume thickness (h). In the end, a realistic h was the ultimate goal. Ideally, h would be thicker at the source, thinner as the plume spreads, and appropriately deep when compared to relevant CTD casts. Any spikes suggested anomolous conditions.

3.3.2.2 Instrumentation and data processing

3.3.2.2.1 Drifters

Instrumentation

Lagrangian measurements were made using 6-8 floating buoys, or drifters, with standard handheld, EGNOS-enabled Garmin 76S or etrex GPS devices attached to the mast (Figure 3.10). The Teign drifters had a smaller footprint than the Columbia drifters, at about 0.5m deep by 0.25m wide (submerged section). Temperature was used as the primary (measured) tracer for entrainment and salt flux, as salinity data was unavailable. Drifters were deployed with a Seabird 56 thermistor attached to the base of the unit, and the sensors recorded temperature ~0.3 m below the surface, which was appropriate in our case, as the shear layer very often began at 1m, and very often

shallower than that. The sensors have an accuracy of 0.005°C, which is adequate as plume and ambient temperatures differed by >0.08°C during our experiment. Drifter position was recorded every 5 seconds and thermistors sampled at 1 Hz.

Garmin GPS 76 and etrex units were used with EGNOS corrections enabled, allowing for accuracy to 1-3m, a potential error deemed acceptable when studying a plume >2 km in size, and where very fine-scale movement was not a feature in question.

Figure 3.10: An image of the drifters used in the Teign experiment (photo credit: Lloyd Russell, Plymouth University).

Data Processing

The approach to data processing for this study also differs somewhat to that employed by McCabe et al. (2008). In that experiment, along-track speed and salinity data are filtered for high-frequency noise by fitting the data with exponential curves in time, and drifter pair distances are fit to linear functions of time, both at least in part due to high frequency oscillations thought to be due to the presence of internal waves. It was thought that these oscillations would be enhanced when taking derivatives, as in equation (17). illustrates the difference between the Columbia River data produced by

the exponential fit and the raw velocity data. For velocity, salinity and drifter spread, data 'tails' that do not fit the linear function are not included in the entrainment calculations, as it was determined that the drifter is close to the front, and frontal dynamics are not the focus of that study.

In the current study, data are also filtered for high-frequency variability, but by using a cubic smoothing spline with a high noise tolerance. In other words, on a scale from 0-1, with 0 being the least-squares straight line to fit the data, and 1 being the variational, or 'natural' cubic spline interpolant, a value of 0.99999999 was used. The spline was used as a way to both filter the velocity data and interpolate a new (common) time axis for the drifter position and temperature data, as the raw temperature data was recorded at a 1 second sampling interval versus the 5-second position data. This filter describes the trends in the velocity more accurately than an exponential fit, while still smoothing to a point where bumps in the data would not disturb modelled plume thickness, as was found in McCabe et al. (2008). Filtering also served to remove spurious velocity data caused by positional errors.

Neither velocity nor drifter distance requires additional fitting, as we did not see the same oscillations (due to internal waves) that were seen in the Columbia River plume. In cases where disturbances were present, there was typically a reason (e.g. proximity to a front), and indicated that those data should not be used in the entrainment calculations.

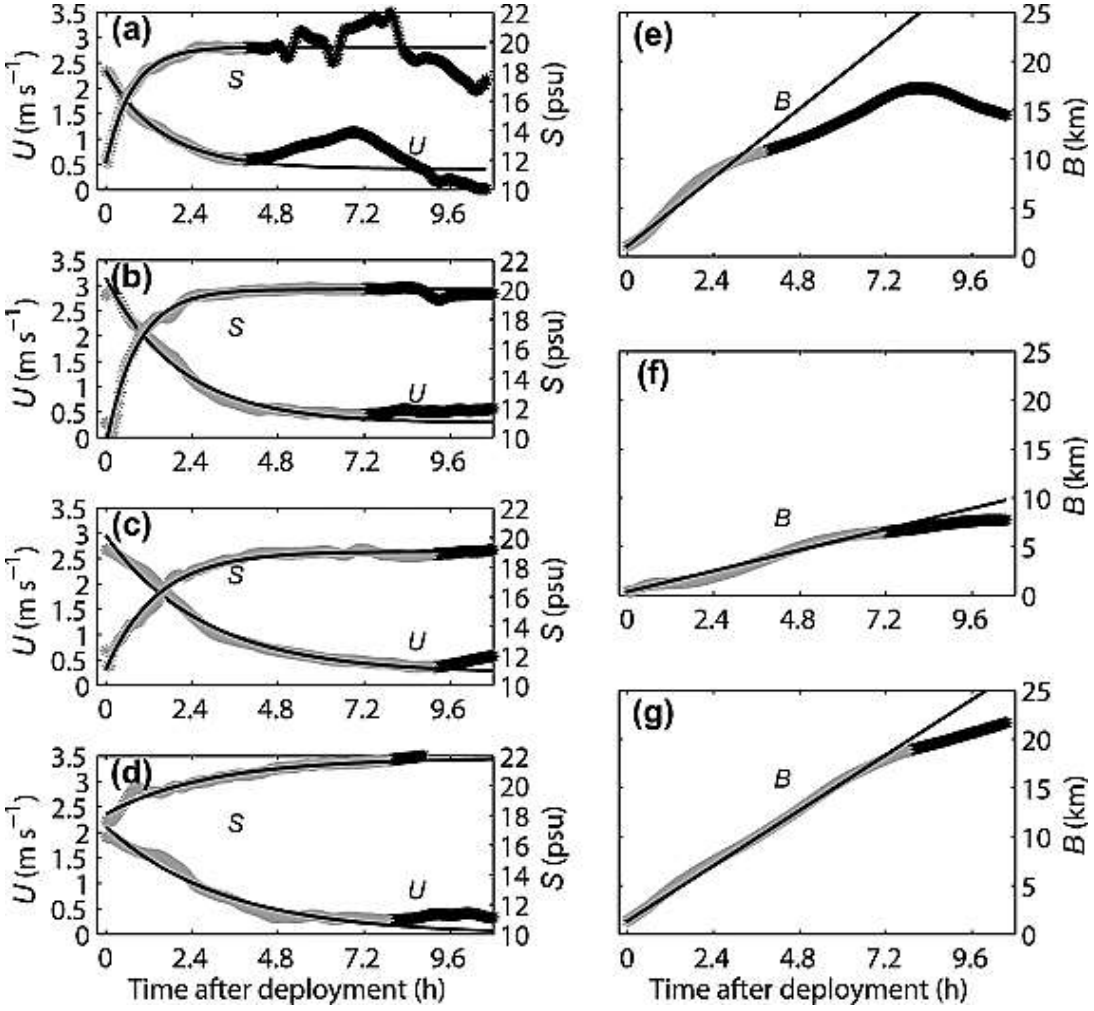

Figure 3.11: Raw (thick line) and fit (thin lines) salinity, velocity (a-d), and drifter spread (e-g). Black tails were eliminated from the fits, due to likely exposure to frontal dynamics.

Drifter velocities were compared to surface ADCP velocities, and the results shown in . The difference between the two sets of velocity measurements appears significant, but is likely due to the fact that 10% of the water column was removed from the ADCP data, due to contamination from side lobe interference at the surface boundary. First, plumes are vertically sheared, and velocities decrease with distance from the surface, and so this would result in a difference between the surface layers of the plume and the uppermost data measured by the ADCP.

Looking at Figure 3.12, the drifters do not appear to be subject to wind slippage, as the differences hold steady even on days with less wind. In addition, the track sections that

are used for the entrainment calculations are not longer than 15-20 minutes, in most cases. This would be too short a timescale during which to accumulate errors due to wind slippage, which would most likely be very small. As far as the influence of the wind on the surface currents, and thus on the drifters, this effect is relevant to this study. This plume is typically 1-3m deep, and wind does affect its behaviour. This is well-documented and was obvious during the field campaign.

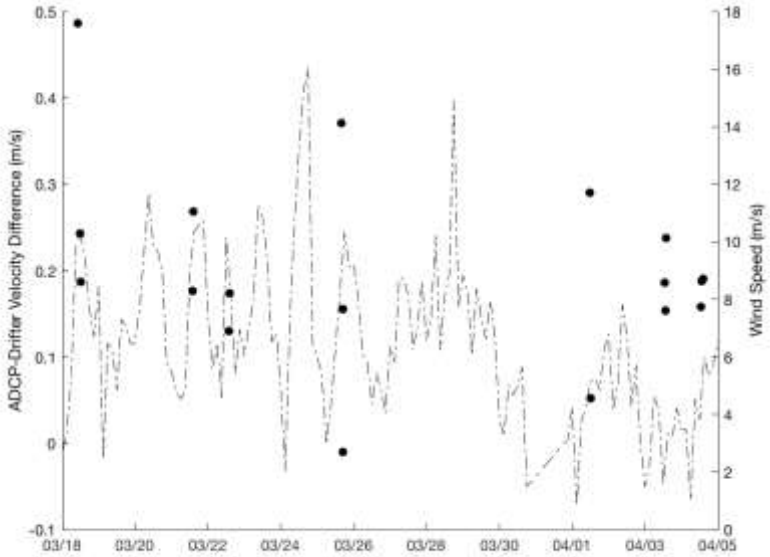

Figure 3.12: Comparison between wind speed (dashed grey) and the difference between drifter and ADCP velocity (dots) from 0.5 and 1 m, respectively.

3.3.2.2.2 Hydrographic profiles

Instrumentation

Conductivity, temperature and depth (CTD) casts were performed using a Seabird Electronics 19+ V2, every 15 minutes at the centre of the drifter cluster, or if groups of drifters diverged significantly (more than approximately 50 m) additional casts would be taken at each group, so that full water column profiles could be captured, and conductivity changes related to temperature changes. The SBE 19+ V2 has a

conductivity sensor with an accuracy of 0.0005 S/m and a typical resolution of 0.0005 S/m, and a temperature sensor with an accuracy of 0.005°C and 0.0001°C resolution. The CTD profiled at 4 Hz, averaging 1 measurement per sample. Measurement stability is 0.0003 S/m for conductivity, and 0.0002°C for temperature, per month.

Data processing

CTD casts were low-pass filtered, and the temperature and conductivity time constants aligned. Temperature and salinity data were then physically aligned with pressure data. The surface soak was manually removed, due to the need for accuracy in preserving as much data at the surface as possible.

3.3.2.2.3 Currents

Instrumentation

An RD Instruments 1200 kHz acoustic Doppler current profiler (ADCP) was deployed 1.4 km from the mouth (Figure 3.7), in 5 m of water at lowest astronomical tide (LAT). Drifter tracks commonly traversed the area just adjacent to, or over the ADCP. The ADCP sampled in Mode 12, or a high resolution sampling mode, with 0.5 m bins, a ping interval of 1 second, a sub-ping interval of 0.06 seconds, and 5 sub-pings for every ping, for 28 days. A Nortek Acoustic Wave and Current profiler (AWAC) was deployed outside of the area of direct plume influence, 3.8 km and 145 degrees (SSE) from the estuary mouth, in 12.6 m (LAT) of water, sampling ambient coastal currents. It collected data in 0.5 m bins, and calculated 1 minute averages of current velocity and direction every 5 minutes, and sampled waves every hour, for the same period.

Both the ADCP and AWAC were equipped with an INW PT2X. This pressure and temperature sensor has an accuracy of +/- 0.05% FSO (full scale output) and 0.5°C, and a resolution of 0.0034% of full scale and 0.1°C, respectively. These sensors sampled every 5 minutes.

Data Processing

ADCP and AWAC current data underwent minimal processing. Surface data was trimmed, using echo amplitude as an indicator of surface location, and then 10% of the water depth was eliminated due to possible side-lobe reflection. The high resolution ADCP data were block-averaged into 2 minute periods, and the AWAC data was not averaged as it was already collected as 10 minute averages.

ADCP velocities were separated into tidal and residual components using the harmonic analysis and reconstruction functions from the UTide Matlab function (see Unified Tidal Analysis and Prediction Using the "UTide" Matlab Functions, Codiga, 2011). Briefly, results of the tidal analysis are as follows: principal tidal constituents from the analysis of the pressure signal were M2, S2, N2, M4, MS4, and O1; accounting for 99.2% of the 98.2% of the pressure data signal that was tidal. On the other hand, 70% of the velocity data signal is tidal, with the remaining 30% likely attributed to other phenomena (i.e. the passage of fronts). The principal constituents for velocity are M2, MSF, S2, M4, MS4 and OO1, accounting for 93% of the tidal signal.

Temperature data from the INW sensors were smoothed using a running mean with a 20 point window, which was abritrarily chosen based on the appearance of the curve.

3.3.2.2.4 Microstructure profiler

Instrumentation

Microstructure measurements were collected using the MSS 90 microstructure probe from Sea and Sun Marine Tech. With 16 bit resolution the profiler measures microstructure and turbulence (temperature, conductivity and microscale current shear from velocity). The profiler sampled in rising mode. It was attached to the seafloor, allowed to float to the surface, and then pulled back down again by hand, using a moored guide pulley. Profiles were collected almost continuously from about 1.5 hours

after high water until 4 hours after high water, adjacent to the moored ADCP. Care was taken to sample far enough from the ADCP so as not to contaminate those data.

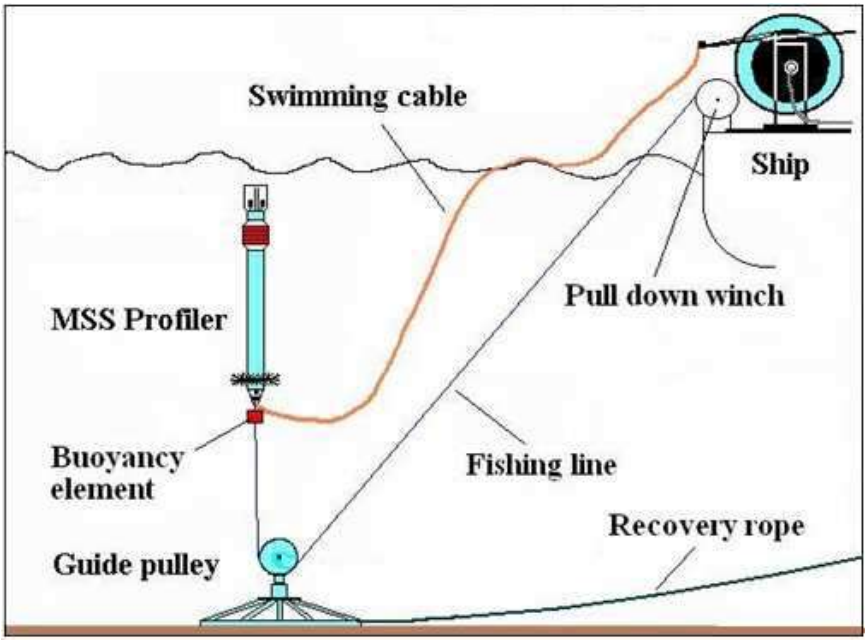

Figure 3.13: Diagram of MSS set up when sampling in rising mode

Data processing

Microstructure data (pressure, temperature, shear, acceleration, conductivity) were initially checked for outliers, and smoothed with a moving average. Physical shear was calculated from time, pressure and data from the raw shear sensor, and then detrended and low-pass filtered using a Butterworth filter. After this, the temperature response time was corrected, and turbulent kinetic energy (TKE) dissipation $\boldsymbol{\varepsilon}$ was calculated using the equation for isotropic turbulence:

$$\varepsilon = 7.5\nu \left\langle \left(\frac{\partial u}{\partial z}\right)^2 \right\rangle \qquad (23)$$

where $\partial u/\partial z$ is the velocity shear, and ν is the kinematic viscosity of seawater, and the variance is calculated using an iterative fit to the Nasmyth spectrum (Nasmyth, 1970; Dewey, 1987; Baumert, 2005). The data was averaged over 1m bins. The Brünt Vaisala Frequency was calculated, followed by the eddy diffusivity $K_\rho = 0.2(\varepsilon/N^2)$, where 0.2 is

the mixing efficiency and N^2 is the Brunt-Vaisala frequency, and the Ozmidov Scales (see Section 2.5.1).

3.3.2.2.5 Meteorological data

Meteorological data were obtained from a coastal weather station in Holcombe (Sean Seabrook, dawlishweather.co.uk), which is approximately 2 miles north of Teignmouth, along the coast. Technical difficulties resulted in data gaps at this station. These were filled by modelled wind data, generated by the Weather Research and Forecasting (WRF) Model (courtesy of the National Center for Atmospheric Research, or NCAR). Data were minimally processed: either block averaged (in the case of Figure 4.2 – 4.5) or smoothed using a running mean.

Freshwater influx into the estuary was taken as a combination of the river flows from the River Teign and the River Bovey, as measured at the Environment Agency river flow gauges located at Chudleigh Bridge and Bovey Parke, roughly 12 km upstream from the Teign Estuary.

3.3.2.2.6 Bathymetry

Instrumentation

A bathymetric survey was completed to map the current state of the complex bathymetry in order to understand its influence on the plume's behaviour at the time of this study. Topographic surveys were performed on Spratt Sand (tidal flat at the mouth of the estuary) and the Salty (tidal flat inside the estuary) using a Trimble 5800 RTK-GPS system. The bathymetric survey was performed using a Midas Surveyor, with an integral 210 kHz echosounder and input from a Trimble 5800 RTK-GPS system. An INW PT2X temperature and pressure sensor was also deployed at the base of the Fish Quay, which is located approximately 0.55 km upstream from the mouth, along the channel, in order to record temperature inside the estuary.

Data processing

Bathymetric data was converted to OSGB36 (Eastings and Northings). Depths were calculated as the difference between the total distance between the GPS antenna and the seafloor and the distance between the antenna and the echosounder. Erroneous data (e.g. out of water periods) were manually removed, and then de-spiked by removing data that were greater than 3 standard deviations from the mean. Data was then plotted using a quadratic Loess interpolator (Plant, et al., 2008), which uses a user-defined smoothing parameter that is 4 times the sample spacing of the data, effectively removing features shorter than twice the smoothing scale. The base station for both topographic and bathymetric surveys was set up at the end of the Teignmouth carpark, just adjacent to the mouth of the estuary. It was located over, and data was referenced to, an Environment Agency Benchmark (EABM 293885.93, 72377.4,5.264).

3.3.2.3 What qualifies a deployment for this analysis?

First, an adequate temperature difference between plume and ambient, as well as a straightforward relationship between temperature and salinity is key. In the latter case, the temperature profile should roughly follow that of the salinity/density profile, as density is the main driver in the dynamics of a two-layer density-driven flow. Next, the presence of easily identifiable two-layer flow is necessary, and lastly, there needs to be adequate plume available to measure after lift-off and before the drifters cross the front, as the mixing due to bottom stress and frontal dynamics are not of primary interest in the current study.

In the case of this plume, early deployments were typically excluded, as the density and temperature differences were small, and the plume itself was small. Both meant that there was very little to work with as the plume would mix quickly, no coherent two-layer structure was evident, and the drifters would cross the front very early on. In the field, drifters were observed lining up along a visible front. The data appears to support this, as temperatures steadily decrease, and then increase for a time, and then decrease

again- it seems that they approach what could be a front, pause (indicated by the increases in temperature) and then presumably break through as the front weakens.

3.3.2.3.1 Using temperature as a plume tracer instead of salinity

One major difference between the two studies is the use of temperature as a passive tracer for plume water, as opposed to salinity. In the instances where temperature is used, it will be used in place of salinity when calculating entrainment, as changes in temperature will indicate that entrainment has occurred, just as changes in salinity would be otherwise.

The biggest issue facing this choice is whether the temperature difference between estuary water and ambient ocean water is enough to produce a temperature differential between the resulting plume and underlying ambient water that would allow us to differentiate the two when calculating the entrainment velocity. Pritchard (2000) analysed seasonal river temperatures from 1995 and 1996 and compared to mean SST from 1957-1989 and used those differences (~2°C in October) as justification for using temperature as a tracer for Teign plume water (Figure 3.14). In that case, there was generally a 0.2-0.4°C temperature difference between plume and ambient. During the current study, the degree to which the temperature between the estuary and the ocean differed depended on the day. The largest temperature difference existed on April 4, with a ~2°C between the AWAC site (at depth) and the temperature sensor located at the base of the Fish Quay, inside the estuary, by the end of the ebb tide. The smallest difference occurred on March 22, with a difference of ~0.5°C by the end of the ebb. A more detailed comparison, in addition to how this corresponded to the difference between the plume and ambient temperatures, may be found in Figure 3.15. The latter difference was adequate enough to see a 0.07°C (late ebb) difference between the plume and ambient water. This is not ideal, and resulted in fewer deployments being used from that day, as the temperature difference was not adequate to clearly see the plume until later in the ebb, but at that point this was within the specifications of the temperature sensors, and was possible. On the remaining days, the difference was larger, which easily allows the use of temperature as a passive tracer in place of salinity.

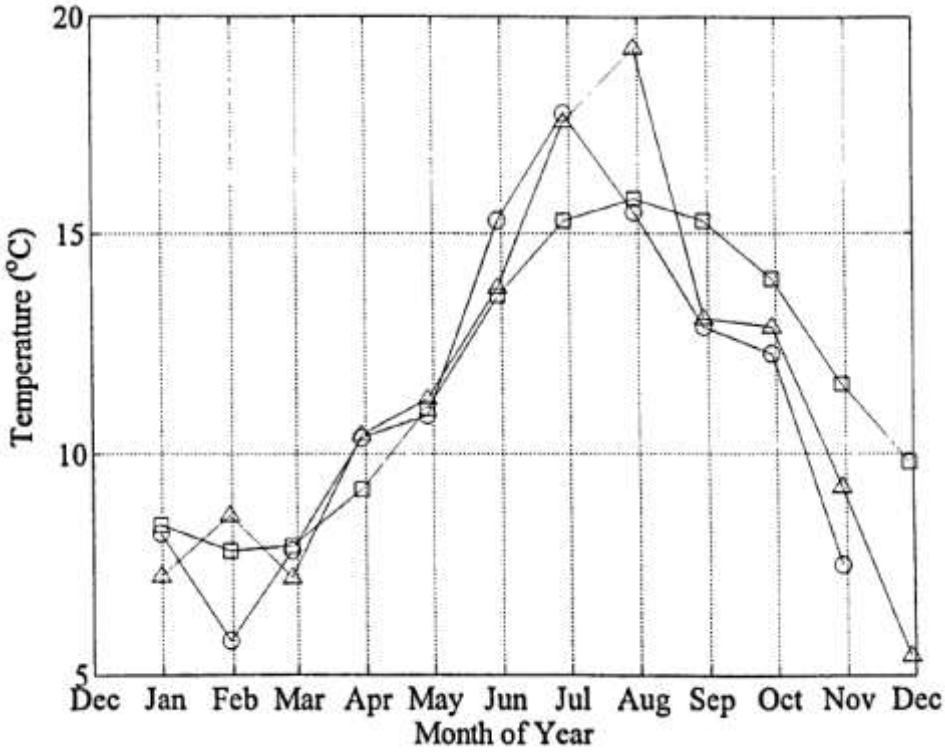

Figure 3.14: Seasonal comparison of sea surface and river temperature, with mean SST 1957-1989 (squares), river temperature 1995 (triangles) and river temperature 1996 (circles), from Pritchard, 2000.

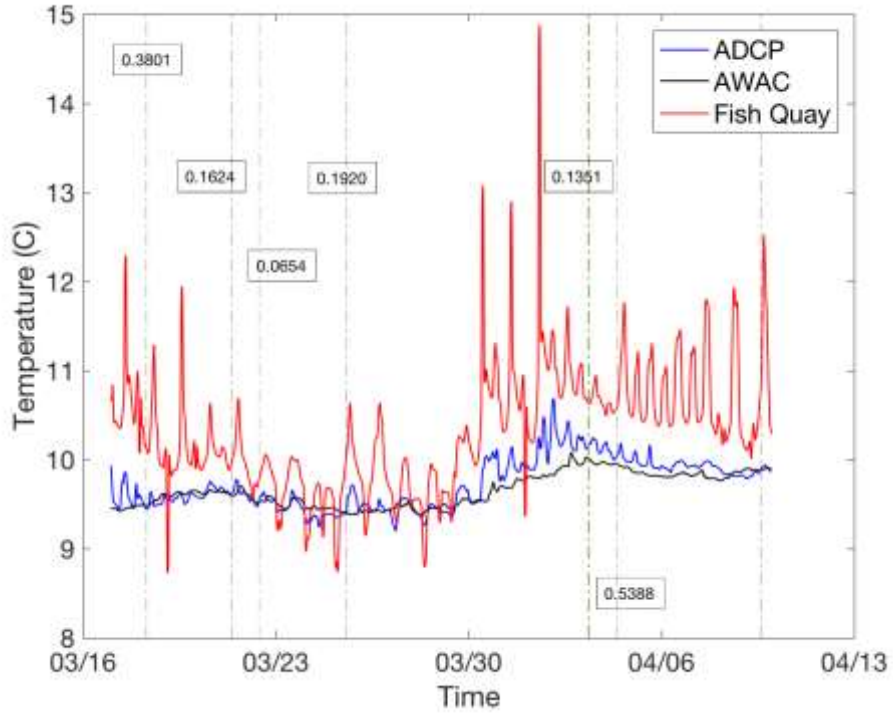

Figure 3.15: Difference in temperature between 3 sites: Fish Quay (0 m LAT, estuary), moored ADCP (5 m LAT, mouth), and moored AWAC (12.6 m LAT, offshore). Hashed lines indicate the start of the ebb tide for each drifter experiment, with midnight on April 3 in green. Boxed numbers indicate daily average temperature difference between plume and ambient water.

In an attempt to assess the accuracy of this approach, plume salinity was derived using a linear fit between drifter temperature and salinity from the CTD casts. There is support for this in the literature, as a TS relationship was used in the near-field region of the Merrimack River plume as a way to fill in gaps in salinity data (MacDonald, et al., 2007). The relationship between temperature and salinity was not always straightforward, and when comparing multiple days as in Section 4.3.7, those days were excluded from the analysis.

3.3.2.3.2 Two-layer flow: Richardson and Froude numbers

As a means of assessing plume stability, and how this may be correlated to entrainment and other plume parameters, the densimetric Froude number (Fr_d),

$$Fr_d = \frac{U_4}{c} = \frac{U_4}{\sqrt{g' h_p}} \quad (1)$$

and a bulk estimate of the Gradient Richardson number (Ri_g),

$$Ri_g = \frac{g \Delta \rho h_p}{\rho_0 (\Delta {U_4}^2)} \quad (2)$$

are calculated. Fr_d is essentially a representation of the balance between inertia and gravity or buoyancy forces, and can be used as an indicator of the intensity of mixing. Ri_g is a measure of the extent to which shear can overcome stability in a stratified flow, and it has been suggested that for $Ri_g < 0.25$, shear overcomes stratification leading to instabilities and mixing. For Fr_d, U_4 is taken as the velocity of the upper layer, or the drifter velocity +/- 1 minute of the CTD cast site, g' is the reduced gravity, and h is the plume thickness as determined subjectively by the user as the region with the largest density change, using the individual CTD cast profiles (region in red in Figure 3.16). For Ri_g, g is the gravitational acceleration -9.81, $\Delta\rho$ is the difference between averaged plume and ambient densities (above and below red layer in Figure 3.16), h is the plume thickness, ρ_0 is the mean density of both layers and ΔU the difference in layer velocities as determined by the drifter velocity at the surface, and a depth-averaged velocity below the pycnocline from the moored ADCP at the time of the cast. Drifter velocity was assumed to represent the whole plume layer, as in McCabe et al. (2008). As the plume layer is sheared this would lead to an overestimate of the plume velocity, and therefore overestimates of the Fr_d and Ri_g numbers. In this case these numbers are already bulk estimates, and will be used as relative values, rather than held to any strict limits or thresholds (i.e. $Ri_g < 0.25$).

ADCP data below the pycnocline were considered to provide meaningful estimates of lower layer velocity, as all casts used to calculate entrainment, and hence, Ri_g and Fr_d, were within 250 m of the moored ADCP, yet as this system does change over small spatial scales, this is another reason why it is important to identify these parameters as estimates.

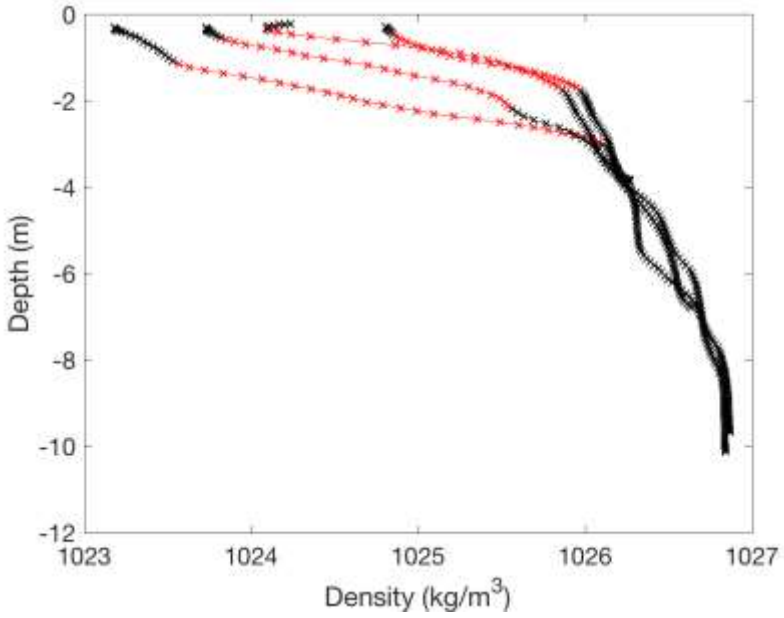

Figure 3.16: Sample density profile from April 3, 2014. Ri_g and Fr_d calculated using two layers, above and below the red section, and h representing the depth from the surface to the bottom of the red section.

3.3.2.3.3 Choosing track subsections

As the Teign plume is so much smaller than the Columbia plume, it is also shorter-lived. McCabe et al. (2008) analysed an 8-hour drifter deployment. Teign deployments were shorter: each being approximately 30-45 minutes long. During this period, many crossed what appeared to be the front into the ambient waters on the other side, resulting in 'in-plume' tracks that were closer to 15 minutes long.

The focus of this study was entrainment from shear stress only - from above (wind) and/or below (density-driven). To this aim, sections of drifter tracks between lift-off and plume front are extracted from the available data, in order to avoid contamination from entrainment from other sources, such as bottom stress and frontal mixing. Appropriate data segments are chosen manually. To avoid data influenced by frontal dynamics, the data are screened for steady increases or sudden changes in velocity or temperature, and may have been adjusted later if entrainment increased dramatically within a short distance of these changes in temperature or velocity (Figure 3.17). To identify source conditions, data is eliminated if CTD casts indicate bottom-attachment (i.e. a well-

mixed water column). Conditions considered ideal for the interior of a spreading plume are steadily decreasing temperature and velocities. Overall, only deployments with: segments that met these requirements, a consistent relationship between temperature and salinity, and evidence of two-layer flow are chosen for the analysis.

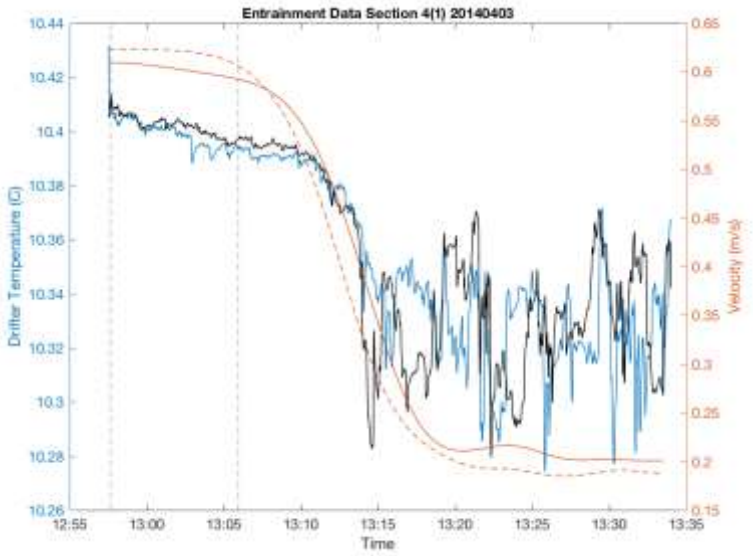

Figure 3.17: Example of drifter velocities (red) plotted with drifter temperature (blue and black), and the subsection chosen to avoid what appears to be a frontal feature, followed by a region of higher mixing.

3.3.2.4 Choosing T_e and S_e

Moving on to the entrainment calculations, the first step is to choose one T_e or S_e value for each individual cast at the base of the plume layer using the density profiles described in the previous section, and an average of those values from casts considered to be inside the plume was used as the representative value for ambient temperature or salinity. This is in contrast to the single isopycnal chosen in the McCabe study, but provides greater accuracy in this case, due to the dynamic nature of the plume.

The mixing or shear layer is established in order to specify T_e and S_e, the entrainment temperature and salinity, and as the base of the plume was defined in McCabe, et al. (2008) as the salinity or temperature of the water just underneath the overlying turbulent

plume, the S_e value is chosen as the isopycnal just below any mixing at all, or where the salinity profile is vertical. In our case, the isopycnal just below the biggest change in density was chosen, or the point at the bottom of the red layer in Figure 3.16, otherwise plume thickness would have been significantly overestimated in many cases. This does not change the analysis much, but is a more accurate representation of the plume, and resulted in track estimates that more closely resembled cast estimates. On April 3, both temperature and salinity profiles mirrored the density profiles, so this was acceptable. In the case of the multi-day results (see Section 4.3.7), if this was not the case, those data were escluded, or entrainment data based on salinity were considered more accurate.

3.3.2.5 Calculating the constant of integration

Once the previous steps are taken, the unknown constant of integration is calculated via equation (19) using values determined at, or in the vicinity of, the CTD casts. Velocity (u) and drifter spread (B) are taken as means of the drifter pair velocities and distances within a window +/- one minute of the CTD Cast. ΔT and ΔS are determined as the difference between plume salinity or temperature, S or T, and the entrained salinity or temperature, S_e or T_e. Both are calculated using cast values, so in this case, salinity is not derived directly from temperature. Plume depth (h) is established as described above using the isopycnal located just underneath the turbulent plume, as seen in individual CTD casts. Only constants from the subsection chosen were used for the calculations, otherwise, h would be over/underestimated along the track. An individual h is chosen for each cast, as changes in conditions between casts could result in variable plume thicknesses, as opposed to McCabe (2008), who acknowledged that "h may change for any given tidal pulse".

Once calculated, the constants of integration are compared to check that they are within the same order of magnitude. If not, some care is taken to determine why, and those data may not be included in the final analysis. If included, an explanation is provided.

3.3.2.6 Determining u, B and ΔT

Velocity (u) and drifter spread (B) are calculated over the entire track, the first as the change in drifter position relative to the change in time, and the second as the distance between drifters at any point along the drifter tracks.

The difference between plume temperature and ambient temperature (ΔT) is also calculated over the track, with plume temperature taken from the temperature measurements made by the sensor attached to the drifters, and ambient temperature as a mean of the T_e values taken from the CTD casts located in the subsection of interest. For track ΔS, plume salinity is derived using the linear fit, and ambient salinity is considered an average of the S_e values taken from the CTD casts. Lastly, the change of temperature or salinity with respect to distance along the track, $\partial T/\partial x$ and $\partial S/\partial x$, are taken as the difference between subsequent plume temperature or salinity values along the drifter track, and dividing by the distance travelled between each data point.

3.3.2.7 Calculating plume thickness (h)

Finally, using the constant of integration calculated above, along with u, B and ΔT, h is calculated over the selected track, again using equation (19).

3.3.2.8 Calculating entrainment, salt flux and diffusivity

Entrainment is then calculated via equation (20) over the entire drifter track. A 'cut-away' calculation at the site of the CTD casts is also performed in order to confirm the accuracy of the track values.

To calculate entrainment at the cast sites, the same h (from cast), u (from drifter), ΔT (from cast), and ΔS (from cast) are taken as were used to calculate the constant of integration, and $\partial T/\partial x$ or $\partial S/\partial x$ are 2-minute averages (+/- 1 from cast site) extracted from the track values. With the cast value for entrainment velocity (w_e), cast values for salt flux are determined using equation (18), using the entrained salinity (S_e) value

determined for each individual cast. This eliminates the error gained by estimating a track value for h, as h values are directly assessed by the CTD density profiles.

Track values for salt flux are also determined using equation (18), using the track value for entrainment velocity and the mean value for the entrained salinity (S_e), determined from all 'in-plume' CTD casts along that particular drifter track. In all cases, entrainment values are calculated using both temperature and derived salinity, and salt flux using entrainment velocities based on both temperature and derived salinity, but this is for comparison, in order to show that temperature is a viable replacement for salinity, but in most cases, the results will focus on those values based on temperature.

Eddy diffusivity is then calculated using equation (21) with $\partial S/\partial z$ taken from the CTD casts, and compared to those measured by the microstructure profiler (MSS). Track values for eddy diffusivity are not calculated.

3.3.2.9 The terms of the entrainment equation

The terms of the entrainment equation (17) are used for the assessment of the principle dynamics at play in the calculation of the entrainment velocity. As is evident from this equation, a change in plume thickness (h), velocity (U), or drifter spread (B) will result in entrainment.

The derivation of equation (17) results in the separation of the applicable terms. The 'thinning term' is defined as $u(\partial h/\partial x)$**,** and represents the change in thickness of the plume relative to distance multiplied by the plume velocity. The 'deceleration term', which is not technically a deceleration, is defined as $h(\partial U/\partial x)$, or the change in velocity with respect to distance multiplied by plume thickness, and the 'fractional spreading term', or $hU/B(\partial B/\partial x)$**,** represents change in plume spreading with respect to distance multiplied by the spreading as scaled for the velocity and thickness of this particular plume. If $\partial h/\partial x$, $\partial U/\partial x$ or $\partial B/\partial x$ become negative, the terms become negative (as in this case, U, h and B will never be negative) and thus entrainment is not indicated. When positive, entrainment is indicated, and it is the balance of these terms that determines the overall amount of entrainment. In this case, a plume will thicken, spread and decelerate due to entrainment of water into the plume layer.

3.3.2.9.1 The steady-state assumption

The attempt was made to improve estimates of $\partial U/\partial t$ and $U\,\partial U/\partial x$ (see equation 22) by using two 'staggered' groups of drifters with an approximate 45-minute gap between deployments. The drifter deployments typically overlapped each other by about 15 minutes. First, the local acceleration ($\partial U/\partial t$) is calculated using the data from the two consecutive drifter deployments, where available, in addition to the moored ADCP data. The two deployments are deemed compatible for this purpose if the second pair of drifters followed a similar path to the first pair (paths within 30-50 m of each other). The two drifter pairs are interpolated onto a common track (x) based on where they overlapped in space, and the difference in velocity with respect to time at each point along that track is determined. The ADCP surface data is extracted and also differenced with respect to time. The latter may not be as reliable at times, as the top bin may have been contaminated by the shear layer. This would result in a bias toward stronger deceleration between uncontaminated and contaminated datapoints.

An advective acceleration ($U\,\partial U/\partial x$) value is also calculated using velocity data that was simultaneously recorded by consecutive drifter pairs, and plotted at the mean along-track position, though this rarely overlapped with the chosen sections in this study. In addition, $U\,\partial U/\partial x$ values were calculated by differencing simultaneously recorded velocity data by the drifters and the moored ADCP, and though there will be some inaccuracy here, as the drifters did not always cross directly over the ADCP, they were close (within 25-100 m in the case of April 3).

3.3.2.10 Error

The largest source of error for the track values based on temperature is likely to be h, as this is the only value that was not measured directly. This is addressed by calculating the cast values, as h is then taken directly from the CTD casts. Additional error for the track values based on salinity is likely gained from the TS fit, and this is assessed in the results. Data are only used for the fit if determined to be inside the plume (similar water mass properties), hence only having a few casts to work with in most instances.

Additional errors will result from the equations themselves, either from differentiation or assumptions made in the equations, in addition to small errors from the smoothing spline and the instrumentation.

4 RESULTS: ENTRAINMENT AND COMPARISON WITH THE COLUMBIA RIVER

Below are the results of the control volume analysis as it was applied to the drifter deployment on April 3, 2014 in the Teign outflow; this includes entrainment, salt flux and diffusivity data, but also the preliminary results at each step of the analysis leading up to the entrainment calculations, as a means to provide context for the mixing parameters. In order to make the comparison to the McCabe study in the Columbia River, April 3 was chosen as conditions most closely matched those under which the Columbia River study was conducted. Both experiments took place 2-4 days after peak spring conditions, and wind was less than 4.1 ms^{-1} throughout (and upwelling favorable), freshwater input was very different, but that is unavoidable with these two systems, as freshwater input will always be much greater for the Columbia River plume, due to its size. The implications of this are discussed later.

4.1 Characterisation of the flow: April 3, 2014

Dynamically speaking, April 3 was the most straightforward day of the Teign experiment. It occurred 2 days past peak spring conditions, with maximum drifter velocities of 0.9 ms^{-1} on this day. Field notes indicate that the day was very wet, but very calm, with some very light breezes from the north. Modelled wind data indicates a north wind very early on (first deployment) at ~6 ms^{-1}, but from then, winds were overall less than 4 ms^{-1} and from the W, or offshore, earlier in the day, switching to SW, or alongshore (and upwelling favourable) later in the day. No local wind measurements were available for this deployment.

Freshwater input to the estuary was approximately 7.3 m^3s^{-1}, as calculated from the two largest tributaries to the Teign estuary (the Rivers Bovey and Teign). This was the third highest for the experiment, but still just under the mean river flow as calculated for the River Teign between 2004 and 2013. That value was 5.616 m^3s^{-1}, and for this deployment, the River Teign flow rate was 4.725 m^3s^{-1}. The depth–averaged residual current, as measured by the moored ADCP, started from the SW at the beginning of the ebb, and early on switched around to the N, stronger at first (~0.25 ms^{-1}) and then decreasing (~0.15 ms^{-1}).

During the particular deployments chosen, maximum drifter velocities were 0.64, 0.61, 0.52 and 0.46 ms^{-1} respectively. The temperature difference between the estuary and ocean water was ~0.9°C by the end of the ebb, with a 0.14, 0.13, 0.14 and 0.2°C bulk average temperature difference between plume and ambient for each deployment. For D5(1), ambient water decreases in temperature, presumably as the tide begins to turn, and this may contribute to an increased density difference at this stage of the ebb (). The naming convention for the deployments is as follows: ‘D’ for deployment, ‘N’ for deployment number, ‘(N)’ for the staggered group designation within that deployment (always 2 groups). So, for this day, D3(2), D4(1), D4(2) and D5(1) are the drifter groups of interest.

4.2 Drifter deployment: April 3, 2014

Below is a look at the four drifter groups (Figure 4.2 - 4.5), spanning 3.9-6 hours since high water (hshw), with a corresponding tidal curve (Figure 4.1). Drifters were initially deployed in a cluster, 1.5 hours after high water, in order to catch the initial formation of the plume at approximately that time. Peak ebb ocurred at ~3 hshw on this day. Seeing as buoyancy input was relatively low for the first 2.5 deployments on this day, plume dynamics were less straightforward, presumably due to a smaller density difference between plume and ambient, and larger tidal currents. Starting with D3(2), the buoyancy difference was high enough to clearly differentiate between plume and ambient water, due to the increased buoyancy influx from the upper estuary at this later stage of the ebb tide.

Once deployed, the drifters travelled approximately 1.25 km, 1 km, 1.25 km and 1 km, respectively, and the sections chosen for entrainment calculations were 140 m, 360 m, 325 m, and 500 m long. Below is an outline of results of the control volume analysis, somehwat loosely following the procedure as described above in Section 3.3.2.1, as a means for putting the results into a dynamical context.

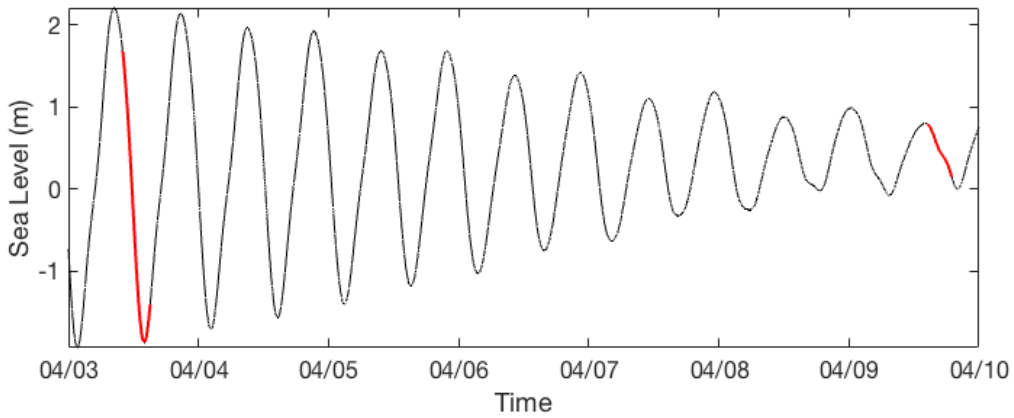

Figure 4.1: Tidal curve with drifter and MSS deployments in red.

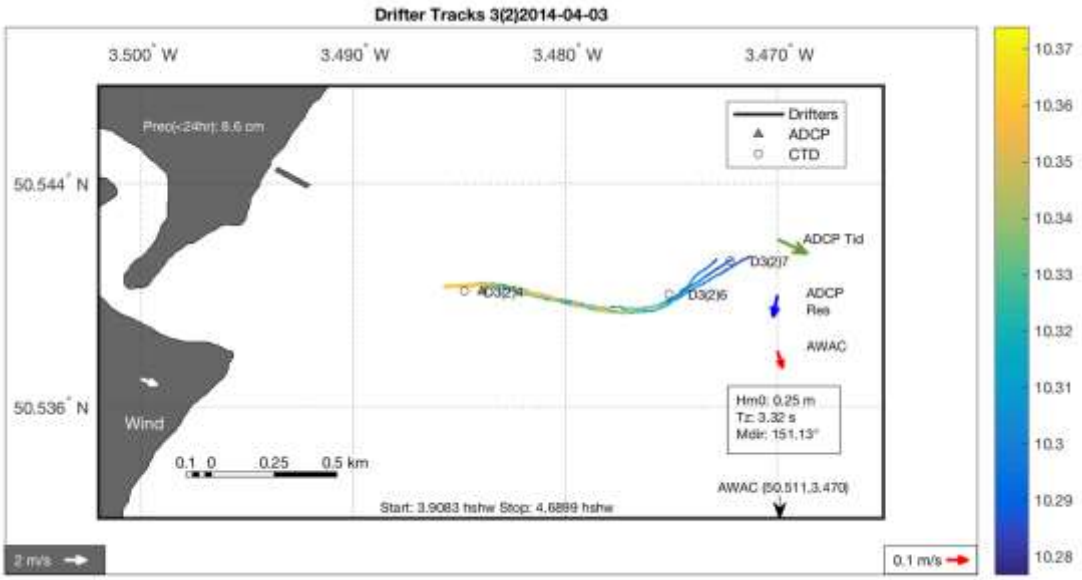

Figure 4.2: Drifter deployment 3(2) from April 3, 2014. Drifter tracks are overlaid with temperature (color scale in degrees Celsius, right). Precipitation from the previous 24 hours, upper left. Hourly wave conditions from the current period, lower right. The AWAC is located ~2.5 km south of the black arrow, and the moored ADCP is at the centre of the image. The wind vector (white arrow) is over the southern land mass ('The Ness'), but this is not where it was measured (3 km north). Current vectors for tidal (green) and residual (blue) velocity from the moored ADCP are middle right. Current velocity (tidal and residual) from moored AWAC (red), also middle right. The scale vector for currents (red) is in the frame, lower right, and the scale vector for wind (white) is in the frame, lower left. Time period denoted bottom centre, in hours since high water (hshw).

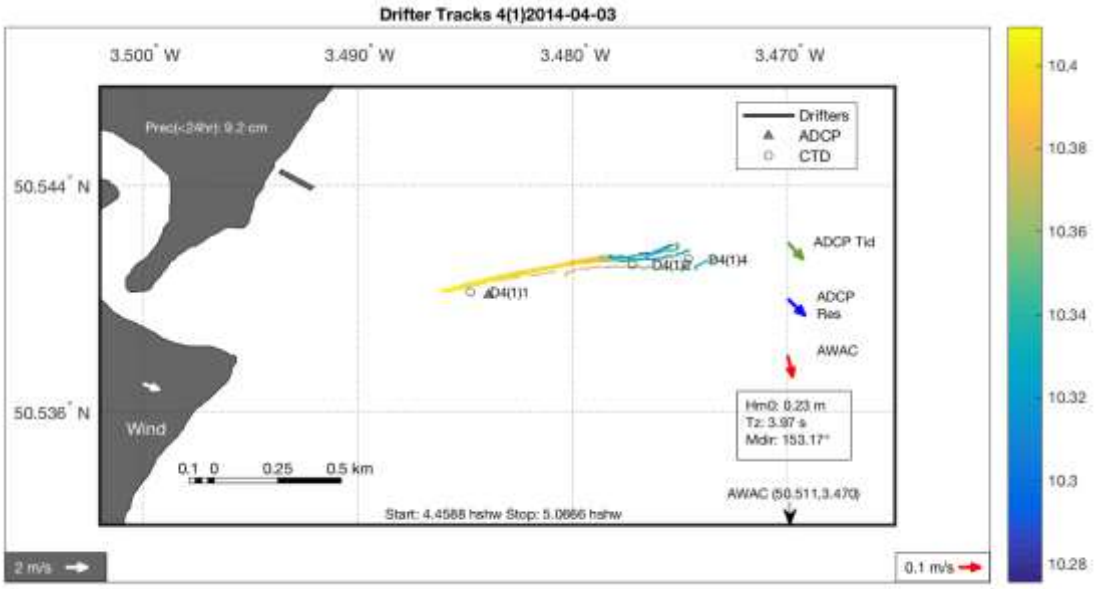

Figure 4.3: Drifter deployment 4(1) from April 3, 2014 (see caption above).

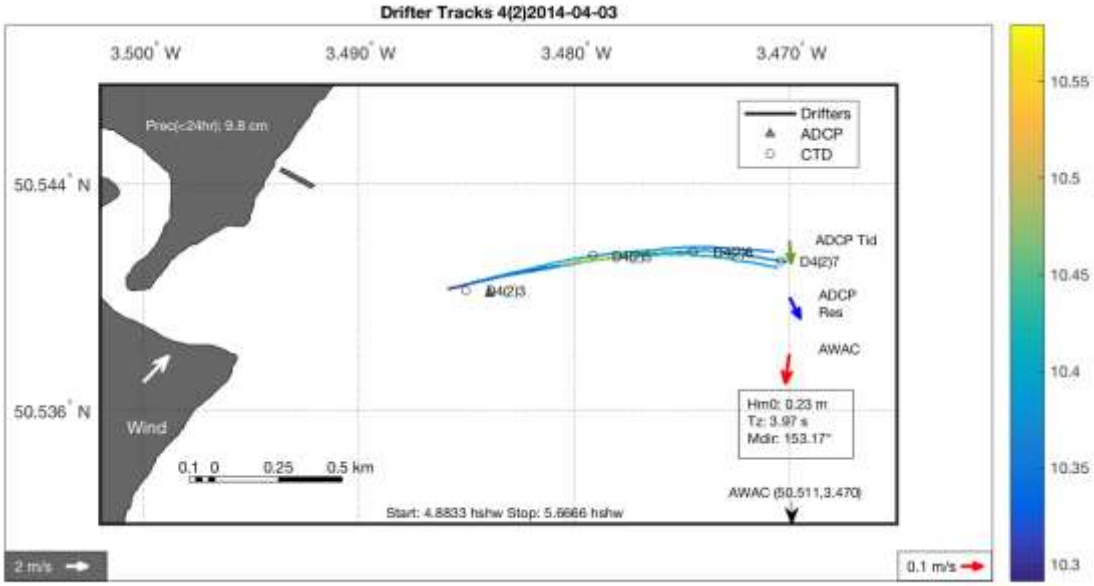

Figure 4.4: Drifter deployment 4(2) from April 3, 2014 (see caption above).

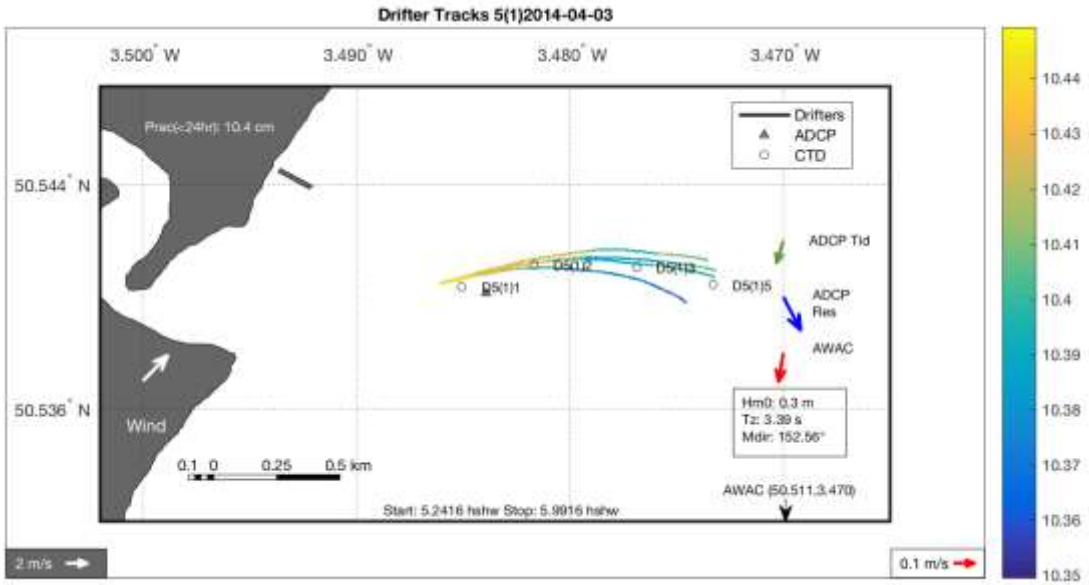

Figure 4.5: Drifter deployment 5(1) from April 3, 2014 (see caption above).

4.3 Control volume analysis: April 3, 2014

The sections following describe the results, presented loosely in the context of the procedure used to perform the control volume analysis, to first demonstrate the applicability of the method, as well as to provide context for the entrainment, salt flux and diffusivity data. First, a look at the choice of deployment, including density profiles, gradient Richardson numbers, and the choice of entrainment temperature (T_e). After that, the choice of track subsections, to provide some insight into the challenges faced working at this scale. Following that there will be a description of the results with respect to the constants of integration and modelled plume thickness (results of equation 19), and finally, entrainment, salt flux and diffusivity, including a look at the terms of entrainment from equation (17).

4.3.1 Density profiles: two-layer flow and choosing T_e

4.3.1.1 Density profiles: two-layer stratified flow

To start, some understanding of the structure of the two-layer flow is required to provide context for the entrainment velocity results. In this section is a description of the developing plume in terms of the stability of the upper layer, as this will inevitably affect entrainment.

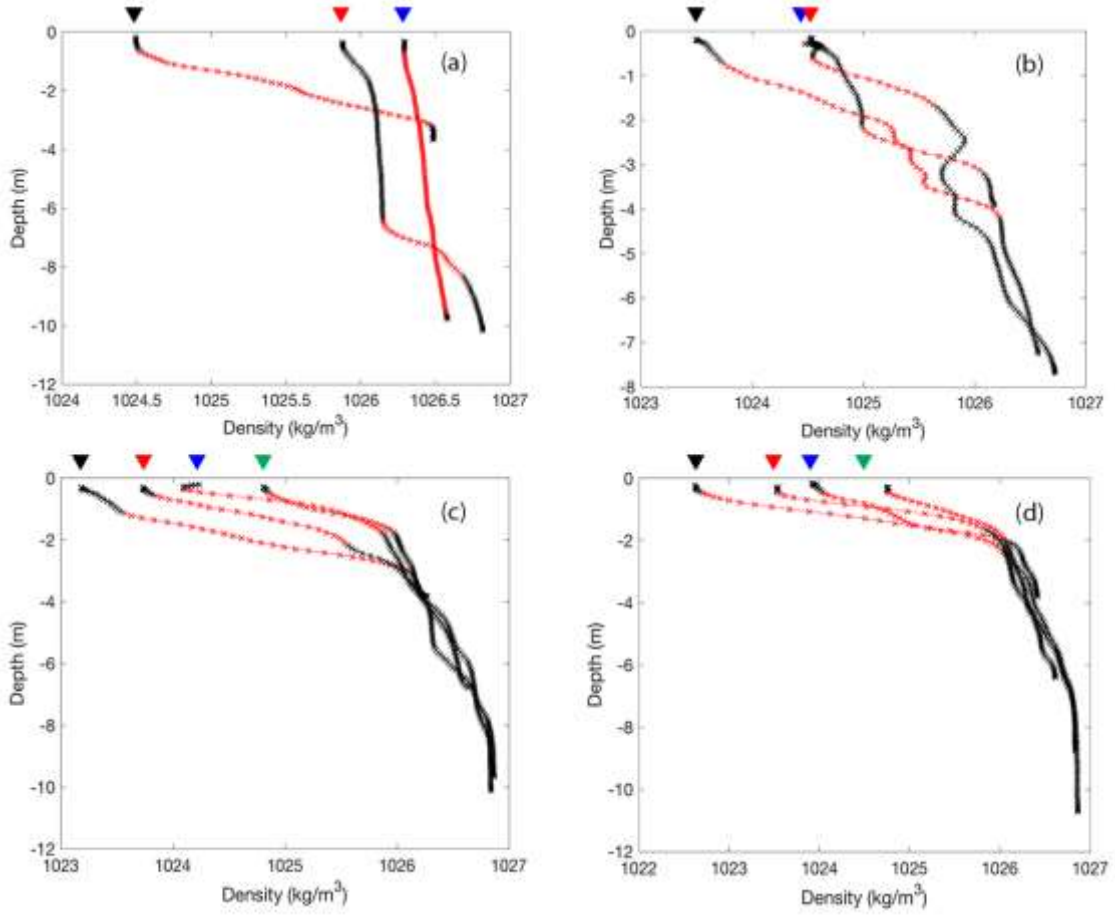

Figure 4.6: Density profiles for deployments 3(2) (a), 4(1) (b), 4(2) (c), and 5(1) (d) on April 3, 2014. Casts 1, 2, 3 and 4 are labelled by black, red, blue and green triangle, respectively.

Two-layer flow is a requirement for choosing a specific group of drifters for analysis. Looking at the density profiles (Figure 4.6) the shear layer, or boundary between the

upper buoyant layer and the lower, more dense ambient layer, is marked in red. Two-layer flow, exemplified by this shear layer, exists at all cast 1 sites, with a slightly thicker plume in the first three than during D5(1) (4 m vs 3 m). With each deployment, the density difference between plume and ambient becomes increasingly large, ranging from 1.98 kgm^{-3} at cast 1 for D3(2) to 3.7 kgm^{-3} at cast 1 for D5(1). When looking at all casts for all four deployments, one can see the progression of this flow, as the plume becomes more buoyant and therefore larger. It reaches as far as cast 4 in D4(2) and D5(1), with all casts showing a steadily thinning two-layer flow. It is worth noting that the plume reaches to within less than a meter of the seafloor during D3(2), and subsequent deployments are similar at approximately 1m, 1m, and 2m, suggesting close proximity to the lift-off zone, at least earlier on. In this case, the deployment site was only 0.6 km from the sandbar mentioned in Section 3.2.1, but it is still quite shallow and variable even beyond the bar, with depths of 4-6 m (at low tide) seen at the site of the first CTD cast.

When calculating the bulk estimate of the gradient Richardson number (Ri_g), the density anomaly between plume and ambient is determined using the two layers located above and below the red area in (Figure 4.6). Ri_g for each deployment was 0.24 (cast 1), 0.31 (cast 1), 0.48 (cast 1), 0.59 (cast 1) and 0.72 (cast 2), and the corresponding Froude numbers 2.63, 2.24, 1.85, 1.78 and 1.77 (Table 3). Both sets of numbers support this observed trend of decreased velocity and increased stratification and stability from D3(2) to D5(1). Flow is supercritical in all cases. Looking at D3(2), the first cast gives the only evidence for two-layer flow, and while the flow at cast 1 is stratified, it is not very stable, as the Ri_g and Fr_d numbers suggest a flow dominated by mixing. For D4(1), Ri_g and Fr_d suggest minimal stability, with profiles reflecting a greater density difference (2.52 kgm^{-3}), resulting in a slightly more stable two-later flow than D3(2). That said, similar velocities between the two deployments and the density inversion in the pycnocline both suggest active mixing at the base of the plume. For D4(2), the density difference is larger (2.8 kgm^{-3}) and velocities are slower by about 0.1 ms^{-1} than the deployment before, but the plume is a similar thickness (at this cast). For D5(1), flow is even slower, with the largest density difference (3.7 kgm^{-3} and 2.8 kgm^{-3}) and a thinner plume (~2.5 m at cast 1).

Table 3: Densimetric Froude number, gradient Richardson number (bulk value), and bulk Richardson numbers at cast sites on April 3, 2014.

	Fr_d	Ri_g	Ri_b
D3(2) Cast 1	2.67	0.24	0.14
D3(2) Cast 2	2.62	0.30	
D3(2) Cast 3	0.63	67.88	
D4(1) Cast 1	2.21	0.32	0.20
D4(1) Cast 2	0.85	6.60	
D4(1) Cast 3	1.16	4.11	
D4(2) Cast 1	1.84	0.49	0.30
D4(2) Cast 2	1.96	0.50	
D4(2) Cast 3	1.92	0.63	
D4(2) Cast 4	1.79	1.00	
D5(1) Cast 1	1.76	0.59	0.32
D5(1) Cast 2	1.82	0.68	0.30
D5(1) Cast 3	1.12	3.03	
D5(1) Cast 4	1.61	1.43	

4.3.1.2 Choosing T_e and S_e

T_e and S_e were chosen as the temperature or salinity value at the base of the plume, which again, is defined as the salinity or temperature of the water just underneath the overlying turbulent plume, or what is chosen here as the value at the base of the red shear layer in). In this case, T_e ranges from 10.22 at cast 1 of D3(2), increases to 10.29 for D4(1), and then stays constant at 10.3 for the same site during D4(2) and D5(1). For context, S_e ranges from 34.4 to 33.6 from D3(2)-D5(1). The changes in T_e and S_e are difficult to explain, as water should be being entrained into the plume, as water is

typically entrained from the less turbulent layer into the more turbulent layer, but detrainment and/or lateral entrainment (i.e. downwelling at the front) are possibilities. This analysis assumes lateral entrainment is zero, as Macdonald and Geyer [2004] found them to be negligible in the upper layers (< 5-6 m), as mentioned before, but a small amount may still occur.

4.3.2 Choosing the subsection of track

The next step in calculating entrainment was to choose the subsection of the drifter tracks that appeared uncontaminated by source or frontal influences. In this case, the cut is made before any major changes in velocity or temperature, which suggests the presence of a feature that could be a front. Within these subsections, CTD casts were performed, and only these casts were used to calculate entrainment parameters.

Only cast 1 was used to calculate constants of integration for the first three deployments, and casts 1 and 2 were used for the last deployment. For D3(2), the casts that were not used (2-4) were located after a sharp decrease in temperature and in an area of apparent high mixing, as demonstrated by increased variability in temperature and velocity data (see Figure 4.7a, and Figure 3.17). For D4(1), cast 2 (first unused cast) coincides with a sharp decrease in both temperature and velocity (Figure 4.7b), presumably a front. Froude numbers were subcritical at subsequent casts, lending support to the front theory. For D4(2), the constants of integration calculated using unused casts 2-4 are all an order of magnitude larger than that that calculated at cast 1, likely due to a significant shift in dynamics between cast 1 and cast 2. This is not obvious in Figure 4.7c), but will be explained in a subsequent section. By D5(1), the plume was larger and more stable, allowing the use of casts 1 and 2, with casts 3 and 4 being located close to or within what could be a front, as judged from an increase in temperature and velocity (Figure 4.7d).

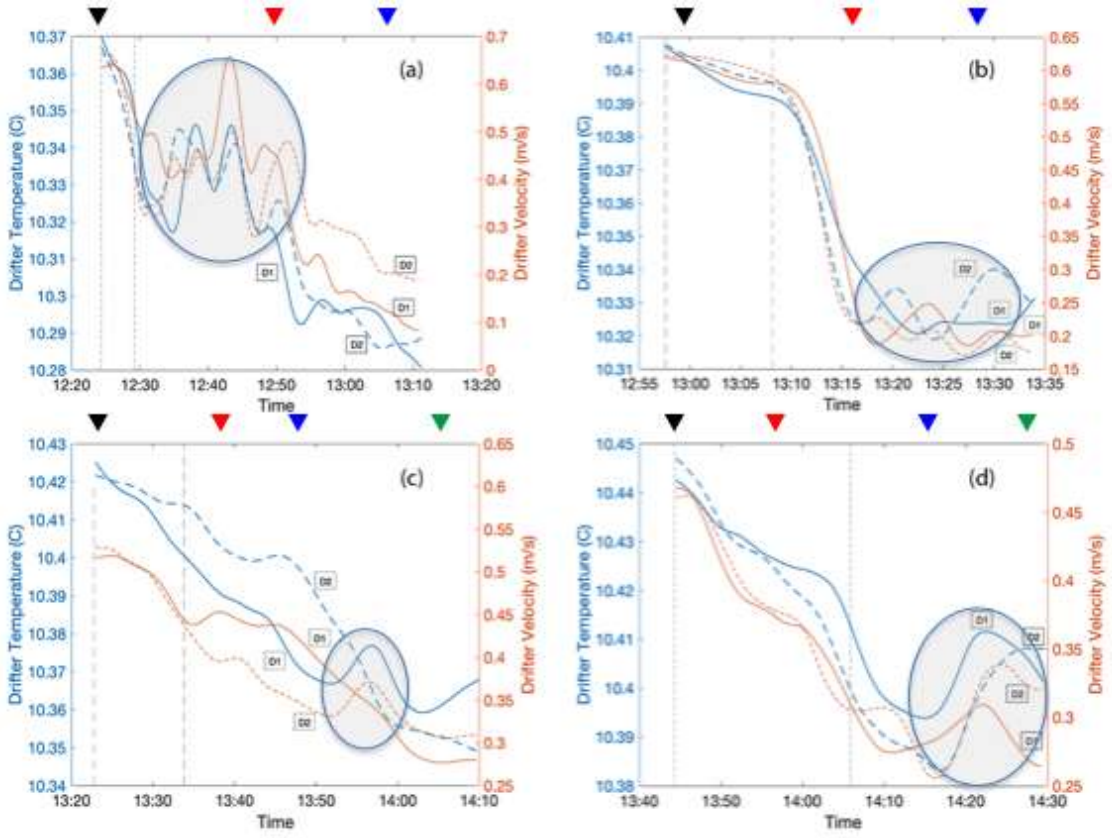

Figure 4.7: Drifter velocity and temperature for D3(2) (a), D4(1) (b), D4(2) (c), and D5(1) (d) on April 3, 2014. Shaded area shows regions with apparent mixing (i.e. fronts). Casts 1, 2, 3 and 4 times are marked by a black, red, blue and green triangle, respectively.

4.3.3 Plume thickness

Figure 4.8 represents the plume thickness h, in the chosen subsection of the drifter tracks, as calculated using U, B, ΔT and the constants of integration (equation 19). As a reminder, constants in the chosen area were the only one(s) used in this calculation.

Modelled plume thicknesses appear mostly accurate for all four deployments, when compared to cast values, though potentially slightly underestimated at the end of D4(2) and slightly overestimated/underestimated at the beginning/end of D5(1). This would be expected depending on where the casts were located along the track. The constants of integration were calculated at the site of each cast, and dynamics along the track in D4(2) occurred at very different scales between cast 1 and the remaining casts, so as one

gets closer to cast 2, the dynamics would have changed such that *h* would not be as accurate as if the constant from the closer site (cast 2) was used. In the case of D5(1), constants from cast 1 and cast 2 were used, and in this case, a mean constant was used to calculate *h*, introducing some error by virtue of the fact that the constants were not exactly the same.

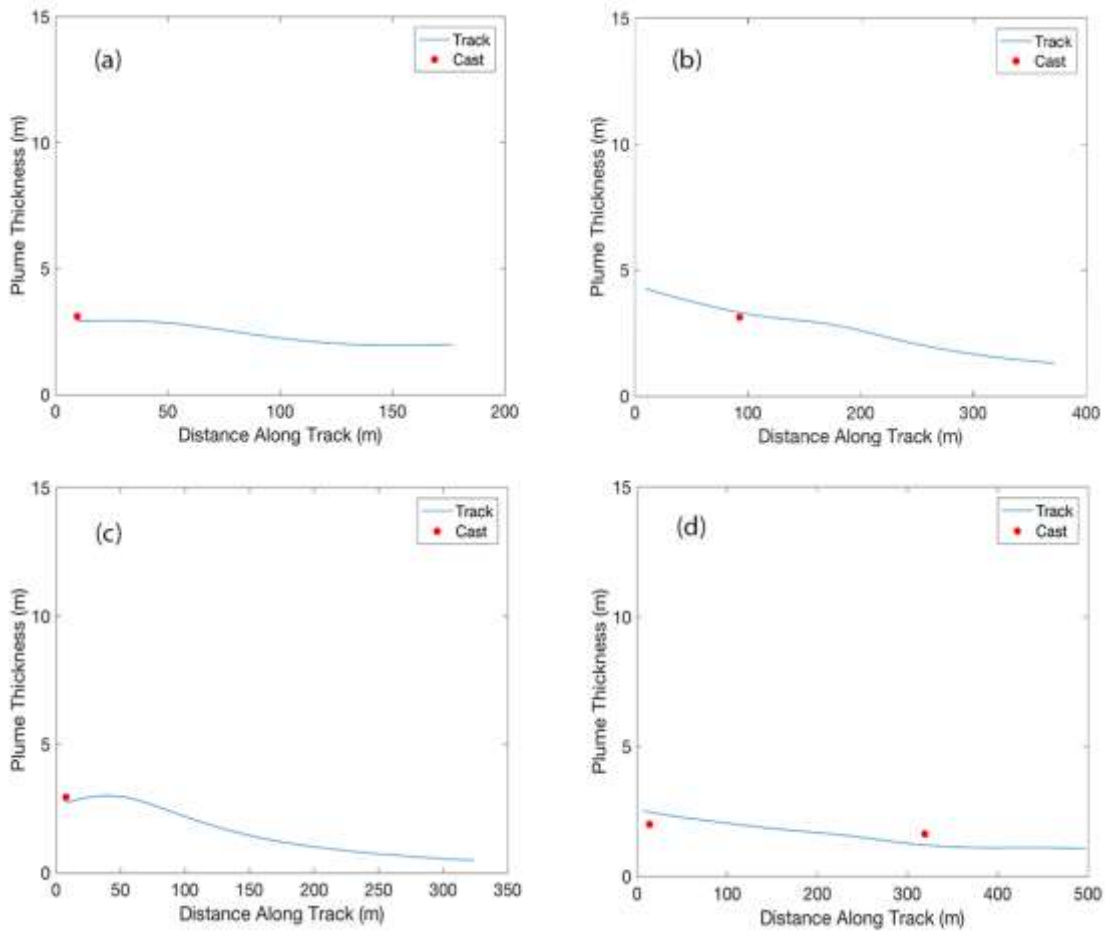

Figure 4.8: Modelled plume thickness (*h*) for D3(2) (a), D4(1) (b), D4(2) (c), and D5(1) (d) on April 3, 2014. Cast values of *h* (red) are overlaid on the results of equation (19) (blue).

4.3.4 Entrainment

On April 3, the mean value for entrainment velocity as calculated using temperature for the four deployments chosen was 4.3 x 10^{-4} ms^{-1}. The mean cast value was slightly

higher at 7.6 x 10^{-4} ms^{-1}, which makes sense as the casts are typically located at the beginning of the tracks, where entrainment velocity is likely to be highest. In the case of D3(2), along-track entrainment velocity is highest at the end of the track, thought to be due to the drifters approaching an area of high mixing.

A difference between the cast and a 2-minute average of track values at the site of the cast was determined as an indicator of error, in order to compare values where *h* is calculated versus measured directly. That number expressed as a percentage of the cast entrainment values is included in Table 4 in Appendix 1, in addition to entrainment values for each deployment (based on temperature as well as salinity).

Looking at track values first, as seen in Figure 4.9, entrainment was highest at the start of D3(2), with values close to 1.5 x 10^{-3} ms^{-1}, which decreased at first, and then increased through the remainder of the section, due to the proximity of what appears to be an area of high mixing. The chosen section in this case was relatively short for this same reason. The following deployment starts closer to 1.1 x 10^{-3} ms^{-1}, and then decreases through the remainder of the section. Next, for D4(2), entrainment velocity is slightly less than the previous deployments, at 7 x 10^{-4} ms^{-1}, and then decreases through the remainder of the section, with a smaller bump at about 200m. The longest section is last, and for D5(1), entrainment starts lower, at 4.3 x 10^{-4} ms^{-1}, and then is variable, with a maximum velocity of 6.8 x 10^{-4} ms^{-1}. Entrainment increases at the end of this section, very likely due to the proximity of a front. The track averages did not include the increases at the ends of D3(2) and D5(1). These were left in the figures to demonstrate the effects of potential fronts, but frontal effects are not meant to be included in the mean estimates.

Before looking at the dynamics more closely in a subsequent section, in all four deployments, the drifters encountered what appears to be an area of high mixing just after the chosen section, hence reinforcing the bounds of what is considered 'plume interior'. For all deployments, it is presumably a front. Whether it is *a* front, or *the* front, is difficult to say, as multiple fronts are possible, even likely based on previous observations (Pritchard, 2000).

Cast values agree pretty well with the track values for this deployment. The mean difference between cast values and track values, at the cast locations, for D3(2)-D5(1) is approximately 1.2 x 10^{-4} ms^{-1}, which is 18% of the mean cast value. The largest difference between cast and track values occurs during D5(1), and can be partially

attributed to errors associated with the calculations; for instance, along the D5(1) section, the disagreement between cast and track values may be attributed to the fact that 2 casts are used here, with an average of the constants being used for this section. For all deployments, there will be additional (small) errors associated with calculating entrainment velocity at the cast sites using mean drifter values for $\partial T/\partial x$ and velocity; taking 2 minute mean values, as well as the assumption that the drifters were co-located exactly with the CTD cast (they were within 20m, in most cases).

Seeing as we avoid the frontal zone, entrainment is typically highest at the beginning of the tracks, likely due to proximity to the source, and/or lift-off zone, where entrainment is also high as the plume rapidly spreads and shoals after losing contact wth the bottom. In addition, In this case, the increased entrainment may also be associated with a transition between jet and plume, as the drifters converge for the first ~20 m for two of the four deployments (D3(2) and D4(2)), and evidence in the raw data suggests the same for D4(1) (Figure 4.12). This convergence could be indicative of jet behavior, where momentum dominates, versus a plume, where buoyancy, and therefore spreading, dominate. This may be due to stronger tidal currents, and the proximity of the lift-off zone to the deployment site. Currents have slowed enough by D5(1), that a possible jet is not evident during this deployment.

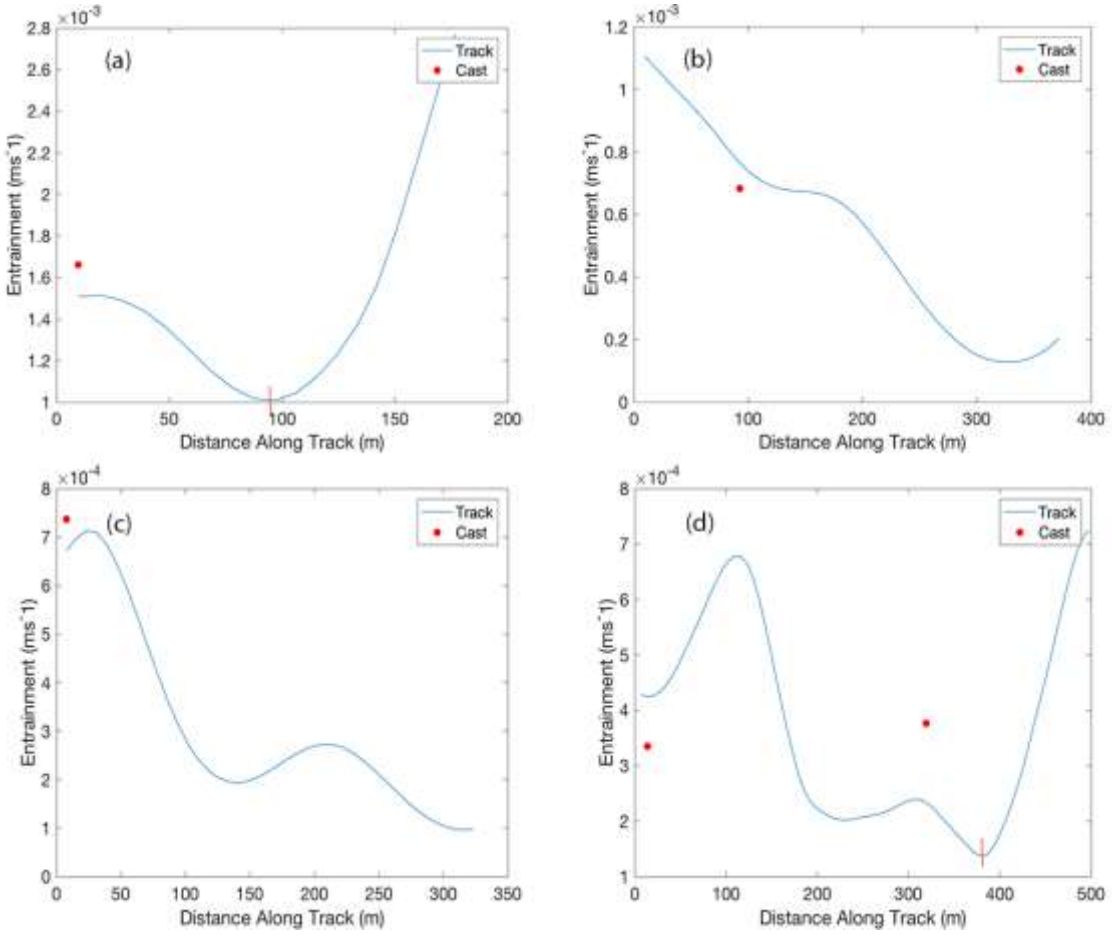

Figure 4.9: Along-track entrainment velocity (ms^{-1}), from equation (20), for D3(2) (a), D4(1) (b), D4(2) (c), and D5(1) (d), with cast values (red) added for demonstration of accuracy. Data after red lines in (a) and (d) were not included in track averages. Overall 95% confidence interval: [1.09×10^{-4}, 1.55×10^{-3}].

4.3.4.1 Entrainment based on salinity

When calculated using salinity (equation 20), the mean of the track entrainment values for April 3 was 6.9×10^{-4} ms^{-1}, and the mean of the cast values was 1.4×10^{-3} ms^{-1} (Figure 4.10). Values calculated using temperature and salinity are within 2.6×10^{-4} ms^{-1} for track values and 5.88×10^{-4} ms^{-1} for cast values.

Errors between cast and track values as calculated from salinity may be associated with the derivation of salinity through the linear fit between cast salinity and drifter temperature, as cast values included a 2 minute average of $\partial S/\partial x$ at the cast site, which was calculated using the derived salinity from the TS fit. Cast entrainment values for

salinity are likely to be slightly more reliable than track values, as ΔS is gleaned from the casts, and not the TS fit. Though in this case, the two are close, demonstrating that both are likley to be fairly accurate, on this day.

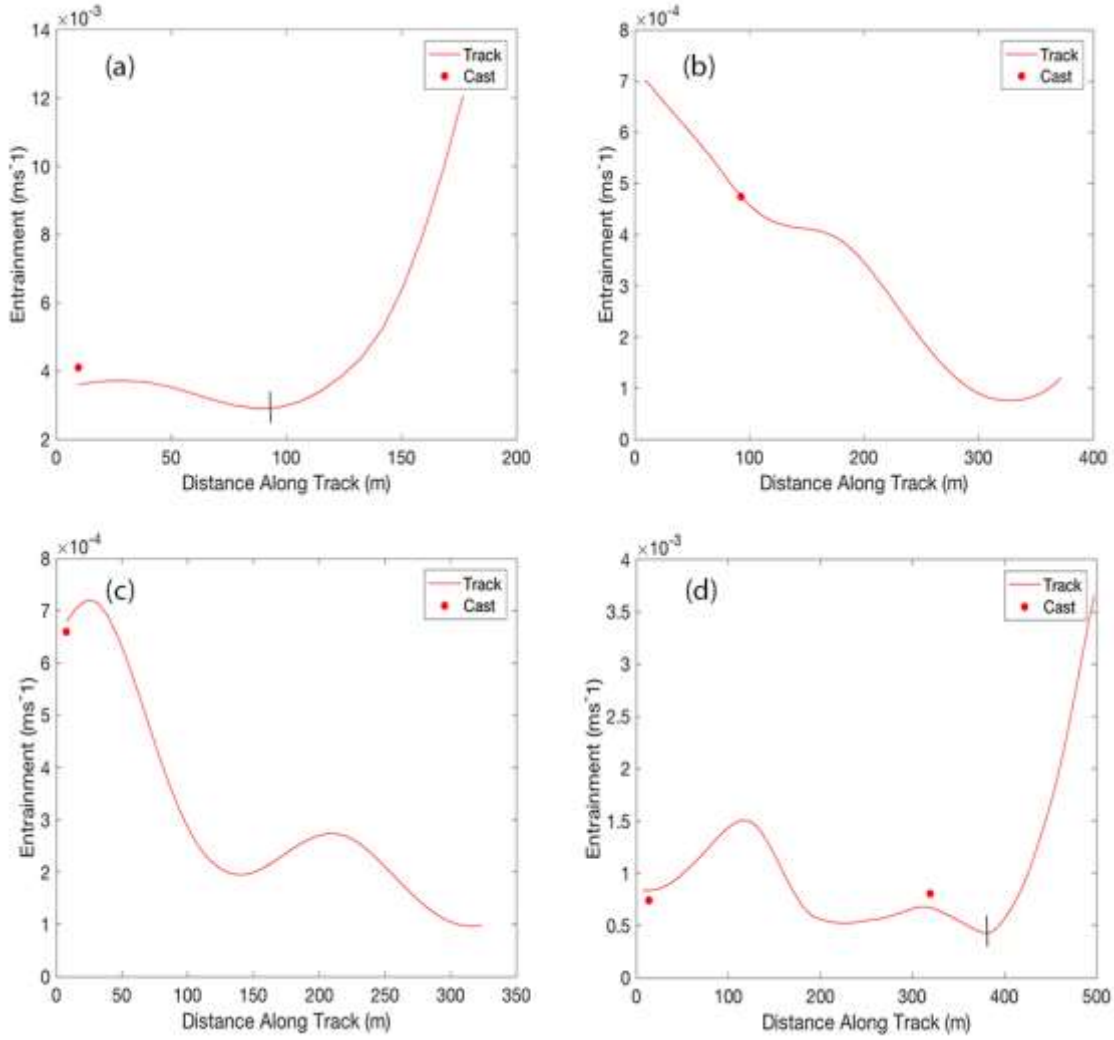

Figure 4.10: Along-track entrainment velocity in ms^{-1} based on salinity, from equation (20) for D3(2) (a), D4(1) (b), D4(2) (c), and D5(1) (d), with cast values (red) added for demonstration of accuracy. Data after black lines in (a) and (d) were not included in track averages.

Additional errors would be associated with the TS fit itself, especially as the smallest difference between temperaure and salinity entrainment values is seen in D4(2), where the fit is the most solid (Figure 4.11c). To be clear, the figure shows the TS fits as they would be if all casts were used (r-squared included, bottom right). Only casts 1 and 2

were used in the T-S fits for D3(2) and D4(2). This seemed the most accurate approach, as described in a previous section. Again, each of the remaining deployments have an issue; for D3(2) and D4(1), the second cast very obviously lies on the other side of an area of high mixing. For D5(1), the dynamics appear to be slightly more complicated, potentially due to the late stage of the ebb, but cast 2 also lies on the other side of what could be a front between the cast sites. The decision was made to use both constants when calculating *h* for D5(2), based on the fact that the constants were of the same magnitude, suggesting similar water properties, but it could be that a small front or other feature could exist there, possibly adding (a small) error.

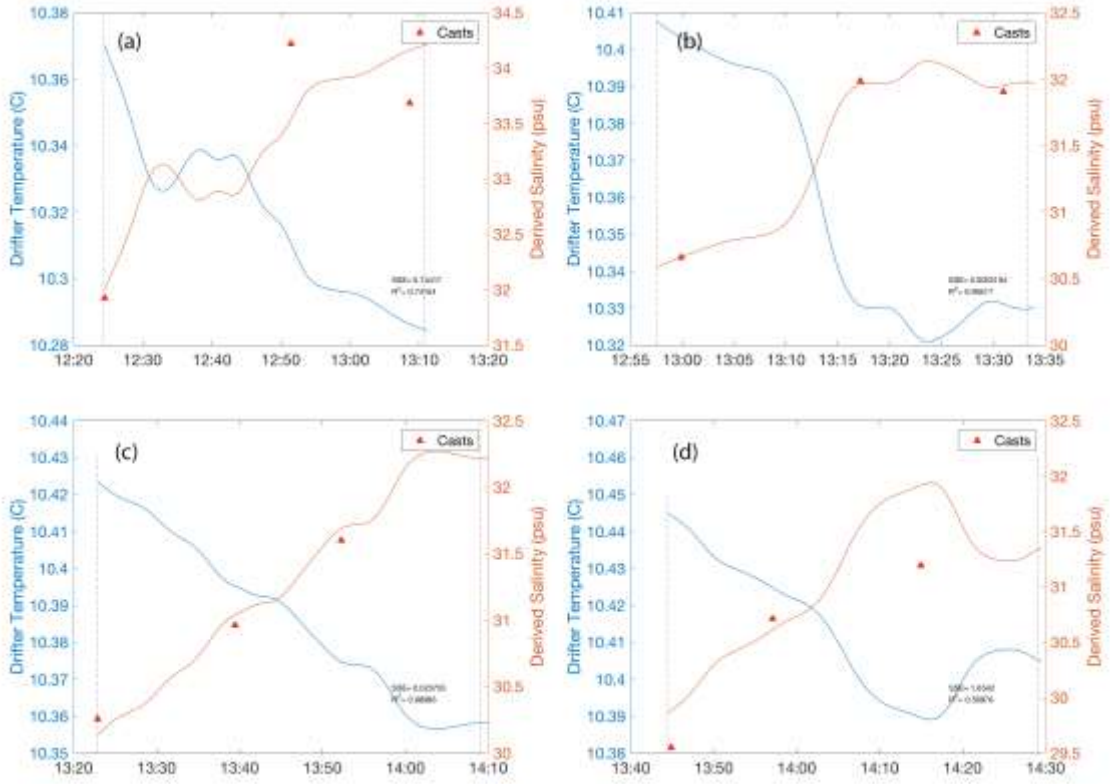

Figure 4.11: Results of linear fit between cast salinity and drifter temperature for the full paths of D3(2) (a), D4(1) (b), D4(2) (c), and D5(1) (d). All fits were only performed with the first two casts, with D4(1) as only exception. All three were used. R-squared values are at bottom right.

4.3.4.2 Terms of entrainment equation

As mentioned, the terms of entrainment from equation (17) may be used as a diagnostic tool to evaluate the dynamics at play in the entrainment calculations.

In the first and third cases (D3(2) and D4(2), see Figure 4.12 (a and c)), a positive thinning term dominates a negative spreading term to start, and then both cross over so that a positive spreading term then dominates the negative thinning term. Deceleration is slightly positive initially for D3(2), and less so for D4(2), and then as spreading increases, becomes negative. This all suggests that the plume is not spreading to start, but thickening and accelerating slightly, as would happen either during lift-off or a jet-plume transition. There is some evidence in the raw data that a similar thing happens during D4(1), but there is a sharper increase in spreading just after, which cancels out the initial decrease in spreading when the spline interpolant is applied.

For all deployments, by 50 m, the plume actively spreads and shoals, with the former indicating entrainment and the latter not. For D3(2), spreading slows and the plume thickens at the end of the section, consistent with the approach of a front-like feature. For the remaining deployments, fractional spreading and thinning decrease over the length of the track, with quite a few wobbles in D5(1), as the drifters move and spread inconsistently, with a stronger deceleration term, possibly due to the impending onset of the flood tide. At the end of D5(1), the thinning term becomes positive, indicating the approach of an area of mixing.

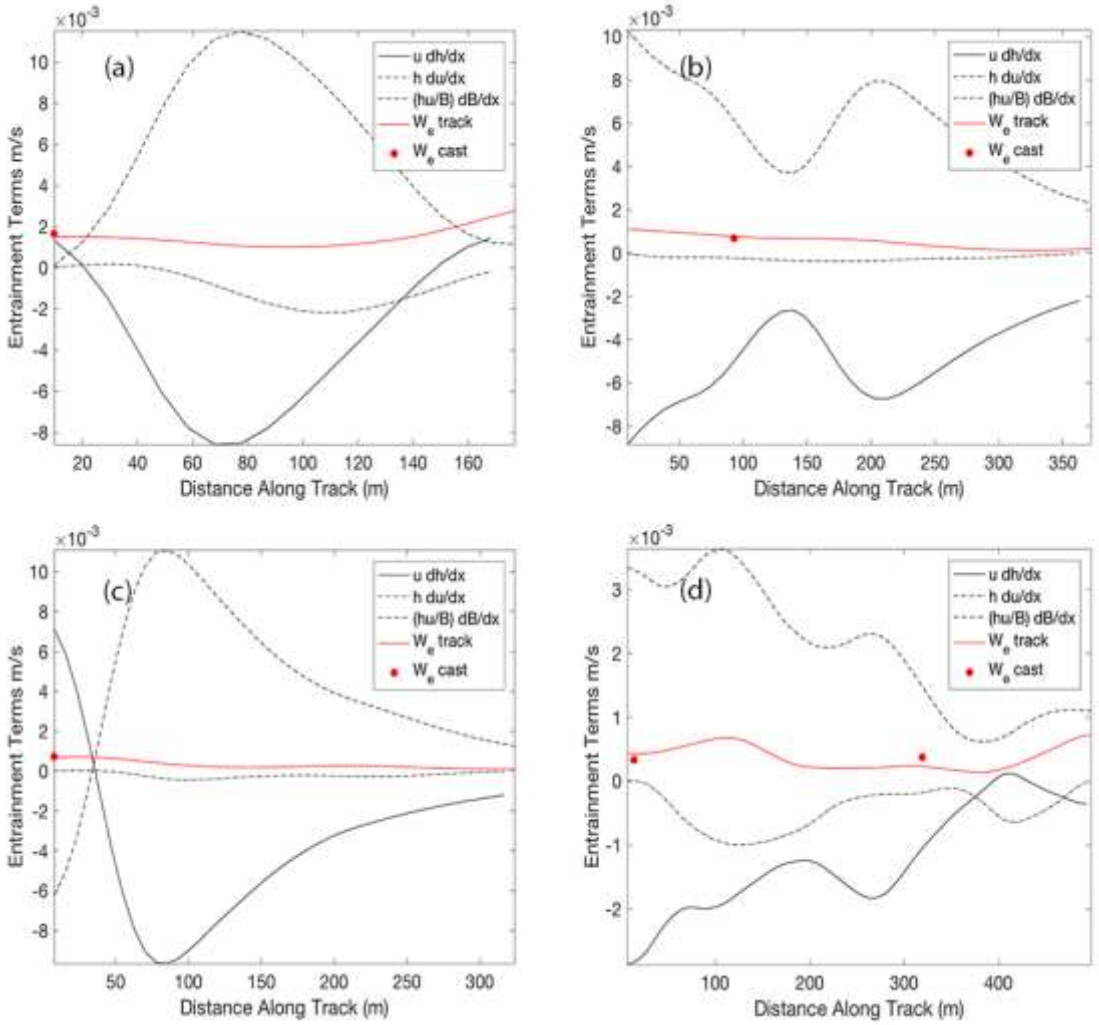

Figure 4.12: Terms of entrainment equation (17) for D3(2) (a), D4(1) (b), D4(2) (c), and D5(1) (d): thinning (solid black), deceleration (dashed and dotted black), fractional spreading (dashed black) and entrainment velocity (red).

4.3.4.3 The steady-state assumption

In the case of the Teign study, because the chosen sections were so short (9-20 minutes long in the case of April 3), the staggered approach did not work as well as hoped. The lag between staggered deployments in this case were 25-35 minutes. As there is no overlap in time or space between drifter pairs, the staggered $U\,\partial U/\partial x$ value is a little suspect. Though looking at both the staggered data and the ADCP data, taking into account that the lower spikes (faster deceleration) could be attributed to the shear layer, $\partial U/\partial t$ is smallest during D3(2) at 10^{-6} ms^{-2} and increases only slightly in subsequent

deployments to an average value of -5 x 10^{-5} ms^{-2}. This is less than or consistent with other plume studies (Chen et al., 2009), and considered sufficiently small relative to other terms in the entrainment equation, which were typically 2 orders of magnitude larger. In addition, when compared to ADCP values of $U\ \partial U/\partial x$, $\partial U/\partial t$ was considerably less than 25% of $U\ \partial U/\partial x$. Staggered $U\ \partial U/\partial x$ values were considered unreliable, as the drifters never overlapped in time or space, considering the shortened tracks. All suggest a limited effect of time-dependent terms on the entrainment results.

4.3.5 Salt flux and diffusivity

In theory, entrainment values calculated using either temperature or salinity could be used to calculate salt flux, as it is the velocity associated with entrainment and *should* be the same when calculated with either temperature or salinity. In this case, for this deployment, entrainment velocities calculated from temperature are more reliable, and will be reported here.

Track values for salt flux mirror entrainment as it is just the entrainment velocity multiplied by the entrained salinity (or S_e). Track and cast results show similar trends as seen in the entrainment results. The mean along-track salt flux, for D3(2), D4(1), D4(2) and D5(1) was 1.5 x10^{-2} psu ms^{-1}, and for cast values, 2.6 x 10^{-2} psu ms^{-1}, and again, with casts being located close to the beginning of the track, this makes sense. To see values for each deployment, see Table 5) in Appendix 2.

Using equation (21), and the salt flux calculated at the cast sites from the temperature entrainment velocity, diffusivity at the cast sites was 5.8 x 10^{-2} m^2s^{-1}, 2.0 x 10^{-2} m^2s^{-1}, 1.4 x 10^{-2} m^2s^{-1}, 4.7 x 10^{-3} m^2s^{-1}, and 5.2 x 10^{-3} m^2s^{-1} for D3(2)-D5(1). The mean of all diffusivity estimates at the cast sites was 2.0 x 10^{-2} m^2s^{-1}. All values show the same trend as with entrainment and salt flux: highest values for D3(2), decreasing through to D5(1).

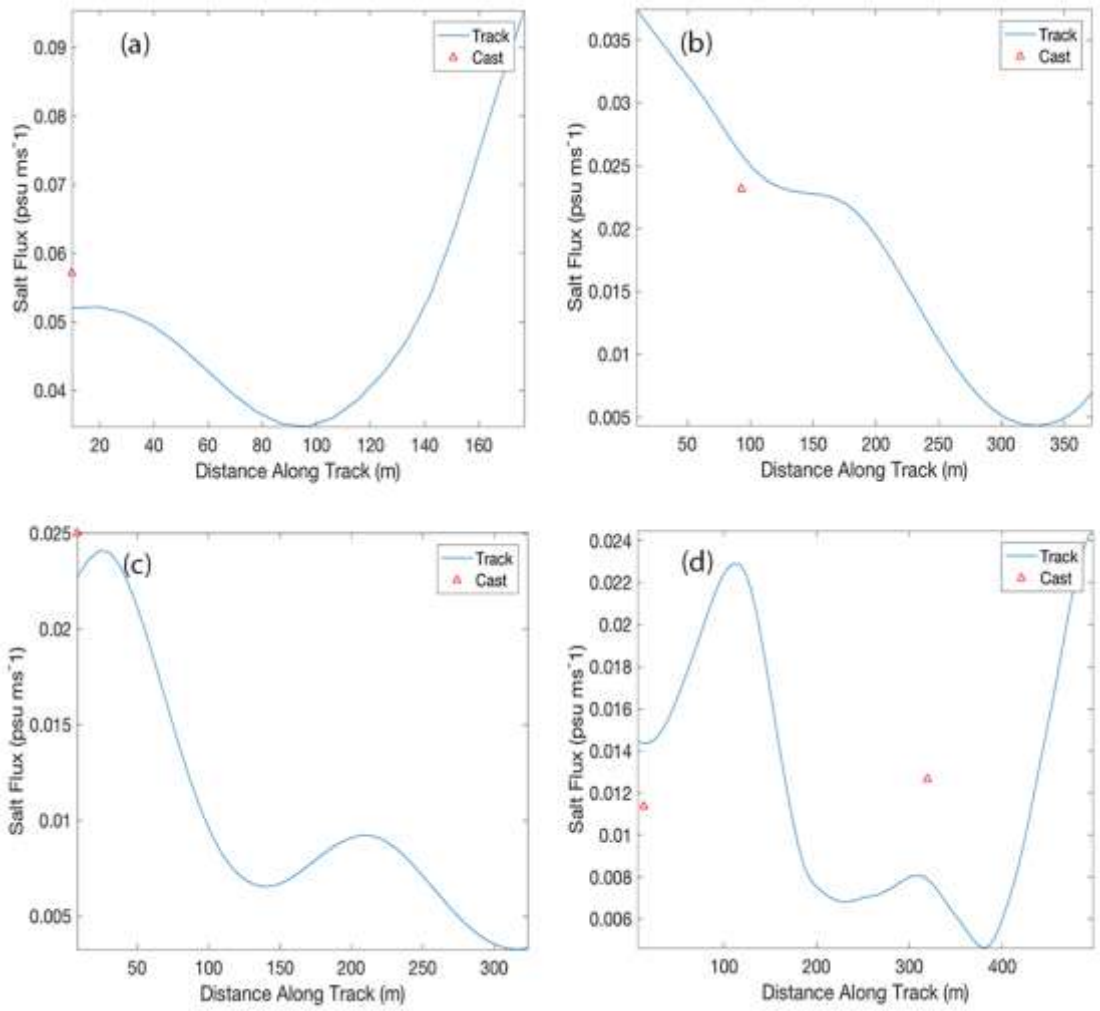

Figure 4.13: Along-track salt flux in psu ms^{-1} based, from equation (18), for D3(2) (a), D4(1) (b), D4(2) (c), and D5(1) (d), with cast values (red) added for demonstration of accuracy. Overall 95% confidence interval for salt flux: [3.68 x 10^{-3}, 5.34 x 10^{-2}], and for diffusivity of salt: [4.2 x 10^{-3}, 5.75 x 10 $^{-2}$]. The confidence interval for diffusivity is only based on 5 values.

4.3.6 Comparison with MSS

Microstructure data was collected six days after the deployments discussed here, without drifters. The profiler was deployed during a single ebb tide at peak neaps on April 9, 2014 (Figure 4.1). Winds were light and southerly (<4 ms^{-1}), and freshwater input to the estuary was the highest of the experiment at 9.9 m^{3}s^{-1}. A front was observed

visually passing the boat during the time when the highest diffusivity values were measured.

There are some gaps in the data due to difficulty managing the rising profiler in any level of wind, but a mean value for the shallowest diffusivity values from the top meter of the water column was 0.6341 m^2s^{-1}. These data include measurements from the frontal and ambient zones, including a number of mysteriously high values ocurring just before the passage of the front ($O(10)$ m^2s^{-1}), which likely skewed the average slightly high. Taking an average of all values where salinity is less than 34, the result is 2.6 x 10^{-2} m^2s^{-1}, which is much closer to the range of values calculated using the drifters.

Figure 4.14 shows drifter K_s values alongside MSS surface K_ρ values, with April 3 in green, all on a base 10 scale. The MSS was recovered early with respect to the end of the ebb, relative to the drifters, but values still agree well.

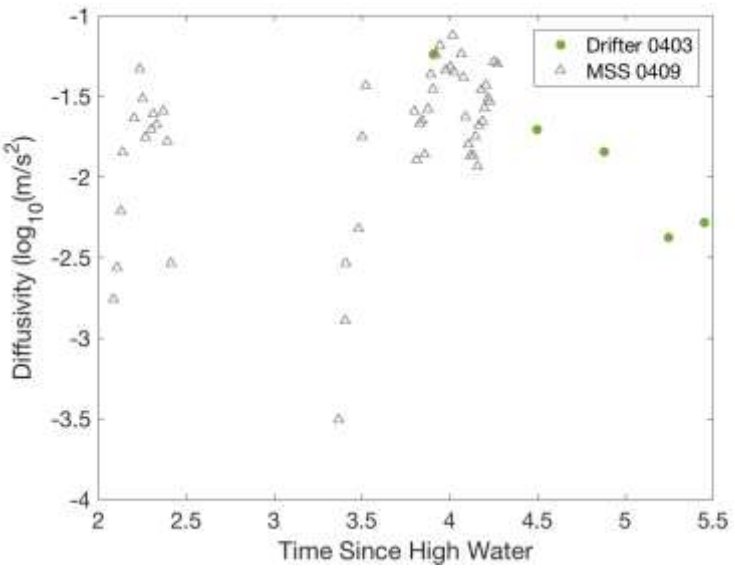

Figure 4.14: Diffusivity of salt (K_s) estimates for April 3 (green), including those captured by the MSS (K_ρ, grey) on April 9, 2014. Overall 95% confidence interval (log10 scale): [-3.03, -1.173].

4.3.7 Entrainment with variable conditions

As promised, a brief look at the effects of conditions on entrainment is included in Figure 4.15. Additional deployments were conducted but left out due to unsuitability of the data (this included a deployment conducted at neaps, unfortunately). Entrainment velocity from tracks travelled each day between 4-5 hshw were used here for comparison.

There is too much complexity to delve into here, but a quick look demonstrates that conditions do have an effect, but seemingly not a big one. Some variability is evident, especially on April 1 (purple), when winds were onshore, effectively contraining the movement of the plume, and thus limiting entrainment. Values are also higher on March 22 (orange), possibly due to wind direction (perpendicular to the streamwise flow of the plume) and values are lower on April 4 (turquoise), possibly due to increased sratification, as freshwater influx was highest on this day. April 3 (green) shows less variability in the spread of values due to it being such a short track.

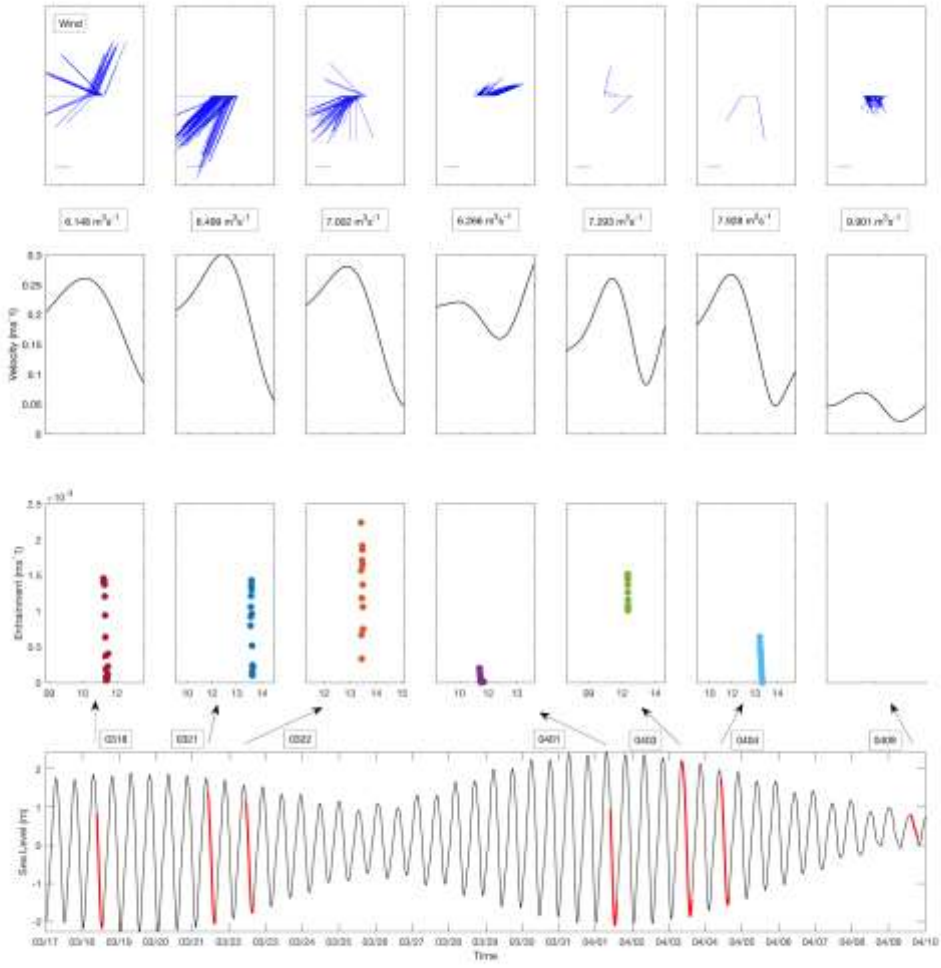

Figure 4.15: Wind (in ms^{-1}, top panel), river flow (small panels, second), tidal current velocity (third panel), entrainment velocity (fourth panel) and sea level as measured by the moored ADCP (bottom panel). Days are indicated next to arrows at the bottom, with stages of the tide during which drifters were deployed in red.

5 DISCUSSION: ENTRAINMENT AND COMPARISON WITH THE COLUMBIA RIVER

5.1 April 3- At a Glance

April 3 was fairly straightforward in terms of the dynamics. It is obvious from the results that a buoyant, spreading outflow develops over the course of the late ebb. Evidence of a jet exists in 3 of the four chosen deployments when tidal velocities are higher, but the increase in density anomaly with time along with the decrease in layer velocity, progressively slows down mixing with each deployment. This increase in the density anomaly, along with mooring data not presented here that show a sudden decrease in salinity later in the ebb tide, lend support to the fact that the Teign estuary is partially mixed, at least during times of relatively low runoff, an observation supported by previous studies (Pritchard, 2000).

Entrainment values calculated using both temperature and salinity show pretty good agreement on this day, with track means agreeing to within 2.6 x 10^{-4} ms^{-1}, and cast values 5.9 x 10^{-4} ms^{-1}. The bulk of the difference that does exist is most likely due to the errors associated with the TS fit.

According to the terms of the entrainment equation (Figure 4.12), the fractional spreading terms for all deployments described in the results suggest that spreading is the single-most important indicator of entrainment, and is almost balanced by the thinning term, an indicator that entrainment is not occuring. Deceleration is more of a factor during D3(2), likely due to the approach of the front, and D5(1), as the ebb slows down and readies for the flood.

5.2 Comparison with Columbia River

5.2.1 Comparison between scales

To provide some context as to the difference in scale between the Teign outflow and the Columbia River outflow, the Columbia River is one of the four largest river outflows in the United States. The Columbia River estuary mouth is approximately 3.5 km across and 20 m deep, whereas the Teign estuary mouth is 0.125 km wide and approximately 5 m deep at low tide, at the time of this study. The Columbia mixed semidiurnal regime has a tidal range of typically 1-3 m, with near-surface velocities reaching 3 ms^{-1}. The Teign tides are semidiurnal, with maximum tidal velocities as high as 3-5 ms^{-1} measured at the mouth, but with surface velocities only as high as 1.4 ms^{-1} seen just 0.8 km seaward, along the channel, during this study, possibly due to the outlet channel's complex bathymetry. The Columbia outflow, on the other hand, encounters a sill and then a steep shelf. Columbia discharge ranges from 3,000 m^3s^{-1} in summer to 17,500 m^3s^{-1} in spring, whereas the Teign average discharge is 5.6 m^3s^{-1} and maximum values range from 44-140 m^3s^{-1}.

McCabe, et al. (2008) calculated a Kelvin Number of ~0.3, using a ratio of the river mouth width to the baroclinic Rossby Radius (R'), which is calculated using the equation $R'=(g'h)^{1/2}/f$, where g' is the reduced gravity, h is the thickness of the buoyant

layer, and f the Coriolis parameter, 1 x 10^{-4}. This differed from other calculations of the Kelvin number for the Columbia River plume (Horner-Devine et al., 2009; Hickey et al, 1998), which used plume width as a characteristic length scale, rather than the width of the mouth. Those resulted in K = 2, similar to that calculated for the Teign by Pritchard (2000). In this instance, the McCabe calculation seems appropriate as both that study and the current study are focused on the near-field, or tidal region, of both plumes, where using the river mouth as the characteristic length scale makes sense. Coriolis does eventually affect the Columbia River outflow, in contrast to the Teign outflow, but this occurs in the far-field, or the Columbia River plume's re-circulating and far-field regions, when the plume expands and slows down. This region was not the focus of the McCabe study.

For the reasons stated above, and to maintain consistency, the same length scale is used to calculate the Kelvin number for the Teign. Based on a baroclinic Rossby radius of 2.16, K= 0.06, an order of magnitude smaller than the Columbia River. This indicates that Coriolis has even less of an effect in this system. This is supported by the constant radial shape maintained by the Teign plume (up to a width of 4 km) in X-band radar images used by Pritchard (2000), which called into question his own calculation of the Kelvin number at that time. In our case, the front was never visually identified as being further than 2 km from the mouth, likely due to reduced freshwater runoff in comparison to earlier studies, which would still result in $K < 1$, even if using plume width as the characteristic length scale.

Comparing the near-field regions of both plumes, the Kelvin number differs by an order of magnitude, essentially a reflection of the difference in physical size between the two systems. Both are less than 1, indicating that the forces driving both systems may be similar, or at the very least, do not include effects induced by the Coriolis effect.

5.2.2 Comparison between deployments

McCabe et al. conducted a single drifter deployment to describe plume entrainment dynamics, which is the largest difference between the two studies. The same could not have been done here, as the Teign outflow is short-lived and the drifters would have

crossed the front too early on in the deployment. This was advantageous in the case of the Teign, as insight was gained into how the plume evolves through the ebb.

5.2.3 Comparison between data analyses

5.2.3.1 Density profiles and choosing T_e

Columbia River flow was considerably larger than any of the Teign tributaries, at 6400 m^3s^{-1}, but still on the lower end of the typical annual range, which is 3000 to 17000 m^3s^{-1}. This resulted in considerably lower salinities in the Columbia river (Figure 5.1), with the Teign outflow ranging from 34.25 psu during our first deployment on April 3 (~1.5 hshw) to 29.6 psu late in the deployment. By contrast, the Columbia outflow measured 10-12 psu at the start of the drifter tracks. An approximate density anomaly of 2-3.7 kgm^{-3} existed near the mouth for the Teign deployments (progression from D3(2) to D5(1)), and for the Columbia it was larger, at approximately 12 kgm^{-3} near the mouth, and 5 kgm^{-3} at 20 km.

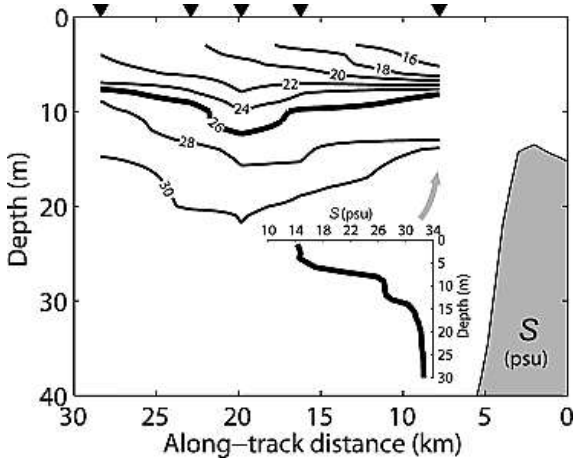

Figure 5.1: Salinity section of the Columbia River plume, contructed from hydrographic profiles (triangles). Salinity contours are in black, with the 26 psu isohaline in bold (S_e). The inset panel shows the initial salinity profile and the one used to choose it as the plume base, from McCabe et al., 2008. See Figure 4.6 or Teign density profiles.

The decision to change the location at which T_e was chosen was made to avoid overestimating the plume thickness, and it seemed appropriate to delineate the two layers by the region with the largest density difference, as mixing below this region may have been influenced by the effects of bottom friction, and those were not desired in this case.

The S_e value for the Columbia was 26 psu, and in our case the corresponding isohaline typically fell within 33.2-35 psu, as mixing with ambient seawater is more complete in the case of the Teign, and fewer plume remnants remain between ebbs.

5.2.3.2 Choosing a section of track

This step was not applicable to the Columbia River study, but one thing to note is the difference in drifter velocities between the two studies. Velocities were much higher in the Columbia outflow, as high as between 2 and 3 ms^{-1} initially, in comparison to our April 3 deployment, which was closer to 0.65 ms^{-1}. The Columbia River tidal range is smaller than in the Teign, though despite this, drifter velocities are much faster, likely due to the increased volume and negative streamwise pressure gradient associated with the freshwater input and surface height field (McCabe et al., 2009). In addition, the Teign jet is slowed considerably at the estuary mouth.

In addition, the drifters in the McCabe study remained in the water for 9 hours (from peak ebb), and did not encounter the front until 4 hours at the earliest (northern drifter), and >7 hours for the remaining drifters (Figure 3.11). Data beyond this point were not included in their analysis. The Teign tracks are much shorter, but this did not have an adverse affect on the outcome.

5.2.3.3 Plume thickness

Modelled plume thicknesses, based on the fit data, for the Columbia River (Figure 5.2) ranged from approximately 12 m at the outset, and then decreased to 10 m before increasing again to between 15 and 20 kilometers, where the steady-state assumption became invalid. See Figure 4.8 for the Teign equivalent, but the range was roughly 2-3

m at the outset. The exponential fits were used in the Columbia study as a result of the effects small changes in salinity, velocity or drifter spread had on the modelled plume thickness. This was unneccessary in the case of the Teign.

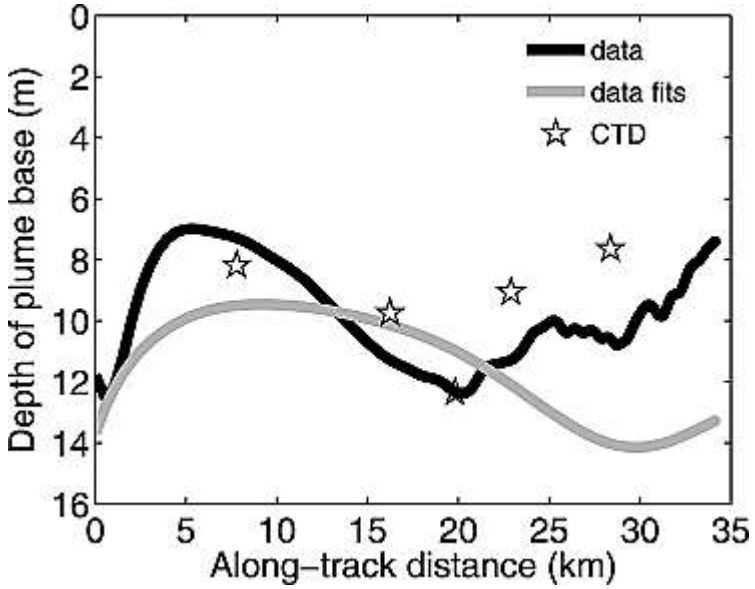

Figure 5.2: Modelled plume thickness for the Columbia plume, for fit (gray) and unfit (black) data. The stars indicate the location of the CTD casts. See Figure 4.8 for Teign modelled plume thickness.

5.2.4 Entrainment

The maximum Columbia values at the beginning of the track were ~2 x10^{-3} ms^{-1} (unfit data), or ~1.8 x 10^{-3} ms^{-1} (unfit data), and look to be on the order of 10^{-4} by 20 km offshore where the steady state assumption becomes invalid. Seeing as the actual entrainment data for the Columbia River is not at hand, it is difficult to compare track means between the two systems with absolute accuracy, but a rough mean was calculated to be 9.5 x 10^{-4} ms^{-1} (Figure 5.3). This is approximately double the Teign's overall track average for the four groups of drifters, 4.33 x 10^{-4} ms^{-1}, but looking only at D3(2), which is the deployment closest to maximum ebb, early Columbia River estimates only slightly exceeded the Teign plume estimates. It should be taken into account that surface values were used to represent full plume quantities in the Columbia

study, whereas Teign values were measured at approximately 0.5 m in a 2-3 m plume (including shear layer). This could lead to larger overestimates in the Columbia values than in the Teign. That said, these results demonstrate that although the Columbia is so much larger on a physical scale to the Teign, that entrainment in the Teign plume still rivals that of the Columbia.

Looking at the terms of equation (20), the equation that was used to calculate entrainment values for both studies, the scales of the following quantities are of primary importance: U, h, ΔS and $\partial S/\partial x$. Looking at the difference in these terms across the Columbia and Teign outflows, the Columbia plume thickness (h) and drifter velocities (U) are significantly larger than the Teign. The difference between plume salinity and ambient salinity (ΔS), is also a bit larger than the Teign, but the change in salinity with along-track distance ($\partial S/\partial x$) is bigger in the Teign.

Looking at the terms of entrainment from equation (17), thinning, deceleration and fractional spreading, the Teign outflow displays a slightly increased mean fractional spreading term over the Columbia River, in addition to a deceleration term that is an order of magnitude smaller and a thinning term that is an order of magnitude larger than the Columbia. It is difficult to explain these differences with certainty without having performed a lateral momentum balance analysis for the Teign for this study, but there are few general possibilities. The difference in the fractional spreading term is likely to be attributed to differences in the cross-stream or stream-wise pressure gradients, with one potential explananation including the Coriolis effect, which does affect plume spreading in the cross-stream direction in the Columbia River (McCabe et al., 2009), especially further away from the source. There is also a possibility that the Teign drifters were deployed slightly outside of the plume core, and spreading is greater closer to the edges of the plume. This was difficult to avoid without the ability to visualise the overall plume structure on any given day. Consistency was the aim; deploying at the same site as much as was possible, and choosing the site based on its central location and proximity to the mouth

In terms of plume deceleration, it is possible that the Teign estimates are made during a period of plume evolution where the plume has just lifted off, and acceleration due to shoaling of the upper layer is balancing that of deceleration caused by mixing. This is supported by the Teign's extra large thinning term, and could also explain the differences in fractional spreading. Another possibility is the internal plume stress due

to shear as a main driver in plume deceleration in the Columbia, a direct consequence of the difference in velocity of the plume and ambient layers. Another important factor is the relaxation of the pressure gradient as the surface height of the outflow decreases. Both effects would be more pronounced in the Columbia River, due to sheer size, density gradient and streamwise velocity. In addition, the majority of the deceleration of the estuarine outflow in the case of the Teign happens as it flows through the bar system just outside of the mouth (and before the drifter deployment site in this study), and the deployments analysed here occurred just after peak ebb, resulting in velocities 0.4-0.5 m/s slower than at peak.

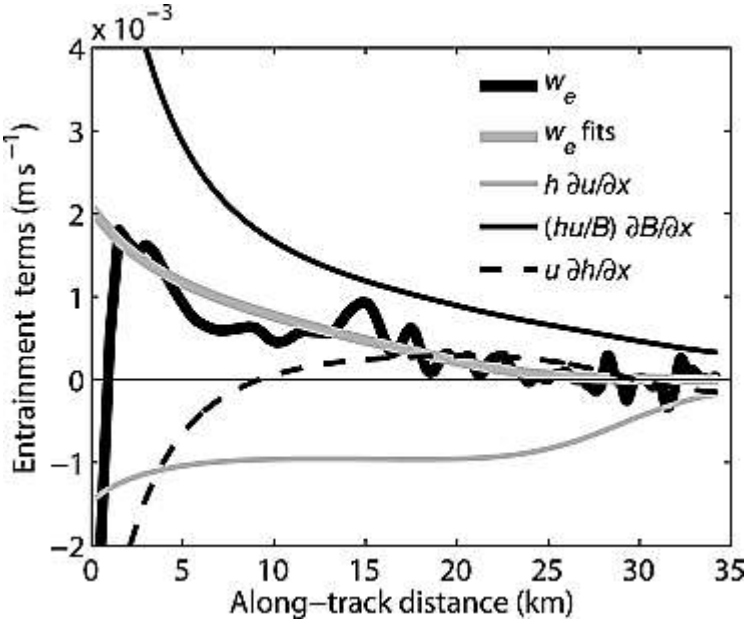

Figure 5.3: Entrainment Velocity (w_e), from fit (thick grey) and un-fit (thick black) data, in addition to the terms of the entrainment equation (17); deceleration (thin grey), fractional spreading (thin black) and thinning (dashed black) in the Columbia River, from McCabe et al., 2008. See Figure 4.9 and Figure 4.12 for equivalent values in the Teign.

5.2.5 Salt flux and diffusivity

Looking at the differences in salt flux and diffusivity, an even clearer picture of the contrast between the two systems becomes apparent. Salt flux is on the same order of

magnitude between the Teign and the Columbia, at 0-5 x 10^{-2} psu ms^{-1} and 0-3 x 10^{-2} psu ms^{-1}, respectively, yet diffusivity values at the cast locations differ by close to an order of magnitude, with the Teign coming out higher. The Columbia values ranged from ~0.2 - ~9.6 x 10^{-3} m^2s^{-1}, while the Teign values ranged from 0.5-5.8 x 10^{-2} m^2s^{-1} (see Section 4.3.5), with microstructure data from the plume interior (measured on a different day) agreeing well with a mean of 2.6 x 10^{-2} m^2s^{-1}. This may also be compared to diffusivity estimates of $O(10^{-2})$ m^2s^{-1} from Orton and Jay (2005) from the frontal region of the Columbia River (compared to $O(10^{-1})$ m^2s^{-1} in the Teign plume front), as well as $O(10^{-3})$ m^2s^{-1}– $O(10^{-2})$ m^2s^{-1} as average ebb values measured within 5 km of the Columbia River jetties, and $O(10^{-3})$ m^2s^{-1} within 10 km of the jetties, at the plume base (Kilcher and Nash, via McCabe et al., 2008).

Looking at equation (21) for calculating the diffusivity of salt (K_s), with salt flux values being similar in magnitude between the two systems, the salinity gradient was smaller in the Teign plume, leading to higher diffusivity values. So, essentially, while everything about the Columbia River is bigger than the Teign, smaller gradients within a plume the size of the Teign leads to a higher level of mixing relative to its size, further supporting the fact that small plumes do mix more quickly. As it becomes more difficult for sediment to be resuspended and settle once the plume loses contact with the bottom (Geyer et al., 2004), it follows that, if a plume mixes more quickly, this sediment and other anthropogenic materials carried within the plume may settle out as well, closer to the coast, or at least remain in the near-coastal circulation, with potential effects to the local marine life and human population.

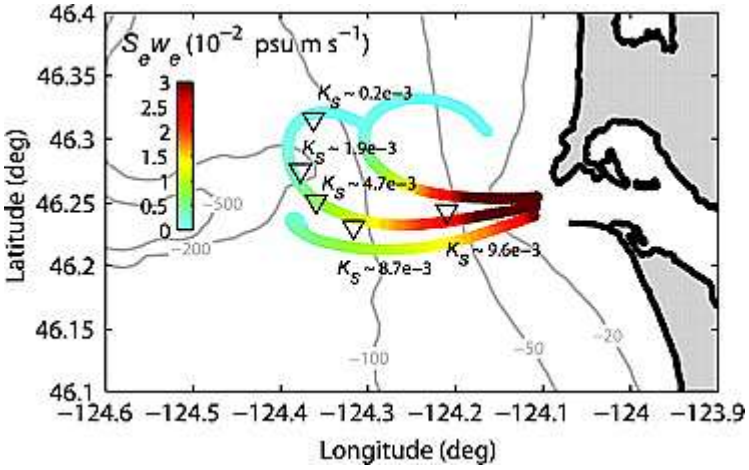

Figure 5.4: Salt flux (coloured drifter tracks) and diffusivity (triangles) estimates in the Columbia River, from McCabe et al., 2008. See Figure 4.13 for equivalent values in the Teign.

5.3 Comparison with previous studies in the Teign

Entrainment velocity was previously calculated by Pritchard (2000) at and behind the Teign plume front, using the following equation:

$$\frac{\partial}{\partial \bar{x}}(\bar{U}D) = q_e(\bar{x})$$

with $\bar{x}$ = distance behind the front (m), D = depth of the interface (m), $\bar{u}$ the velocity relative to the front (ms^{-1}) and q_e the entrainment velocity in ms^{-1}. Detrainment is evident at the plume front, with q_e values reaching -0.6 x 10^{-2} ms^{-1}, but values then become positive just behind the front, starting at $O(10^{-2})$ ms^{-1} and steadily decreasing to zero and beyond (additional detrainment becoming evident at various locations). The scale in Figure 5.5 makes it difficult to distinguish between orders of magnitude, but our values safely fall within the limits here and make sense within the context of both sets of estimates. Entrainment behind the front increases with subsequent transects throughout the ebb, looking to be $O(10^{-3})$ ms^{-1} – $O(10^{-4})$ ms^{-1} between 20 and 70 m behind the front. The plume was bigger (radially) during the Pritchard study, with larger

freshwater outflow (13.642 m^3s^{-1} for a,b, and c and 10.942 m^3s^{-1} for d), and so more space over which to measure entrainment in the plume interior, which may have resulted in a larger quantity of lower entrainment values had the same conditions existed in the Teign.

It must be pointed out that the entrainment values calculated in the current study were very possibly influenced by dynamics in the 'lift-off' region, and therefore may be biased higher than when measuring solely within the plume interior (no effects from the source, lift-off or front). There was little choice in this case. Without greater amounts of freshwater input, the plume would only grow so large before mixing, especially on days of increased wind or tides, and competition between the front and lift-off made it more difficut to choose values from the so-called 'plume interior'. During the April 3 deployment and also April 4, there is typically a linear decrease in entrainment velocity with distance from the mouth, suggesting that this trend would continue if the plume were larger, especially as velocities decrease and mixing continues to add stability to the water column. Analysing data within the lift-off region is still valid, as entrainment is happening due to shear at the base of an accelerating (and shoaling) plume, but some effect from bottom stress experienced prior to lift-off may remain, and it should be noted that entrainment will be higher in this region.

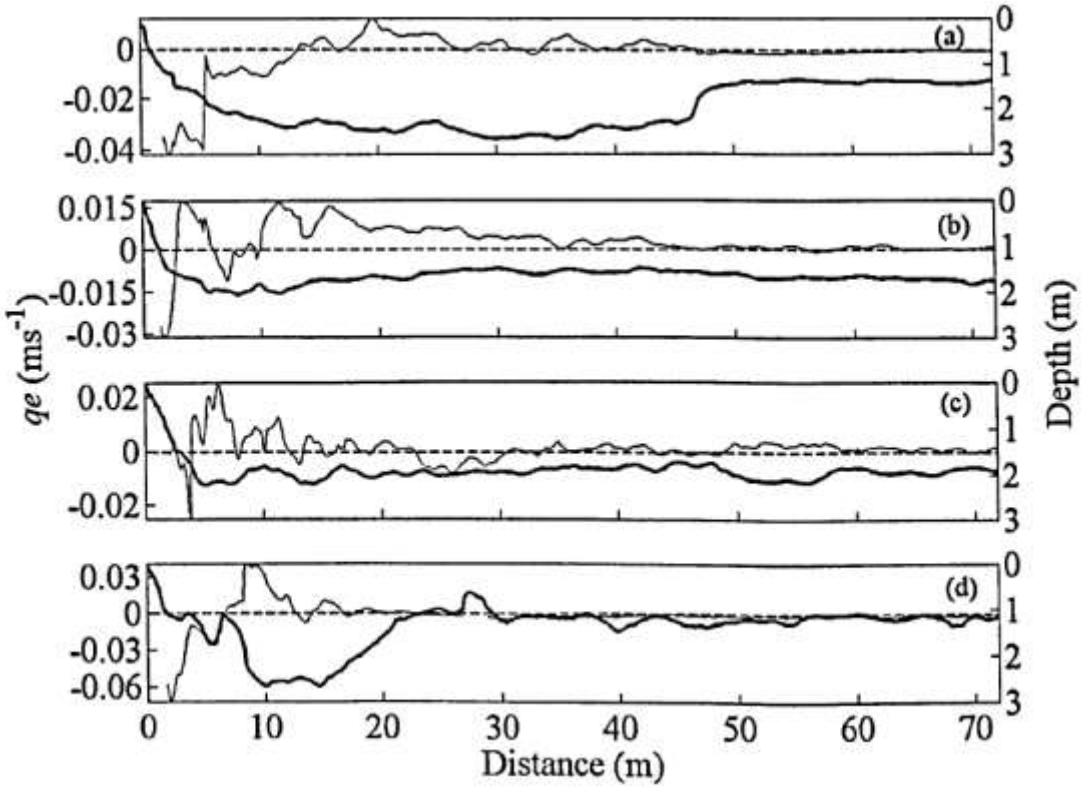

Figure 5.5: Entrainment velocity (q_e) at the leading front vs. distance for 4 transects on November 25 (a, b, c) and November 26 (d), 1998, from Pritchard, 2000. The plume interface is denoted by the thick black line.

5.4 Comparison with other plumes

Following is a brief look at entrainment values measured in other plumes: small, medium and large.

First, Luketina and Imberger (1987;1989) measured entrainment at ~1.7 x 10^{-3} ms^{-1}, which was the maximum value found near the plume front in the Leschenchault Estuary outflow. This value decreased to 1/10 that value (10^{-4}) within 300m behind the front. This is a small plume, similar in size to the Teign, and with a similar density profile. In addition, they measured diffusivity at 0.2 m^2s^{-1}, 50 m behind the plume front. The former (entrainment) is an order of magnitude smaller than the average value from the Teign on April 3 (though on par with those form peak ebb) but the diffusivity is comparable to measurements made with the microstructure profiler at the front during

the current study, with diffusivities in both smaller plumes being a magnitude larger than those measured in the Columbia River.

Entrainment values in the Fraser River in British Columbia, Canada (MacDonald and Geyer, 2004) were 1-4 x 10^{-3} ms^{-1} 1 km seaward of the salt wedge front at the base of the plume, just after lift-off, a comparable location to the Teign estimates. The Fraser River is considered a medium plume with $K < 1$, and these estimates agree well with both the Columbia and the Teign. Diffusivity estimates for the same region ranged from 0-7 x 10^{-3} m^2s^{-1}, which is an order of magnitude smaller than the Teign estimates from the plume base, again agreeing well with the relationship already described between large (i.e. Columbia) and small (i.e. Teign) plumes with smaller density gradients.

Lastly, vertical diffusivity estimates were made in the far-field region (approximately 300 m from the source in this case) of a wastewater plume near the Akashi Strait in Osaka Bay, Japan. Vertical eddy diffusivity was derived analytically using a calculation for open-channel flow, based on the assumption of a parabolic eddy viscosity, bounded by the bed and surface ($D_z = 0.067hu_*$), and then verified by calculation of Thorpe scales from hydrographic profiles. These estimates ranged from $O(10^{-1} – 10^{-3})$ m^2s^{-1}. In small outflows such as this, most of the dilution happens in the near-field (Wood, et al., 1993; Jirka, 2004), and so it seems reasonable that if estimates were made in the near-field, they would be larger than all of the plumes mentioned thus far.

6 CONCLUSIONS

6.1 Concluding remarks

A control volume analysis, using drifters, was performed for a small, radially-spreading estuarine plume in the southwest of England. Estimates of entrainment, salt flux, and diffusivity of salt were made using conservation of momentum, volume and salt. Estimates of entrainment and salt flux rivalled those found in the Columbia River using a similar analysis, and one that inspired that used in the current study. Diffusivity estimates were higher, all documenting the increased propensity for mixing in a small geophysical plume.

With this analysis, the mixing process was essentially determined in reverse; entrainment and then salt flux, and last, diffusivity, when obviously the latter is responsible for the former two. With higher diffusivities and smaller vertical density gradients, resulting salt flux and entrainment are the same order of magnitude as that of the larger plume. The increased turbulence that results from the weaker density gradients effectively balances the contribution to mixing that the sheer size of the larger plumes provide (i.e. the combination of increased flow velocities, plume thickness and density/salinity anomaly), which in turn leads to a larger streamwise salinity gradient in the smaller plume, reflecting a comparable level of entrainment.

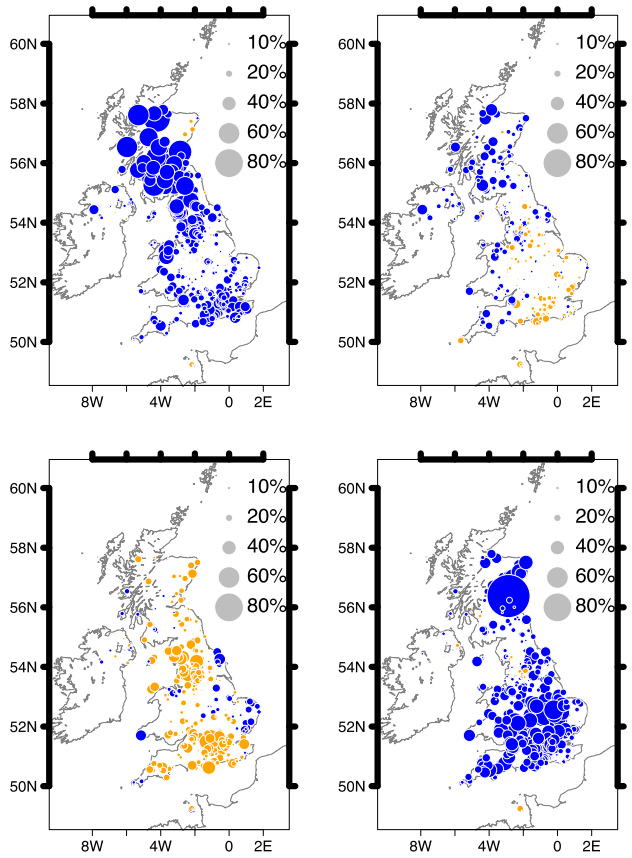

Figure 6.1: Trend of mean precipitation relative to mean calculated for period from 1961-1990. Upper left (winter), upper right (spring), lower left (summer), lower right (autumn). Blue indicates an increase, and yellow, a decrease, from Maraun et al., 2008.

This all supports the early assertion that smaller plumes mix more quickly than their larger counterparts, and thus the materials that they carry will have a larger impact, if not individually then collectively, on the local environment into which they flow. This information can help to inform modelling efforts, as all freshwater sources, large and small, will become increasingly important as the climate changes, as has been seen in the Tarim River Basin in China (Chen, Y. et al., 2006) where river flow in the Aksu and Yarkant rivers has increased significantly in the past 50 years, coinciding with increased temperatures and precipitation in that region. It has been predicted that climate change will result in greater amounts of precipitation as the earth warms, and thus will result in a higher anthropogenic impact from runoff, including excess nutrients and the resulting eutrophication, on the coastal margin (Sinha, 2017; Halpern, 2015).

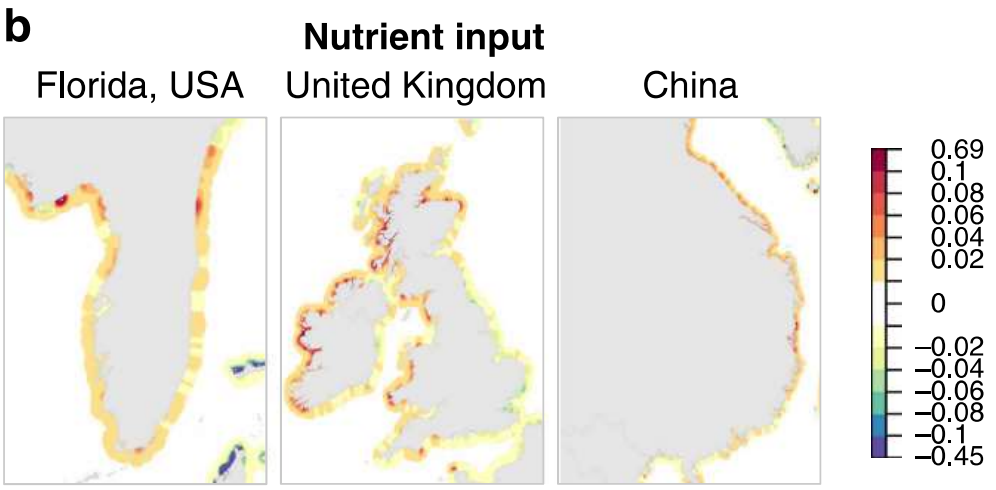

Figure 6.2: Absolute difference between 2008 and 2013 in intensity of nutrient input, from Halpern, 2015.

In the UK specifically, mean precipitation increased during the period from 1961 – 2006 (Figure 6.1), as did the intensity with which it falls, though causation was not established (Maraun, 2008). With respect to land-based anthropogenic impacts including, but not limited to: nutrient, organic and non-organic pollution, a modelled increase occurred globally, from 2008 to 2013, including along the British coastline (Figure 6.2). More accurate model parameterisations, provided by studies like the current one, will lead us one step closer to understanding the collective effect of freshwater runoff into the sea, and we can only benefit from a clearer understanding of the mechanisms by which materials are transported into the coastal zone. This will be key in lessening our impact, as increased precipitation and runoff will only exacerbate the effects of human influence moving into the future.

6.2 Further study

Further study would include an in-depth look at the data collected on the remaining days of the experiment, including statistical analysis of the various weather variables and the effect that those changes may have on the mixing parameters estimated here. In

addition, an in-depth momentum balance analysis is necessary, including the terms that were left out of the balance established by Pritchard (2000), in order to provide further insight into the dynamics of the Teign. Finally, further analysis of the microstructure data, in conjunction with turbulence as calculated from the high-resolution ADCP data, would be interesting, to further enhance understanding of the plume mixing.

7 REFERENCES

Aguilar-Islas, A., & Bruland, K. (2006), Dissolved manganese and silicic acid in the Columbia River plume: A major source to the California Current and coastal waters off Washington and Oregon. *Marine Chemistry*, *101*, 233–247. doi:10.1016/j.marchem.2006.03.005

Archetti, R., & Mancini, M. (2012), Freshwater dispersion plume in the sea: Dynamic description and case study. In H.E. Schulz, A.L. Andrade Simões & R. Jahara Lobosco (Eds.), *Hydrodynamics – Natural Water Bodies* (pp.129-154). In Tech. doi: 10.5772/28390

Armi, L.D. (1975). *The Internal Hydraulics of Two Flowing Layers of Different Densities* (Doctoral dissertation). University of California, Berkeley, California.

Armi, L.D., & Farmer, D.M. (1986). Maximal 2-layer exchange through a contraction with barotropic net flow. *Journal of Fluid Mechanics, 164*, 27-51. doi: 10.1017/s0022112086002458.

Avicola, G., & Huq, P. (2002). Scaling analysis for the interaction between a buoyant coastal current and the continental shelf: Experiments and observations. *Journal of Physical Oceanography, 32*, 3233-3248.

Barry, M. E., Ivey, G. N., Winters, K. B., & Imberger, J. (2001). Measurements of diapycnal diffusivities in stratified fluids. *Journal of Fluid Mechanics*, *442*, 267-291.

H. Z. Baumert, J. H. Simpson & J. Sunderman, J. (Eds.), *Marine Turbulence: Theories, Observations and Models, Volume 1.* Cambridge University Press.

Benjamin, T. B. (1968). Gravity currents and related phenomena. *Journal of Fluid Mechanics, 31*, 209–248.

Blanton, J.O. (1981). Ocean currents along a nearshore frontal zone on the continental shelf of the southeastern United States. *Journal of Physical Oceanography, 11*, 1627-1637. doi: 10.1175/1520-0485(1981)011<1627:OCAANF>2.0.CO;2

Bricker, J. D., and Nakayama, A. (2007). Estimation of far-field horizontal and vertical turbulent diffusion coefficients from the concentration field of a wastewater plume near Akashi Strait. *Environmental Fluid Mechanics, 7(1)*, 1–22. doi: 10.1007/s10652-006-9013-4

Britter, R. E., & Simpson, J. E. (1981). Note on the structure of the head of an intrusive gravity current. *Journal of Fluid Mechanics, 112*, 459-466.

Britter, R. E., & Simpson, J. E. (1978), Experiments on the dynamics of a gravity current head. *Journal of Fluid Mechanics, 88*, 223–240.

Bruland, K., Lohan, M., Aguilar-Islas, A., Smith, G., Sohst, B., & Baptista, A. (2008), Factors influencing the chemistry and formation of the Columbia River plume: Nitrate,

silicic Acid, dissolved Fe and dissolved Mn. *Journal of Geophysical Research, 113*. doi:10.1029/2007JC004702

Burke, D. (1997). *Use of Photo-Mosaics to Monitor Estuary Mouth Sandbanks*, (Unpublished M.Sc. Thesis, University of Plymouth).

Buck, K., Lohan, M., Berger, C., & Bruland, K. (2007). Dissolved iron speciation in two distinct river plumes and an estuary: Implications for riverine iron supply. *Limnology and Oceanography, 52*, 843– 855. doi: 10.4319/lo.2007.52.2.0843

Chao, S., & Boicourt, W.C. (1986). Onset of estuarine plumes. *Journal of Physical Oceanography, 16*, 2137–2149.

Chao, S. (1988a). River-forced estuarine plumes. *Journal of Physical Oceanogaphy, 18*, 72–88. doi: 10.1175/1520-0485(1988)018<0072:RFEP>2.0.CO;2

Chao, S. (1988b). Wind-driven motion of estuarine plumes. *Journal of Physical Oceanography, 18*, 1144–1166.

Chant, R. J., 2012: Interactions between estuaries and coasts: River plumes—their formation, transport, and dispersal. In, Water and Fine-Sediment Circulation, R. J. Uncles and S. G. Monismith, (Eds.), Vol. 2, *Treatise on Estuarine and Coastal Sciences,* Academic Press, 213–236

Chapman, D.C., & Lentz, S.J. (1994). Trapping of a coastal density front by the bottom boundary layer. *Journal of Physical Oceanography, 24(7),* 1464-1479.

Chen, J.C. (1980), *Studies on Gravitational Spreading Currents* (Doctoral dissertation). California Institue of Technology, Pasadena, California.

Chen, F., & MacDonald, D.G. (2006). Role of mixing in the structure and evolution of a buoyant discharge plume. *Journal of Geophysical Research, 111(C11),* 2156-2202. doi:10.1029/2006JC003563.

Chen, F., MacDonald, D.G., & Hetland, R.D. (2009). Lateral spreading of a near-field river plume: Observations and numerical simulations. *Journal of Geophysical Research, 114(C07013)*. DOI:10.1029/2008JC004893

Chen, Y., Takeuchi, K., Xu, C., Chen, Y., & Xu, Z. (2006). Regional climate change and its effects on river runoff in the Tarim Basin, China. *Hydrological Processes, 20*, 2207–2216. DOI:10.1002/hyp.6200

Craig-Smith, S.J. (1970). *A Hydrograpic Analysis of the Approaches to Teignmouth*, (Unpublished M.Sc. Thesis, University of Leicester).

Cromwell, T., & Reid, J.L. (1956). A study of oceanic fronts. *Tellus* 8(1) (1956): 94-101.

Davis, R.E. (1985). Drifter observations of coastal surface currents during CODE: The statistical and dynamical views. *Journal of Geophysical Research: Oceans, 90(C3)*. doi: 10.1029/JC090ic03p04756

Dewey, R. K., Crawford, W. R., Gargett, A. E. & Oakey, N. S. (1987).A microstructure instrument for profiling oceanic turbulencein coastal bottom boundary layers. *Journal of Atmospheric Ocean Technology, 4,* 288-297.

Didden, N., & Maxworthy, T. (1982). Viscous spreading of plane and axisymmetric gravity currents. *Journal of Fluid Mechanics, 121*, 27-42.

Ellison, T., & Turner, J. (1959). Turbulent entrainment in stratified flows. *Journal of Fluid Mechanics,6*(3), 423-448. doi:10.1017/S0022112059000738

Etemad-Shahidi, A., & Imberger, J. (2001). Anatomy of turbulence in thermally stratified lakes. *Limnology and Oceanography*, *46(5)*, 1158-1170.

Ferron, B., Mercier, H., Speer, K., Gargett, A., & Poltzin, K. (1998). Mixing in the romanche fracture zone. *Journal of Physical Oceanography, 28*, 1929-1945.

Fong, D.A. & Geyer, W.R. (2001). Response of a river plume to an upwelling wind event. *Journal of Geophysical Research, 106*, 1067–1084.

Fong, D.A. & Geyer W.R. (2002). The alongshore transport of freshwater in a surface-trapped river plume, *Journal of Physical Oceanography, 32*, 957–972.

Gargett, A. E., & Moum, J. N. (1995). Mixing efficiencies in turbulent tidal fronts: Results from direct and indirect measurements of density flux. *Journal of Physical Oceanography*, *25(11)*, 2583-2608.

Garvine, R.W. (1974). Physical features of the Connecticut River outflow during high discharge. *Journal of Geophysical Research*,, 79(6), 831–846. doi:10.1029/JC079i006p00831

Garvine, R.W., & Monk, J.D. (1974). Frontal structure of a river plume. *Journal of Geophysical Research*, *79(15),* 2251–2259.

Garvine, R.W. (1982). A steady-state model for buoyant surface plume hydrodynamics in coastal waters. *Tellus, 34(3)*, 293-306.

Garvine, R.W. (1984). Radial spreading of buoyant, surface plumes in coastal waters. *Journal of Geophysical Research, 89*, 1989–1996.

Garvine, R.W. (1987). Estuary plumes and fronts in shelf waters: A layer model. *Journal of Physical Oceanography, 17*, 1877–1896. doi: 10.1175/1520-0485(1987)017<1877:EPAFIS>2.0.CO;2

Garvine, R.W. (1991). Subtidal frequency estuary–shelf interaction: Observations near Delaware Bay. *Journal of Geophysical Research, 96*, 7049–7064.

Garvine, R.W. (1995). A Dynamical system for classifying buoyant coastal discharge. *Continental Shelf Research, 15*, 1585–1596.

Garvine, R.W. (1999). Penetration of buoyant coastal discharge onto the continental shelf: a numerical model experiment. *Journal of Physical Oceanography, 29*, 1892–1909.

Garvine, R.W., & Whitney, M.M. (2006). An estuarine box model of freshwater delivery to the coastal ocean for use in climate models. *Journal of Marine Research 64*, 173–194.

Geyer, W.R., Hill, P.S., & Kineke, G.C. (2004). The transport, transformation and dispersal of sediment by buoyant coastal flows. *Continental Shelf Research, 24*, 927-949.

Gregg, M.C. (1987). Diapycnal mixing in the thermocline: A review. *Journal of Geophysical Research, 92(C5)*, 5249– 5286.

Halpern, B.S., Walbridge, S., Selkoe, K.A., Kappel, C.V., Micheli, F., D'Agrosa, C., Bruno, J.F., Casey, K.S, Ebert, C., Fox, H.E., Fujita, R., Heinemann, D., Lenihan, H.S., Madin, E.M.P., Perry, M.T., Selig, E.R., Spaldig, M., Steneck, R., & Watson, R. (2008). A global map of human impact on marine ecosystems. *Science, 319(5865),* 948-952. doi: 10.1126/science.1149345

Halpern, B.S., Frazier, M., Potapenko, J., Casey, K., Koenig, K., Longo, C., Stewart Lowndes, J., Rockwood, R.C., Selig, E.R., Selkow, K.A., & Walbridge, S. (2015). Spatial and temporal changes in cumulative human impacts on the world's ocean. *Nature Communications, 6(7615)*. doi: 10.1038/ncomms8615

Hench, J.L., & Luettich, R.A. (2003). Transient tidal circulation and momentum balances at a shallow inlet. *Journal of Physical Oceanography, 33*, 913-932.

Hetland, R.D. & MacDonald, D.G. (2008), Spreading in the near-field Merrimack River plume. *Ocean Modelling, 21*, 12–21. doi:10.1016/j.ocemod. 2007.11.001

Hetland, R.D. (2005). Relating river plume structure to vertical mixing. *Journal of Physical Oceanography, 35*, 1667– 1688. doi: 10.1175/JPO2774.1

Hetland, R.D. (2010). The effects of mixing and spreading on density in near-field river plumes. *Dynamics of Atmospheres and Oceans, 49(1)*, 37-53. doi:10.1016/j.dynatmoce.2008.11.003

Hickey, B. M., & Hamilton, P. (1980). A spin-up model as a diagnostic tool for interpretation of current and density measurements on the continental shelf of the Pacific Northwest. *Journal of Physical Oceanography 10(1),* 12-24.

Hickey, B. M., Pietrafesa, L. J., Jay, D.A., & Boicourt, W. C. (1998). The Columbia River plume study: Subtidal variability in the velocity and salinity fields. *Journal of Geophysical Research, 103(C5)*, 10339–10368. doi:10.1029/97JC03290

Hill, J., & Wheeler, P. A. (2002). Organic carbon and nitrogen in the Northern California Current System: Comparison of offshore, river plume, and Coastally upwelled waters. *Progress in Oceanography, 53*, 369– 387, doi:10.1016/S0079-6611(02)00037-X

Horner-Devine, A. (2009). The bulge circulation in the Columbia River plume. *Continental Shelf Research, 29*, 234–251. doi:10.1016/j.csr.2007.12.012

Horner-Devine, A., Jay, D. A., Orton, P. M., & Spahn, E. Y. (2009). A conceptual model of the strongly tidal Columbia River plume. *Journal of Marine Systems, 78*, 460-475. doi:10.1016/j.jmarsys.2008.11.025

Horner-Devine, A., Hetland, R. D., & MacDonald, D. G. (2014). Mixing and transport in coastal river plumes. *Annual Review of Fluid Mechanics, 47*, 569-694. doi: 10.1146/annurev-fluid-010313-141408.

Houghton, R. W., Tilburg, C. E., Garvine, R. W., & Fong, A. (2004). Delaware River plume response to a strong upwelling-favorable wind event. *Geophysical Research Letters, 31*, L07302. doi:10.1029/2003GL018988

Ivey, G. N., & Imberger, J. (1991). On the nature of turbulence in a stratified fluid. Part I: The energetics of mixing, *Journal of Physical Oceanography, 21*, 650–658.

Jay, D. A., Pan, J., Orton, P. M., Horner-Devine, A. R. (2009). Asymmetry of Columbia River tidal plume fronts. *Journal of Marine Systems, 78(3)*, 442-459.

Jirka, G. H. (2004). Integral model for turbulent buoyant jets in unbounded stratified flows. Part 1: The single round jet. *Environmental Fluid Mechanics, 4*, 1–56

Kilcher, L. F., & Nash, J. D.(2010). Structure and dynamics of the Columbia River tidal plume front. *Journal of Geophysical Research* 115(C5), 2156-2202.doi: 10.1029/2009JC006066

Kingsford, M. J., & Suthers, I. M. (1994). Dynamic estuarine plumes and fronts: importance to small fish and plankton in coastal waters of NSW, Australia. *Continental Shelf Research, 14(6),* 655-672.

Kolmogorov, A. (1941). The local structure of turbulence in incomressible vicous fluid for very large Reynolds' numbers. *Doklady Akademiia Nauk SSSR, 30,* 301-305.

Kourafalou, V. H., Oey, L.-Y., Wang, J. D., & Lee, T.N. (1996). The fate of river discharge on the continental shelf 1. Modeling the river plume and the inner shelf coastal current. *Journal of Geophysical Research 101(C2),* 3415-3434.

Knauss, J. A. (1957). An observation of an oceanic front. *Tellus 9(2)*, 234-237.

Largier, J. L. (1992). Tidal intrusion fronts. *Estuaries 15*, 16–39.

Largier, J. L. (1993). Estuarine fronts: How important are they? *Estuaries 16(1),* 1-11.

Le Fèvre, J. (1987). Aspects of the biology of frontal systems. *Advances in Marine Biology, 23,*163-299. doi: 10.1016/S0065-2881(08)60109-1

Lentz, S. J., & Helfrich, K. R. (2002). Buoyant gravity currents along a sloping bottom in a rotating fluid. *Journal of Fluid Mechanics 464(1),* 251-278.

Lentz, S.J., & Largier, J.L. 2006: The influence of wind forcing on the Chesapeake Bay buoyant coastal current. *Journal of Physical Oceanography, 36*, 1305–1316. doi: 10.1175/JPO2909.1

Lohan, M., & Bruland, K., 2006. Importance of vertical mixing for additional sources of nitrate and iron to surface waters of the Columbia River plume: Implications for biology. *Marine Chemistry 98*, 260–273.

Luketina, D. A., & Imberger, J. (1987). Characteristics of a surface buoyant jet. *Journal of Geophysical Research, 92,* 5435–5447.

Luketina, D. A., & Imberger, J.(1989). Turbulence and entrainment in a buoyant surface plume. *Journal of Geophysical Research: Oceans (1978–2012), 94(C9),* 12619-12636.

MacDonald, D. G., & Geyer, W. R. (2004). Turbulent energy production and entrainment at a highly stratified estuarine front. *Journal of Geophysical Research, 109,* C05004. doi:10.1029/2003JC002094.

MacDonald, D. G., Goodman, L., & Hetland, R. D. (2007). Turbulent dissipation in a near-field river plume: A comparison of control volume and microstructure observations with a numerical model. *Journal of Geophysical Research, 112*, C07026, doi:10.1029/2006JC004075

Mann, K.H. and Lazier, J.R.N. (2005). Fronts in coastal waters*, in Dynamics of Marine Ecosystems, Third Edition,* Malden, MA, USA: Blackwell Publishing Ltd. doi: 10.1002/9781118687901.ch6

Marmorino, G. O., & Trump, C. L. (2000). Gravity current structure of the Chesapeake Bay outflow plume. *Journal of Geophysical Research, 105(C12),* 28,847–28,861.

Marmorino, G. O., Cooper, A. L., Mied, R. P., Lindemann, G. J., Trizna, D. B., & Porter, D. L. (2004). Onshore propagation of a buoyant ocean front observed using a shore-based marine radar. *Contintental Shelf Research, 24*, 951–964.

Massey, B. S. (1989). *Mechanics in Fluids*. London: Chapman & Hall.

McCabe, R. M., Hickey, B. M., & MacCready, P. (2008). Observational estimates of entrainment and vertical salt flux in the interior of a spreading river plume. *Journal of Geophysical Research, 113, C08027*. doi:10.1029/2007JC004361

McCabe, R. M., MacCready, P., & Hickey, B. M. (2009). Ebb-tide dynamics and spreading of a large river plume. *Journal of Physical Oceanography, 39(11)*, 2839-2856.

Miles, J., Russell, P.E., Huntley, D. (1997). Introduction to the Coast3D field study site at Teignmouth. Egmond, NL.

Monin, A.S. & Yaglom A.M. (1975). Statistical Fluid Mechanics, Vol. 22. MIT Press.

Morgan, C. A., De Robertis, A., & Zabel, R. W. (2005). Columbia river plume fronts. I. Hydrography, zooplankton distribution, and community composition. *Marine Ecology Progress Series, 299*,19-31.

Morton, B. R., Taylor, Sir G., Turner, J. S. (1956). Turbulent gravitational convection from maintained and instantaneous sources. *Proceedings from the Royal Society London A: Mathematical, Physical and Engineering Sciences, 234(1196)*, 1-23. doi: 10.1098/rspa.1956.0011

Moum, J. (1996). Energy- containing scales of turbulence in the ocean thermocline. *Journal of Geophysical Research, 101(C6),* 14095-14109. doi:10.1029/96JC00507.

Munchow, A., & Garvine, R.W. (1993). Dynamical properties of a buoyancy-driven coastal current. *Journal of Geophysical Research, 98*, 20063–20077.

Nash, J. D., & Moum J. N. (2005). River plumes as a source of large amplitude internal waves in the coastal ocean. *Nature, 437*, 400–403. doi:10.1038/nature03936.

Nash, J. D., Kilcher, L. F., & Moum, J. N. (2009). Structure and composition of a strongly stratified, tidally pulsed river plume. *Journal of Geophysical Research, 114,* C00B12. doi:10.1029/2008JC005036

Nasmyth, P.W. (1970). Oceanic turbulence (doctoral dissertation), University of British Columbia, Vancouver.

Nof, D. (1988). Eddy-wall interactions. *Journal of Marine Research, 46(3)*, 527-555.

O'Donnell, J., Ackleson, S. G., & Levine, E. R. (2008). On the spatial scales of a river plume. *Journal of Geophysical Research, 113*, C04017. doi:10.1029/2007JC004440.

Orton, P. M., & Jay, D .A. (2005). Observations at the tidal plume front of a high-volume river outflow, *Geophysical Research Letters, 32*, L11605, doi:10.1029/2005GL022372

Osborn, T. R. (1974). Vertical profiling of velocity microstructure. *Journal of Physical Oceanography, 4*, 109-115.

Pingree, R. D. , Pugh, P. R., Holligan, P. M., & Forster, G. R. (1975). Summer phytoplankton blooms and red tides along tidal fronts in the approaches to the English Channel. *Nature, 258*, 672-677.

Plant, N. G., Holland, K. T., & Puleo, J. A. (2008). Application of quadratic loess filters to bathymetric bnterpolation. *Naval Research Lab, USA. Accepted for publication in Marine Geology*.

Pritchard, M. (2000). *Dynamics of a small estuarine tidal plume* (Doctoral dissertation), University of Plymouth, Plymouth, UK.

Pritchard, M., Huntley, D., 2002. Instability and mixing in a small estuarine plume front. *Estuarine Coastal and Shelf Science, 55(2)*, 275–285. doi:10.1006/ecss.2001.0902

Pritchard, M., & Huntley, D.A. (2006). A Simplified Energy and Mixing Budget for a Small River Plume Discharge. *Journal of Geophysical Research-Oceans, 111,* C0309. doi: 10.1029/2005JC002984

Rennie, J. (1838). *Report on proposals for maintaining and improving the port of Teignmouth*. Unpublished Report.

Robinson, A.H.W. (1975). Cyclical changes in shoreline development at the entrance to Teignmouth Harbour, Devon, England. In: Hails, J., Carr, A. (Eds.), *Nearshore Sediment Dynamics and Sedimentation* (pp. 181–200). London: Wiley.

Sanders, T. M., & Garvine, R. W. (2001). Fresh water delivery to the continental shelf and subsequent mixing: An observational study. *Journal of Geophysical Research: Oceans*, *106(C11),* 27087-27101.

Shin, J. O., Dalziel, S. B., & Linden, P. F. (2004). Gravity currents produced by lock exchange. *Journal of Fluid Mechanics, 521*, 1–34.

Simpson, J. E., & Britter, R. E. (1979). The dynamics of the head of a gravity current advancing over a horizontal surface. *Journal of Fluid Mechanics 94(3),* 477-495.

Simpson, J. E. (1982). Gravity currents in the laboratory, atmosphere, and ocean. *Annual Review of Fluid Mechanics, 14*, 213–234.

Simpson, J. H., & Hill, A. E. (1986). The Scottish coastal current. In S. Skreslet (ed), *The role of freshwater outflow in coastal marine ecosystems* (pp. 295-308). Berlin, Heidelberg: Springer.

Simpson, J. H., & Souza, A. J. (1995). Semidiurnal switching of stratification in the region of freshwater influence of the Rhine. *Journal of Geophysical Research: Oceans*, *100(C4)*, 7037-7044.

Simpson, J. E. (1999). *Gravity currents: In the environment and the laboratory*. Cambridge university press.

Smyth, W. D., Moum, J. N. & Caldwell, D. R. (2001). The efficiency of mixing in turbulent patches: inferencesfrom direct simulations and microstructure observations, *Journal of Physical Oceanography, 31*, 1969-1992.

Spahn, E. Y., Horner-Devine, A. R., Nash, J. D. & Kilcher, L. F. (2009). Particle re-suspension in the Columbia River plume near-field, *Journal of Geophysical Research: Oceans*, *114*(C2). doi:10.1029/2008JC004986

Spratt, T. (1856). *An Investigation of the Movements of Teignmouth Bar*. London: John Weale.

Stacey, M. T., Rippeth, T. & D Nash, J. (2011), Turbulence and Stratification in Estuaries and Coastal Seas. In E. Wolanski, E. & D.S. McLusky (Eds.), *Treatise on Estuarine and Coastal Science*. (pp. 9-35). Elsevier. doi: 10.1016/B978-0-12-374711-2.00204-7

Taylor, G. I. (1935). Statistical theory of turbulence, Parts i-iv. *Proceedings from the Royal Society of London A 151*, 421-478.

Trump, C.L., Marmorino, G.O., 2003. Mapping small-scale along-front structure using ADCP acoustic backscatter range-bin data. *Estuaries 26*, 878–884.

Van Lancker, V., Lanckneus, J., Hearn, S., Hoekstra, P., Levoy, F., Miles, J., Moerkerke, G., Monfort, O., & Whitehouse, R. (2004). Coastal and nearshore morphology, bedforms and sediment pathways at Teignmouth (UK). *Continental Shelf Research 24(11)*, 1171-1202. doi: https://doi.org/10.1016/j.csr.2004.03.003

Walstra, D.J.R., Van Ormondt, M.,Van Rijn, L.C. (2000). Verification and comparison of the Delft 3D-model for an inlet system (Teignmouth, UK), COAST3D. Overall Workshop, June 2000, Caen.

Whitehead, J., & Chapman, D. C. (1986). Laboratory observations of a gravity current on a sloping bottom: the generation of shelf waves. *Journal of Fluid Mechanics 172*, 373-99.

Whitehouse, R., Hearn, S., Waters, C., Sutherland, J., 2000. Data report on measurements by HR Wallingford at Teignmouth UK (1998–1999). Report TR105, HR Wallingford, Wallingford.

Whitney, M. M., & Garvine, R. W. (2005). Wind influence on a coastal buoyant outflow. *Journal of Geophysical Research: Oceans*, *110*(C3).

Wimpol (1989). *Environmental survey and mathematical modelling of the river Teign estuary and coastal region.* Unpublished Report.

Wood, I. R., Bell, R. G., & Wilkinson, D. L. (Eds.). (1993). *Ocean disposal of wastewater* (Vol. 8). World Scientific.

Yankovsky, A., Chapman, D.C. (1997). A simple theory for the fate of buoyant coastal discharges. *Journal of Physical Oceanography 27,* 1386–1401.

Zaneveld, J. R. V., Andrade, M., & Beardsley, G. F. (1969). Measurements of optical properties at an oceanic front observed near the Galapagos Islands. *Journal of Geophysical Research*, *74(23)*, 5540-5541.

8 APPENDICES

APPENDIX 1: ENTRAINMENT VALUES

Table 4: Entrainment velocity (in ms^{-1}) based on temperature (T) and salinity (S). Track values ar emeans of the along-track values, and cast values are the results for the casts used for the calculations. The difference between cast values and a mean of track values at that location are compared, and reported as a percentage of the cast value.

20140403	W_e Cast (T)	W_e Track (T)	Cast/Track Diff	Percent Diff
D3(2)	0.0017	0.0015	1.087×10^{-4}	6.4
D4(1)	6.945×10^{-4}	5.4352×10^{-4}	-1.127×10^{-4}	16.2
D4(2)	7.369×10^{-4}	2.9075×10^{-4}	3.858×10^{-5}	5.2
D5(1)	3.312×10^{-4} 3.765×10^{-4}	3.675×10^{-4}	-1.037×10^{-4} 1.530×10^{-4}	33.2 40.6

20140403	W_e Cast (S)	W_e Track (S)	Cast/Track Diff	Percent Diff
D3(2)	0.0041	0.0047	4.523×10^{-4}	11.0
D4(1)	4.82×10^{-4}	3.325×10^{-4}	-1.713×10^{-5}	3.6
D4(2)	6.597×10^{-4}	2.957×10^{-4}	-5.307×10^{-5}	8.0
D5(1)	7.328×10^{-4} 8.057×10^{-4}	0.0011	-1.28×10^{-4} 1.621×10^{-4}	17.5 20.1

APPENDIX 2: SALT FLUX AND DIFFUSIVITY VALUES

Table 5: Values for salt flux (in psu ms^{-1}) and diffusivity (in m^2s^{-1}). Track values ar emeans of the along-track values, and cast values are the results for the casts used for the calculations. Diffusivity is only given as means of the cast values.

20140403	S_eW_e Cast (T)	S_eW_e Track (T)	S_eW_e Cast (S)	S_eW_e Track (S)	K_S Cast
D3(2)	0.0571	0.0514	0.1412	0.1635	0.0575
D4(1)	0.0236	0.0184	0.0163	0.0113	0.0196
D4(2)	0.0250	0.0098	0.0224	0.0100	0.0143
D5(1)	0.0112 0.0127	0.0124	0.0248 0.0271	0.0364	0.0042 0.0052